FEDERAL UNIVERSITY OF PARÁ
INSTITUTE OF TECHNOLOGY
POSTGRADUATE PROGRAM IN ELECTRICAL ENGINEERING

HYBRID COMPUTATIONAL APPROACH WITH GNINA AND MOLECULAR DYNAMICS IN THE SEARCH FOR INHIBITORS AGAINST MARBURG VIRUS

AGUINALDO PANTOJA DE ALMEIDA

DM 31/2025

UFPA / ITEC / PPGEE
Guamá University Campus
Belém-Pará-Brazil
2025

FEDERAL UNIVERSITY OF PARÁ
INSTITUTE OF TECHNOLOGY
POSTGRADUATE PROGRAM IN ELECTRICAL ENGINEERING

AGUINALDO PANTOJA DE ALMEIDA

HYBRID COMPUTATIONAL APPROACH WITH GNINA AND MOLECULAR DYNAMICS IN THE SEARCH FOR INHIBITORS AGAINST MARBURG VIRUS

Dissertation submitted to the Examining Board of the Graduate Program in Electrical Engineering at UFPA to obtain the Master's Degree in Electrical Engineering in the Area of Applied Computing.

Advisor: Prof. Dr. Claudomiro de Souza de Sales Junior

DM 31/2025

UFPA / ITEC / PPGEE
Guamá University Campus
Belém-Pará-Brazil
2025

Dados Internacionais de Catalogação na Publicação (CIP) de acordo com ISBD
Sistema de Bibliotecas da Universidade Federal do Pará
Gerada automaticamente pelo módulo Ficat, mediante os dados fornecidos pelo(a) autor(a)

P198h Pantoja De Almeida, Aguinaldo.
HYBRID COMPUTATIONAL APPROACH WITH GNINA AND MOLECULAR DYNAMICS IN THE SEARCH FOR INHIBITORS AGAINST MARBURG VIRUS / Aguinaldo Pantoja De Almeida. — 2025.
102 f. : il. color.

Orientador(a): Prof. Dr. Claudomiro de Souza de Sales Junior
Dissertação (Mestrado) - Universidade Federal do Pará, Instituto de Tecnologia, Programa de Pós-Graduação em Engenharia Elétrica, Belém, 2025.

1. Docagem Molecular. 2. Dinâmica Molecular. 3. Rede Neural Convolucional. 4. Fármacos. 5. DFT. I. Título.

CDD 620

FEDERAL UNIVERSITY OF PARÁ
INSTITUTE OF TECHNOLOGY
POSTGRADUATE PROGRAM IN ELECTRICAL ENGINEERING

HYBRID COMPUTATIONAL APPROACH WITH GNINA AND MOLECULAR DYNAMICS IN THE SEARCH FOR INHIBITORS AGAINST MARBURG VIRUS

AUTHOR: **AGUINALDO PANTOJA DE ALMEIDA**

MASTER'S DISSERTATION SUBMITTED TO THE EXAMINING BOARD AND APPROVED BY THE BOARD OF THE POSTGRADUATE PROGRAM IN ELECTRICAL ENGINEERING, BEING CONSIDERED APPROVED FOR THE AWARD OF THE MASTER'S DEGREE IN ELECTRICAL ENGINEERING IN THE AREA OF APPLIED COMPUTING.

APPROVED IN: 06/10/2025

EXAMINATION COMMITTEE:

Prof. Dr. Claudomiro de Souza de Sales Junior
(Advisor - PPGEE / UFPA)

Prof. Dr. Jasmine Priscyla Leite de Araújo
(Evaluator Interno - PPGEE / UFPA)

Prof. Dr. Ewerton Cristhian Lima de Oliveira
(Evaluator Externo - Vale Technological Institute / VTI)

Prof. Dr. Kauê Santana da Costa
(Evaluator Externo - PROFMAT / UFOPA)

APPROVED BY:

Prof. Dr. Diego Lisboa Cardoso
(Coordinator of PPGEE/ITEC/UFPA)

This dissertation is dedicated to God and my parents, whose effort and wisdom allowed me to complete this master's degree.

Acknowledgements

First and foremost, I thank God, the source of strength, wisdom, and inspiration, who sustained me at every stage of this journey, guiding my steps and renewing my hope in moments of difficulty.

To my parents, Adinaldo Lopes Almeida and Maria Mirian Neris Pantoja, my eternal gratitude for their unconditional love, life teachings, dedication, and example of perseverance, which were fundamental for me to reach this point.

To my brothers, Arnaldo Pantoja de Almeida and Adriano Pantoja Almeida, I express my sincere appreciation for their constant encouragement and, especially, for their financial support, which was undoubtedly essential for the realization of this dream.

I am especially grateful to my colleagues Kleber and Ricardo for their valuable collaboration, technical support, and computational assistance, which were crucial for the development of this research.

Finally, I record my deep gratitude to my advisor, whose guidance, patience, dedication, and trust were indispensable throughout this academic journey. His contribution was essential not only to the development of this work but also to my professional and personal growth.

"A moralidade é a melhor de todas as regras para orientar a humanidade."

Friedrich Nietzsche

Abstract

Molecular modeling has become a crucial tool in studying interactions between drugs and viral targets, allowing the prediction of binding mechanisms and potential therapeutic applications. In this context, four drugs were examined — Ivermectin, Nafamostat, Lopinavir, and Remdesivir — for their potential interactions with the Marburg virus (MARV), exhibiting effective interactive characteristics that suggest a strong possibility of being repurposed for therapeutic approaches against MARV. The effectiveness of these interactions was evaluated through molecular docking, which determines the positions of ligands around the target protein and measures them based on binding energy. The results provided binding energies obtained using *GNINA*, which employs Convolutional Neural Networks, ranging from –8.74 kcal/mol to –10.54 kcal/mol for Ivermectin, –7.37 kcal/mol to –10.46 kcal/mol for Lopinavir, –7.16 kcal/mol to –10.00 kcal/mol for Nafamostat, and –6.56 kcal/mol to –9.59 kcal/mol for Remdesivir. The molecular complexes identified in the docking simulations, together with their respective binding affinities, demonstrated the establishment of interactions between amino acids in the catalytic regions of macromolecular structures and the pharmacological compounds. Furthermore, the electrostatic potential distribution was analyzed to identify promising regions for viral attack. Molecular dynamics simulation approaches were applied, focusing on the structural components of the virus, specifically the transmembrane glycoprotein and the VP24, VP35, VP40, and nucleoprotein (NP) proteins. Using the *GROMACS 2025* modules, the results showed that the ligands — the tested drugs Ivermectin, Nafamostat, Lopinavir, and Remdesivir — maintained interactive characteristics over time. From the molecular dynamics simulations, root mean square deviation (RMSD) data of atomic positions were obtained, yielding ranges from 0.25 to 2.0 Å for Ivermectin, 0.25 to 2.37 Å for Lopinavir, and 0.25 to 7.0 Å for Nafamostat. RMSD values below 2–3 Å suggest good structural integrity and stable interactions throughout the simulation. In the results obtained from molecular dynamics, the intermolecular hydrogen bonds showed significant differences compared to the RMSD data, displaying variations in the number of hydrogen bonds during the simulation. These variations were influenced by the ligand's approach, which helps eliminate non-natural conformations during structural adjustment. Hydrogen bond analysis demonstrated that the amino acids located in the active region of VP40 established significant interactions with the three drugs. Ivermectin exhibited stronger interactions with VP24 and VP30, while Lopinavir interacted with GP2, VP24, and VP30. Nafamostat showed a high number of hydrogen bonds with all the proteins. The repurposing of these drugs against MARV may lead to potential viral antagonists, which, if confirmed by experimental studies, could contribute to reducing the mortality caused by MARV.

Key-words: Molecular Docking, Electrostatic Potential Map, MARV, Molecular Dynamics, Ivermectin, Nafamostat and Lopinavir.

Resumo

A modelagem molecular tornou-se uma ferramenta crucial no estudo de interações entre fármacos e alvos virais, permitindo a previsão de mecanismos de ligação e potenciais aplicações terapêuticas. Neste contexto, quatro fármacos foram examinados: Ivermectina, Nafamostat, Lopinavir e Remdesivir, com potenciais interações com o vírus Marburg (MARV) e exibindo características interativas eficazes, sugerindo uma forte possibilidade de serem reaproveitados na abordagem terapêutica contra o MARV. A eficácia dessas interações foi avaliada por meio de docking molecular, que calcula as posições dos ligantes ao redor da proteína alvo e as mede pela energia de ligação. Os resultados forneceram energias de ligação pela GNINA que usa Rede Neural Convolucional variando de -8,74 kcal/mol a -10,54 kcal/mol para Ivermectina, -7,37 kcal/mol a -10,46 kcal/mol para Lopinavir, -7,16 kcal/mol a -10,00 kcal/mol para Nafamostat e -6,56 kcal/mol a -9,59 kcal/mol para Remdesivir. Os complexos moleculares identificados nas simulações de docking, juntamente com suas respectivas afinidades de ligação, demonstraram o estabelecimento de interações entre aminoácidos na região catalítica das estruturas macromoleculares e os compostos farmacológicos. Além disso, analisamos a distribuição do potencial eletrostático para identificar áreas promissoras de ataque viral. Abordagens de simulação de dinâmica molecular foram aplicadas, com foco nos componentes estruturais do vírus, mais precisamente a Glicoproteína Transmembrana, as proteínas VP24, VP35, VP40 e a Nucleoproteína. Utilizando os módulos GROMACS 2025, os resultados demonstraram que os ligantes — os fármacos testados Ivermectina, Nafamostat, Lopinavir e Remdesivir — mantiveram características interativas ao longo do tempo. A partir das simulações de dinâmica molecular, dados de desvio quadrático médio (RMSD) de posições atômicas foram obtidos, fornecendo intervalos variando de 0,25 a 2,0 Å para Ivermectina, 0,25 a 2,37 Å para Lopinavir e 0,25 a 7,0 Å para Nafamostat. Valores abaixo de 2–3 Å sugerem boa integridade estrutural e interações estáveis ao longo da simulação. Nos resultados obtidos por meio da dinâmica molecular, as ligações de hidrogênio intermoleculares apresentaram diferenças significativas quando comparadas aos dados de RMSD, exibindo variações no número de ligações de hidrogênio durante a simulação. Essas variações foram influenciadas pela aproximação do ligante, que ajuda a eliminar conformações não naturais durante o ajuste. As análises de ligações de hidrogênio demonstraram que os aminoácidos localizados na região ativa de VP40 estabeleceram interações significativas com os três fármacos. A Ivermectina interagiu mais intensamente com VP24 e VP30. O Lopinavir interagiu com GP2, VP24 e VP30. O nafamostato apresentou um alto número de ligações de hidrogênio com todas as proteínas. A reutilização desses medicamentos contra o MARV pode levar a antagonistas virais candidatos, os quais, se confirmados por estudos experimentais, podem contribuir para a redução da mortalidade causada pelo MARV.

Palavras-chave: Docagem Molecular, Mapa de Potencial Eletrostático, Dinâmica Molecular MARV, Ivermectina, Nafamostat e Lopinavir

List of Figures

List of Tables

List of Abbreviations and Acronyms

Å	Angstrom (unit of distance, 1 Å = 10^{-10} m).
ADV	AutoDock Vina, molecular docking simulation software.
ANN	Artificial Neural Networks.
B3LYP	Hybrid functional of Density Functional Theory.
CNN	Convolutional Neural Networks.
DFT	Density Functional Theory.
DOC	Molecular Docking.
Fs	Femtoseconds.
GAUSSIAN 16	Computational chemistry software.
Gnina 1.3	Molecular docking software based on convolutional neural networks.
GROMACS	GROningen MAchine for Chemical Simulations.
HB	Hydrogen Bonds.
K	Kelvin.
kcal/mol	Kilocalories per mole (energy affinity unit).
MARV	Marburg Virus.
MD	Molecular Dynamics.
MEP	Molecular Electrostatic Potential.
nM	Nanomolar.
ns	Nanoseconds.
RMSD	Root Mean Square Deviation.
UFPA	Federal University of Pará.

Summary

1 INTRODUCTION

1.1 Context and Motivation

Life expectancy has increased, in part, due to new strategies to combat diseases and improved quality of life. Among these reasons is the development of medications used to diagnose and treat diseases or control various illnesses [1–3]. However, research and analysis of new pharmaceutical compounds are extremely complex processes and require significant investments of both time and financial resources [4].

The pharmaceutical trade relies heavily on multimillion-dollar investments in instruments, materials, labor, and distribution; in adverse situations, these costs can reach billions. Over the last decade, investments in the study, development, and advancement of new treatments have grown [5]. Research indicates an increase in the production of new therapeutic compounds on the market across various sectors. Meanwhile, pharmaceutical revenues have been increasing at an annual rate of 5.8% since 2017. [6]. These increases in drug production can be attributed to several factors, including the development of new forms of drug production, clinical trials, the adoption of new methodologies, and the application of conventional strategies [7, 8].

The global pharmaceutical market has been seeking to reduce its drug production costs, with a focus on pursuing efficient drug development strategies in recent years, aiming to minimize the selection of less effective drugs [9–11].

Thus, new computational tools and their developments are becoming increasingly valuable for both the industrial and academic sectors. They can be applied at any stage of the manufacturing process. Various techniques can be developed and employed in rational drug development, including computational drug development, molecular docking (MDOC), and the prediction of aspects such as toxicity, bioavailability, and other factors. [12]. Computational approaches are highly effective in the pharmaceutical field, but they still require rigorous evaluation of the effectiveness of the results obtained, due to certain constraints, such as the accuracy of experimental investigations, computational cost, the great complexity involved in the computational calculations performed, and the challenges in representing certain interactions, particularly intermolecular ones.

Between late January and early February 2023, new outbreaks of Marburg virus were reported in Equatorial Guinea, which exhibits diverse structures, as shown in Figure 1 [13]. A total of nine cases (four probable, one confirmed, and four suspected) were reported, all resulting in death. The confirmed patient presented severe symptoms of seizures, fever, vomiting, and a severe case of bloody diarrhea, and died of the disease in February 2023 [14]. This generated significant local and global social attention due to the high mortality rate of the disease, ranging

from 25% to 90% depending on the recorded location of incidence, and its effective spread. The first known cases of Marburg virus occurred in 1967 in the German cities of Marburg and Frankfurt, when laboratory technicians handling contaminated monkey blood became infected. This initial outbreak resulted in 31 human cases and 7 deaths, marking the discovery of the virus. Since then, Uganda has recorded several outbreaks, including those from 2007 to 2014, with case fatality rates ranging from 25% to 75%, depending on the year and health response conditions. The largest outbreak recorded globally occurred in Angola between 2004 and 2005, with 442 cases and 356 deaths, representing a case fatality rate of over 80%, making it the most severe episode in the history of the disease. These outbreaks highlight the high mortality potential of Marburg virus and the importance of effective preventive and therapeutic strategies to contain future epidemics [15].

To combat new outbreaks, research related to materials science is of central importance, aiming to develop advanced technological solutions and accessories for sensor analysis, antiviral compounds, and treatment approaches targeting the Marburg virus (MARV) [16]. One approach to examining this topic is through computer simulations [17], which utilize correlated data, employing Molecular Modeling (MM) based on docking analyses and molecular dynamics (MD) simulations [18]. The molecular docking (MDOC) approach is a crucial and important tool for evaluating the potential interrelationships between molecules, such as in the case of biomacromolecules. Docking is a crucial technique for examining molecular affinity, specifically for large biological molecules. Although DOC estimates are extremely useful tools, they do not provide data on the MD of complexes involving ligands and biomolecules [19].

By performing molecular docking modeling, we can monitor and analyze the movement of arrangements over different time frames [20]. This enables diagnostics related to rapid internal dynamics and slow conformational changes, important in complex mechanisms, including the interaction of ligands with active sites or protein folding. [20]. The use of DOC in the pharmaceutical sector continues to increase, making it nearly impossible to enumerate all its applications. The combination of laboratory and computational methods provides a deeper understanding of intermolecular interactions and is a crucial tool for identifying viral sensors and inhibitors [21]. Currently, the safest and most effective way to deliver medicines quickly is through the therapeutic repurposing of drugs already on the market.

These technological procedures have the potential to be used in the strategic development of compounds, based on a logical hypothesis about their mode of action. Molecular modeling tools aim to monitor and examine these interactions, as well as characterize previously uncharacterized interactions and structures of interacting biomolecules. Therefore, it is crucial that the combination of DOC and MD provides reliable results.

The lack of exclusive and effective antiviral treatments to combat the Marburg virus, coupled with its high fatality rate, constitutes a relevant motivation for this work. Molecular modeling tools aim to monitor and examine these interactions, as well as predict and characterize

interactions and previously uncharacterized structures of interacting biomolecules. Scientific advances in virus research and the development of potential drugs are relevant to the creation and production of new medications and pandemic control strategies. Viral research using computational techniques (MD and DOC) allows for the analysis of drugs that reduce or completely neutralize viral activity.

1.2 Justification

Despite the severity of the virus, no approved antivirals or vaccines are currently available, representing a threat to global public health [22, 23]. In this context, *in silico* approaches have been employed as strategies to accelerate drug discovery and repurposing.

Recent studies have demonstrated the potential of these methodologies. Alsaady et al. (2023) applied cheminformatics to identify inhibitors of the VP35 protein, using molecular docking and modeling to analyze specific interactions [22]. Natural compounds, such as procyanidin, have also demonstrated high affinity for VP40, as validated by MD simulations and metrics, including RMSD, RMSF, and hydrogen bond counts [24], studies are already indicating their evolution with the use of artificial intelligence [25]. In the clinical context, Remdesivir, either alone or in combination with monoclonal antibodies, demonstrated modest efficacy in post-exposure prophylaxis protocols, whereas obeldesivir achieved up to an 80% survival rate in non-human primates following lethal exposure.

In this work, we conducted virtual screening of multiple MARV structures using Ivermectin, Lopinavir, Nafamostat, and Remdesivir, drugs already approved for other indications. The computational tools were selected based on their scientific relevance and computational performance. The analysis includes DOC to identify affinities and binding sites, as well as molecular dynamics simulations to evaluate temporal stability, RMSD, and intermolecular interactions. Molecular Electrostatic Potential were employed for binding analysis. AutoDock Vina, which relies on classical physics equations, and Gnina, which employs a convolutional neural network for docking, were used, along with Gaussian 16 for molecular dynamics. This strategy is grounded in evidence from the literature and aims to contribute to the identification of repurposable compounds with therapeutic potential against MARV.

1.3 Objectives

1.3.1 General Objective

Utilize molecular docking and molecular dynamics methods to investigate the interaction of potential drugs with Marburg virus structures, aiming to identify therapeutic agents that can combat infection by this virus.

1.3.2 Specific Objectives

- **Perform Molecular Docking Simulations:** Use computational tools such as AutoDock Vina and Gnina (with neural network) to model and predict the interaction of candidate drugs with Marburg virus structures, identifying the most favorable binding regions and affinities.
- **Analyze Docking Tools:** Verify which docking tool produced the best results using Discovery Studio Visualizer 4.5, and based on this, initiate the molecular dynamics process with Gaussian 16.
- **Perform Molecular Dynamics:** Analyze the results obtained through RMSD calculations and hydrogen bond analysis to evaluate the stability of interactions and their potential impact on viral activity.
- **Evaluate Drug Potential:** Determine, based on the results of docking (DOC) and molecular dynamics (MD), which drugs show the highest potential to block Marburg virus binding and host cell invasion.
- **Propose New Research Directions:** Suggest new pathways and strategies for research and development of antivirals or sensors against the Marburg virus based on the study results.

1.4 Document Structure

Chapter 1 presented the Introduction and Rationale for the research, as well as the main objectives. Chapter 2 presents a literature review on key topics relevant to this work, including: What is a virus? We analyze the Marburg virus in more detail and present the drugs under study. Chapter 3 presents docking and molecular dynamics. Chapter 4 develops the methodology used. Chapter 5 presents the results obtained. Chapter 6 presents the conclusions and suggestions for further development of this line of research. This dissertation is divided into six chapters.

2 THEORETICAL FRAMEWORK

2.1 Initial Considerations

This chapter exemplifies the main topics for the continuation of this dissertation. The section begins by demonstrating the fundamental concepts of viruses, demonstrating their mode of infection and the main aspects that differentiate them from other biological organisms. It then explains the Marburg virus, its discovery, structure, replication mechanisms, and infection. We then discuss the concept of antiviral drugs and compounds, followed by the three medications selected for the study.

2.2 General Concept of Viruses

Viruses are small, cellless organisms that have the ability to invade host cells and reproduce through replication. They lack their own metabolism and the necessary structure for protein synthesis, and fall into the category of obligate intracellular parasites. In this case, they fall into an ambiguous category between what is a living being and what is not, often described as "on the border between life and non-life" [26].

In simplified terms, its structure presents a genome (which may be made up of RNA or DNA, have a double or single strand, be segmented or non-segmented) surrounded by a protein capsid, with the function of protecting the genetic material and aiding entry into host cells.

Viral infection begins with the attachment of the virus to the host cell. This process is aided by interactions between the virus's specific proteins and receptors on the cell surface. Only after this entry does the virus release its genetic information and use the cellular structures for viral replication. This can lead to host cell death, local inflammation, and in some cases, serious pathological conditions.

Studying the structure and reproduction of viruses is important for developing vaccines, antivirals, and preventative measures. Research into these aspects becomes even more critical in the case of highly lethal viruses like Marburg.

2.3 The Marburg Virus

The Marburg virus (MARV), of the Filoviridae family, of the Marburgvirus genus, is one of the most lethal pathogens known. It causes an acute hemorrhagic fever with a high mortality rate in humans. It was discovered in 1967 during outbreaks in the cities of Frankfurt and Marburg,

Germany, and in Belgrade, in the former Yugoslavia, through the manipulation of monkey cells imported from Uganda for biomedical research [27].

2.4 Viral Morphology and Structure

The Marburg virus has a virion diameter of approximately 80 nm and a length that can exceed 1,000 nm. It can assume linear, branched, or U-shaped or 6-shaped forms. It also has a filamentous structure, a characteristic quite common in filoviruses [28]. Its structure is composed of:

- Lipid envelope: Formed from the host cell's plasma membrane, the viral envelope contains the glycoprotein (GP), essential for the host cell invasion stage.
- Nucleocapsid: Composed of single-stranded RNA, it is coated with specific proteins that confer a rigid complex.
- Structural proteins: include GP, VP24, VP30, VP35, VP40, NP, and RNA polymerase L.

Each of these structures plays fundamental roles in the viral cycle:

- NP (Nucleoprotein): surrounds and protects the viral RNA, forming the core of the nucleocapsid.
- VP35: acts as a cofactor of RNA polymerase and inhibits the innate immune response.
- VP40: main matrix protein, involved in viral budding.
- GP (Glycoprotein): the only surface protein, responsible for receptor binding and membrane fusion.
- VP30: regulates viral RNA transcription.
- VP24: assists in the assembly of the nucleocapsid.
- L (Polymerase): catalyzes the replication and transcription of the viral genome.

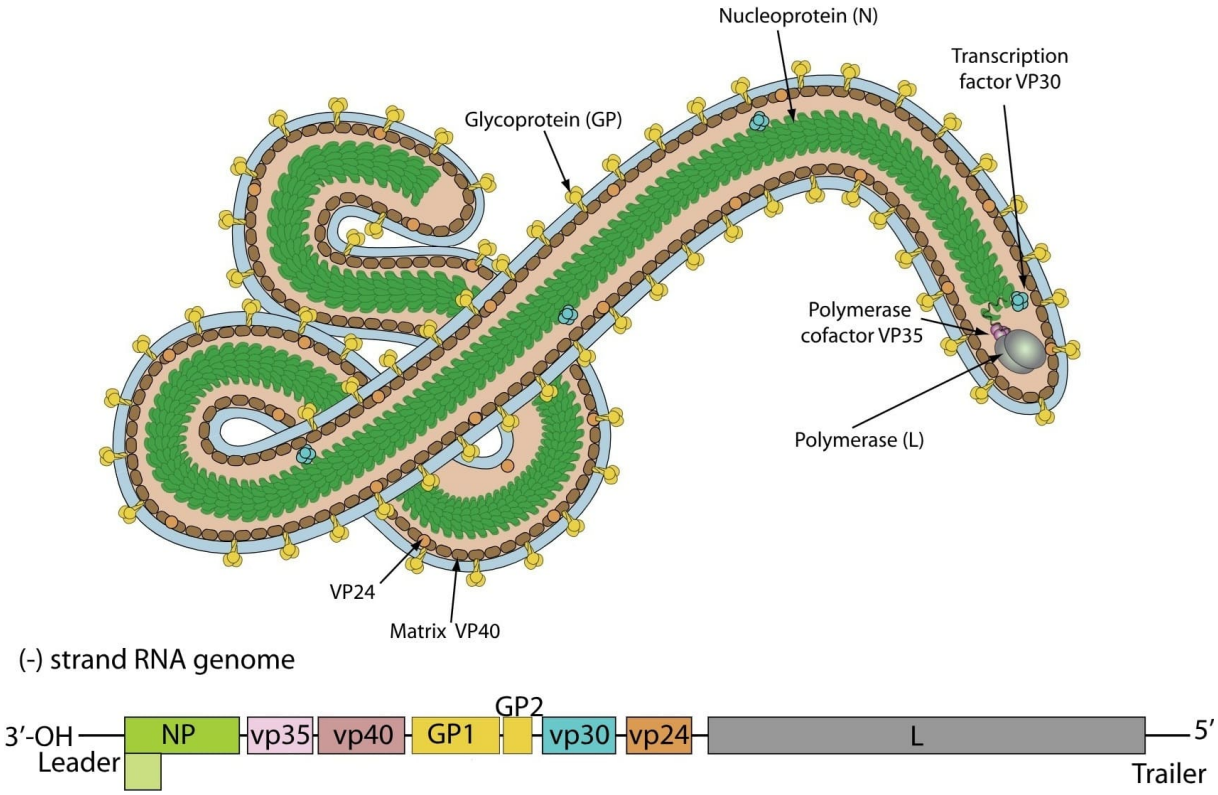

Figure 1 – Structures of the Marburg virus.
Source: Adapted from Swiss Institute of Bioinformatics [13]

2.5 Viral Structures from Research

2.5.1 Transmembrane Glycoprotein (GP2)

The 4g2k code structure, present in the Protein Data Bank (PDB), Figure 2a, is related to the ectodomain of the GP2 subunit of the MARV virus. It presents characteristics of enveloped and single-stranded negative RNA viruses. Its entry is directly related to the virus's characteristic of invading the host cell, this mechanism aided by the fusion of the cellular and viral membranes, which is assisted by the envelope glycoprotein (GP), which has two subunits in its structure: the surface glycoprotein (GP1), which is responsible for binding to the cellular receptor, and GP2, responsible for catalyzing membrane fusion [29].

GP2 possesses regions of extremely important structures that influence fusion, notably two heptad repeats, one located in the C-terminal region (CHR) and the other in the N-terminal region (NHR). During fusion, these regions modify to form a highly stable six-helix bundle, a structure that attracts the viral and cellular membranes, overcoming the energy barriers involved in lipid bilayer fusion. The 4g2k structure describes this post-fusion state of MARV GP2, obtained at 1.9 Å resolution. The conformation presented is highly similar to that previously observed for Ebola virus GP2, revealing an architecture in which a central NHR trimer packs

against peripheral CHR helices, stabilized by additional interactions, including an intermediate loop/helix-turn-helix segment.

Furthermore, studies demonstrate that the stability of its post-fusion conformation is closely related to the pH level, being favored in acidic regions, such as those located in mature endosomes of host cells. This particularity is directly related to an "anion band"in the central region of the structure, composed primarily of acidic residues that enable stabilizing interactions at low pH. This pH dependence is characterized as a critical regulatory mechanism and allows membrane fusion to occur only in appropriate cellular compartments, thus avoiding premature activation of the complex responsible for fusion [29].

The 4g2k conformation provides detailed information regarding the molecular mechanism of fusion mediated by the Marburg virus GP2 glycoprotein. It describes the post-fusion conformation, an indispensable component for viral invasion, and is a crucial model for the development of inhibitors that block this critical step in the filovirus infection process [29].

2.5.2 VP35 Protein

The crystal structure of MARV VP35 (PDB code 4gh9), Figure 2b, shows the conformations and interactions linked to the binding of the VP35 protein to double-stranded RNA (dsRNA), which is generally associated with viral infections, detected by infected cells as a warning signal. The viral genetic content in the form of RNA activates host immune sensors, such as RIG-I and MDA-5, initiating an immune response that incorporates the production of interferons (IFNs) to prevent viral infection.

The RBD domain of VP35 is responsible for hiding the dsRNA, making it difficult for the infected organism to detect it. The 4gh9 structure shows that the RBD domain of VP35 completely covers the sugar-phosphate backbone of the dsRNA, forming a continuous coating along the entire length of the RNA. Furthermore, VP35 can cap the ends of the dsRNA, preventing complete detection of the dsRNA, resulting in evasion of host immune surveillance [30].

The uninterrupted coating along the entire length of the dsRNA backbone and end capping are important features of viral RNA camouflage structures, preventing the activation of host immune pathways, such as interferon (IFN) signaling. This is one of the most important ways in which MARV suppresses the host's immune response, thus allowing infection. VP35 is located within the MARV structure, more precisely in the nuclear region of the virus, demonstrating how it binds to the viral dsRNA, creating an immune evasion mechanism by coating the dsRNA and capping its ends, preventing detection by the host's immune surveillance molecules [30].

2.5.3 VP24 Protein

The VP24 protein, Figure 2c, does not demonstrate immunosuppressive abilities (a characteristic present in other *filoviruses*), but is related to the viral nucleus and the ribonucleoprotein

complex (RNP), is crucial for viral multiplication and plays an important role in the construction of viral structures and in viral transcription. It is represented by the 4or8 structure present in the PDB and reveals that the protein component adopts a general single-domain form α/β, with a pyramidal shape [31]. The N-termini present in the MARV VP24 protein are vital for the construction of the nucleocapsid; the structure demonstrates its effectiveness when analyzing the protein's relationships in the viral cycle. This is of interest when evaluating new, effective antiviral drugs that have the ability to inhibit the generation of new viral particles or interfere with the metabolic processes that allow the virus to multiply [31].

Furthermore, the configuration of VP24 provides powerful and fundamental information about the functioning and arrangement of the virus, providing a solid foundation for future studies on the virus's life trajectory and for the development of effective antiviral drugs against this pathogen [31].

2.5.4 VP40 Protein

VP40, Figure 2d, plays an important role in inducing hatching, especially in the formation of viral particles by manipulating the host cell. During this process, the arrangement of VP40 allows it to interact with the GP and cellular components, such as the plasma membrane, facilitating the virus's exit from the infected cell.

Furthermore, VP40 has the ability to exert an immunosuppressive function by binding to the signaling of interferons (IFNs), structures essential for the host's immune response. In the case of MARV, VP40 inhibits the phosphorylation of proteins involved in interferon signaling, contributing to a decrease in communication with the host's immune system [32].

The 5b0v structure is relevant to the structural and immunosuppressive role of MARV's VP40. Its location in the viral matrix plays a central role in the assembly and release of new viral structures, in addition to blocking the host's immune response [32].

2.5.5 Nucleoprotein (NP)

NP, Figure 2e, acts as a fundamental protein in the viral life cycle, performing the function of encapsulating the RNA genome, forming the ribonucleoprotein (RNP). Like other filovirus NPs, it adopts a typical bilobed conformation with an RNA-binding groove. This groove is positively charged, allowing the NP to bind to viral RNA. This characteristic is essential for the emergence of the RNP that coats and protects the viral genetic code, in addition to enabling its transcription and reproduction [33].

The 5f5m structure reveals the hexameric state of the NP structure (without RNA or other bound cofactors), an important feature in the context of protein oligomerization. This hexameric characteristic is maintained by hydrophobic bonds within the C-terminal helix of the NP, suggesting it is crucial for the assembly phase of the RNP complex. Its high flexibility in

the structural phase allows the NP to modify itself to accommodate viral RNA and facilitate the assembly of the viral complex. The MARV NP, described by the 5f5m structure, is located within the viral core, where it interacts with various structures of the RNP complex, such as the RNA-templated RNA polymerase (RdRp) and the VP24 and VP30 proteins, to aid in the replication and synthesis of viral RNA [33].

Furthermore, the structure of MARV has been examined in the presence of the VP35 peptide, classified as one of the viral proteins that aid in the elaboration of the RNP. The VP35 peptide inhibits the binding of NP to viral RNA, forcing the NP to remain in a monomeric form. This structural transformation is important because it causes the organization of the connection between the NP and the viral RNA, a characteristic that helps in the reproduction of the virus.

2.5.6 Communication between Phosphoprotein VP30 and Nucleoprotein NP in MARV

The complex structured by VP30-NP, Figure 2f, modulates the action of viral RNA synthesis and its regulation. Structure 5t3w shows changes in the interaction between VP30 and NP, revealing changes in viral replication rates. This suggests that the VP30-NP complex exerts some control over the viral replication stage, quite possibly adjusting the rates of viral RNA reproduction and synthesis to the needs of the host cell. The PDB lists the protein associated with the 5t3w code. It demonstrates, through the VP30 phosphoprotein and NP, that it is located within the viral nucleocapsid. During the MARV life cycle, NP and VP30 interact in the viral nucleus, where VP30 initiates transcription and regulates the multiplication of viral ribonucleic acid [34].

The 5t3w conformation provides important insights into the interaction between the VP30 phosphoprotein and the MARV NP nucleoprotein. The molecular binding of this protein is essential for the control, transcription, and multiplication of viral RNA and contributes to MARV RNA synthesis. It also offers insights into the development and development of new antiviral drugs that can combat or inhibit the VP30-NP interaction, blocking viral replication and aiding in the treatment of filovirus infections.

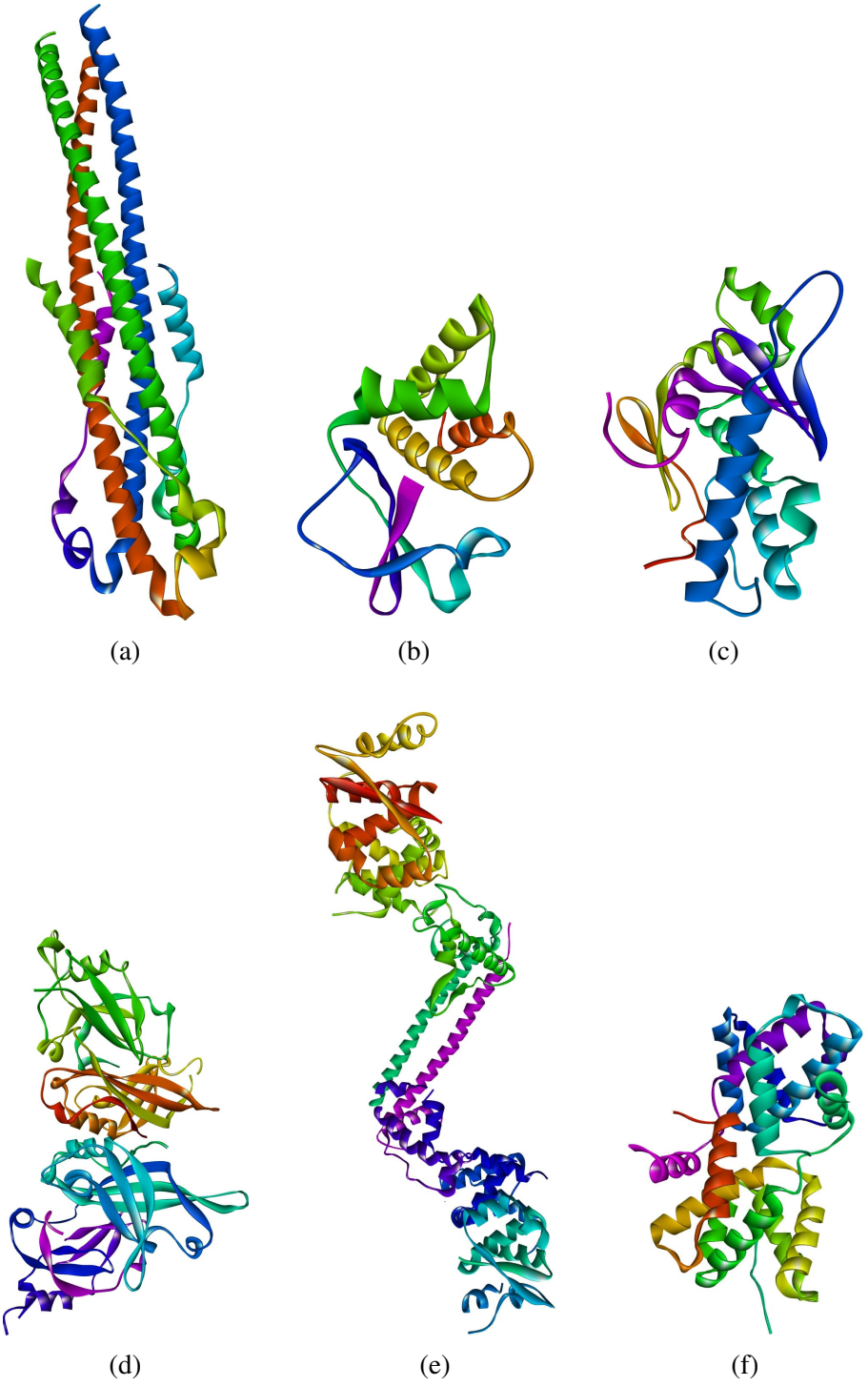

(a) (b) (c)

(d) (e) (f)

Figure 2 – Macrostructures used: (a) GP2; (b) VP35; (c) VP24; (d) VP40; (e) NP; (f) VP30.

Source: RCSB Protein Data Bank [35].

2.6 Drugs and Antivirals

These are biological or chemical compounds that can interact with the biological system, in physiological or pathological processes, with the function of preventing, alleviating, or treating diseases. They act through interactions with specific molecular targets, such as proteins, enzymes,

receptors, or nucleic acids, altering their biochemical functions.

Within this characteristic, antivirals are medications designed to inhibit the reproduction of viruses in the host organism. Unlike antibiotics, which combat bacteria, antivirals combat pathogens that depend on the host's cellular machinery for replication. Therefore, these compounds must be able to interfere with crucial stages of the viral cycle—such as cell entry, genome replication, viral particle assembly, or virus release—while minimizing damage to host cells.

The development of antivirals is, therefore, a complex process that seeks to balance efficacy in viral inhibition with selectivity, in order to reduce side effects and toxicity. The medications selected for the study are presented below:

2.6.1 Ivermectin

In the late 1970s, through a scientific collaboration between Satoshi Ōmura and William C. Campbell, Ivermectin was discovered (Figure 3a). Beginning in 1987, the drug began to be used to treat onchocerciasis in humans [36, 37]. Recent research indicates that Ivermectin has antiviral potential, with interactions observed with the COVID-19 virus. Laboratory trials have demonstrated antiviral effects at doses between 3 and 6 nM against the yellow fever virus [37].

At higher concentrations (200–300 nM), Ivermectin was effective against other flaviviruses, such as Japanese encephalitis and tick-borne encephalitis, suggesting interference with the viral replication process [37].

Ivermectin's antiviral action appears to be associated with inhibition of the Importin α/β_1 complex, responsible for transporting viral proteins to the cell nucleus. This mechanism has the potential to interfere with several RNA viruses, including those of the *Filoviridae* family, such as Marburg. Molecular docking studies support this hypothesis, indicating binding to structural and non-structural viral proteins, in addition to the drug's ability to efficiently cross cellular compartments.

2.6.2 Lopinavir

Lopinavir, Figure 3b, is a protease inhibitor (PI) antiretroviral widely used in the treatment of HIV-1 infection. It acts by inhibiting viral protease, preventing the cleavage of viral polyproteins and, consequently, viral maturation. Thus, it reduces viral infectivity without affecting already infected cells [38].

The drug has in vitro activity approximately 10 times greater than that of ritonavir, although its in vivo efficacy is reduced due to high hepatic metabolism. Therefore, it is commonly administered in combination with ritonavir, which acts as a pharmacokinetic enhancer [38].

In addition to its classic use against HIV-1, Lopinavir has been investigated against several RNA viruses. During the COVID-19 pandemic, it was used in experimental clinical trials.

Studies suggest it may inhibit proteases from other viruses, such as Ebola and Marburg, whose replication depends on similar enzymatic processes. Prior knowledge of pharmacodynamics and safety facilitates its application in emergency settings [38].

2.6.3 Nafamostat

Nafamostat, Figure 3c, was developed in the 1980s by Ono Pharmaceutical, initially for the treatment of disseminated intravascular coagulation and acute pancreatitis. It acts as an inhibitor of serine protease, an enzyme involved in inflammation and coagulation processes [39, 40].

Currently, Nafamostat is being studied as an antiviral, particularly for its effectiveness against viruses that use the TMPRSS2 protease to infect human cells, such as SARS-CoV-2. Inhibiting this enzyme prevents the activation of the spike protein, crucial for the fusion of the virus with the cell membrane [41].

Although Marburg utilizes distinct mechanisms, it is believed to also rely on host proteases to activate its GP glycoprotein and facilitate endosomal fusion. In silico simulations suggest that Nafamostat may inhibit this process, blocking viral entry. Furthermore, its antiprotease action may modulate the exacerbated inflammatory response characteristic of hemorrhagic infections [41].

2.6.4 Remdesivir

Remdesivir, Figure 3d, is a broad-spectrum antiviral drug originally developed by the biopharmaceutical company Gilead Sciences to treat infections caused by the Ebola virus and other viruses in the Filoviridae family. Its development dates back to the early 2010s, during efforts to find effective therapies against highly lethal and emerging pathogens. Chemically, Remdesivir is a nucleotide analog that acts by inhibiting viral RNA-dependent RNA polymerase, an enzyme essential for the replication of several RNA viruses [42, 43].

Although Remdesivir did not achieve the expected clinical performance during the Ebola outbreaks, subsequent studies demonstrated that it exhibited antiviral activity against a broad range of RNA viruses, including coronaviruses, leading to its investigation and subsequent emergency use during the COVID-19 pandemic in 2020. Remdesivir has therefore become a leading candidate for a broad-spectrum antiviral drug [44].

Recently, in silico and in vitro research has investigated the efficacy of Remdesivir against MARV, another filovirus responsible for hemorrhagic fevers with a high mortality rate. [45] Studies indicate that, due to its conserved mechanism of action, Remdesivir has the potential to inhibit MARV replication, making it a promising option in the therapeutic arsenal against this emerging pathogen [46].

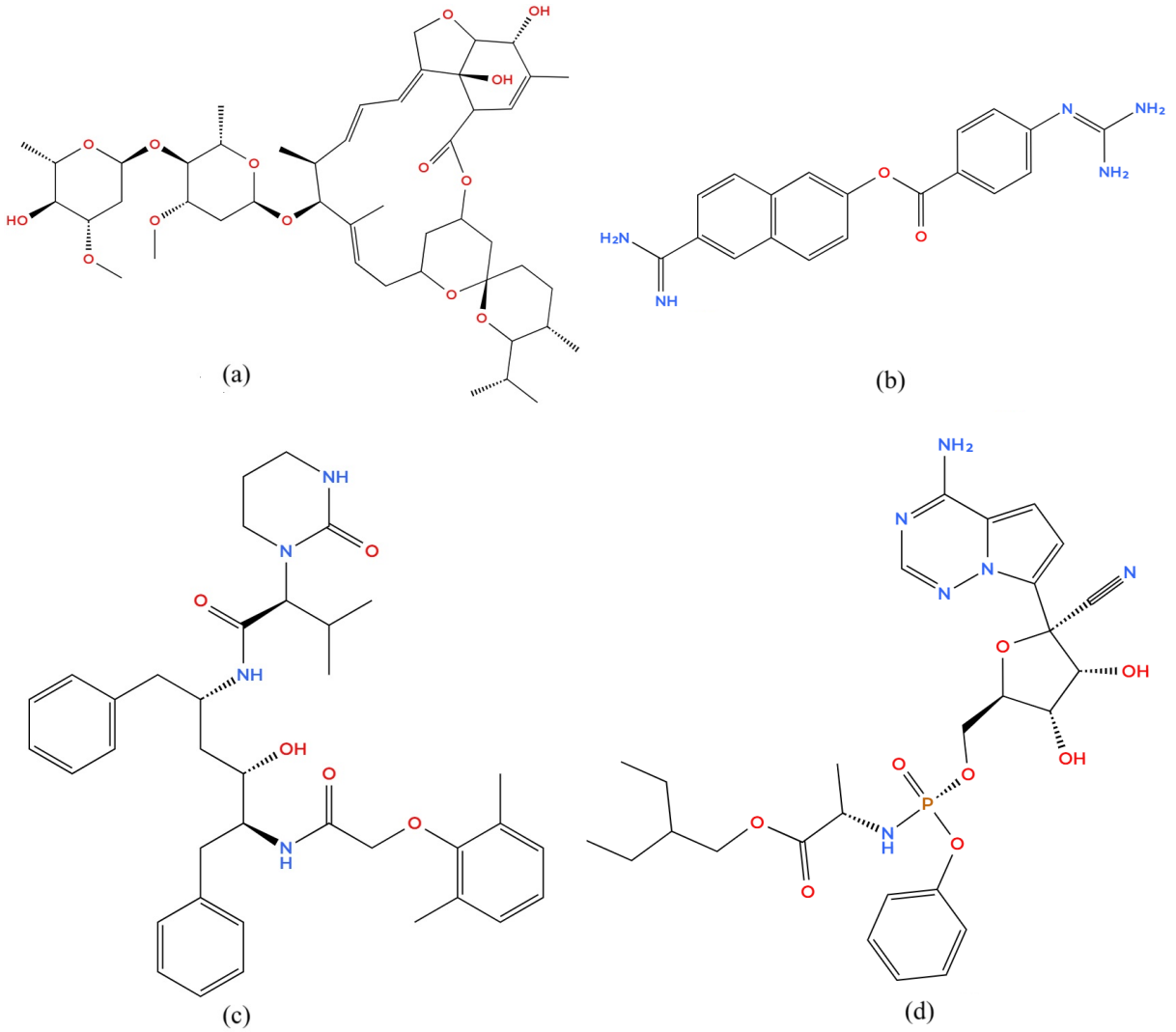

Figure 3 – Structure of the compounds under study (a) Ivermectin, (b) Nafamostat, (c) Lopinavir, and (d) Remdesivir.

Source: National Center for Biotechnology Information [47], MolView [48].

2.6.5 Comparison of Mechanism of Action

The four pharmaceutical compounds investigated act at different stages of the viral replication cycle. Ivermectin interferes with the nuclear import of proteins, Lopinavir inhibits viral maturation by blocking proteases, Nafamostat prevents viral entry by inhibiting host proteases, and Remdesivir acts by inhibiting an enzyme essential for RNA virus genome replication. This diversity of mechanisms strengthens the hypothesis of joint or complementary action against highly lethal viruses like Marburg.

The in silico evaluation of each drug against Marburg target proteins (such as GP2, VP24, VP35, and NP) is a fundamental step in screening compounds with antiviral potential. The analysis includes binding affinity, conformational stability, and free energy of binding, providing support for future experimental testing.

2.7 Chapter Summary

This chapter presented the essential theoretical foundations of viruses, with an emphasis on MARV, a highly lethal agent belonging to the Filoviridae family. Initially, the concept of viruses as obligate intracellular parasites was discussed, lacking their own metabolism and whose replication depends on the host cell. Their structural characteristics, including the genome, capsid, and, in some cases, a lipid envelope, were addressed.

The molecular biology of MARV was then detailed, covering historical aspects, filamentous morphology, and mechanisms of infection and replication. The functions of the main structural proteins were described, such as the glycoprotein GP2, essential for viral fusion; VP35, which plays a role in evading the immune system; VP24, involved in nucleocapsid assembly; VP40, which facilitates the formation and release of viral particles; as well as the NP nucleoprotein and the VP30-NP complex, both essential for viral RNA transcription and replication.

Additionally, the pharmaceutical compounds selected for this study —Ivermectin, Lopinavir, Nafamostat, and Remdesivir— were presented, highlighting their histories of use, clinical applications, and known mechanisms of action. Recent studies reinforce the antiviral potential of these drugs against various viruses, including those with infection mechanisms similar to those of MARV.

The information systematized in this chapter provides the scientific basis for the virtual experiments developed in this research, in addition to informing the choice of compounds and guiding the in-depth computational analyses presented in subsequent chapters.

3 MOLECULAR MODELING

3.1 Initial Considerations

Molecular modeling (MM), developed using computational and theoretical resources, focuses on investigating the structural and functional properties of molecules. This chapter demonstrates the techniques used in drug research and the MARV structures, the Density Functional Theory (DFT) technique, Molecular Docking, Molecular Electrostatic Potential (MEP), Classical Molecular Dynamics (MD), and Convolutional Neural Networks (CNNs). These methodologies demonstrate an analysis of structure and dynamics, with concepts from quantum chemistry, classical mechanics, and artificial intelligence.

3.2 Density Functional Theory

Density functional theory (DFT) [49] is one of the best-known and most effective quantum models widely used in the study of intermolecular properties. This method of calculation allows for the acquisition of theoretical solutions that often agree with laboratory data, enabling an understanding of the microscopic world, as well as its unique characteristics and the electronic and physical properties of the analyzed bodies. An important feature of DFT is the fundamental application of functionals, which can be understood as a function that is subordinate to another function because it is dependent, in this case, the electron density.

The total energy of a molecule is represented by the electron density function ρ used through the equation:

$$\text{Energy} = F[\rho(x, y, z)]. \tag{3.1}$$

The main purpose of the DFT is to establish this functional F. According to Kohn-Sham [50], the energy of the system can be divided by the sum of the contributions presented below:

$$E_{\text{DFT}} = T(\rho) + E_{\text{ne}}(\rho) + J(\rho) + E_x(\rho) + E_c(\rho), \tag{3.2}$$

The term E refers to the total energy, E_{ne} is equivalent to the Coulomb energy of attraction between the nuclei and electrons, E_x and E_c refer to the exchange and correspondence energies between the electrons, J is defined as the aversion energy between the electrons, and T is the energy of electron motion.

Each term in this equation represents a function of the electron density ρ and is known as a functional, which is the core of the DFT approach. The first three terms (T, E_{ne}, and J) can be calculated with reasonable accuracy using semi-empirical or ab *ab initio* methods [50]. However, contributions related to electron exchange and correlation are treated differently within DFT.

The B3LYP functional (Becke, three-parameter, Lee–Yang–Parr), widely employed in Density Functional Theory (DFT) studies, is a hybrid functional that combines the Hartree–Fock (HF) exchange with the Becke's exchange correction (B88) and the Lee–Yang–Parr (LYP) correlation terms. This combination allows a more realistic representation of electronic correlation effects, providing an effective balance between accuracy, computational cost, and numerical stability. B3LYP is particularly effective for molecular systems composed of light elements such as hydrogen, carbon, oxygen, and nitrogen, and it is extensively used for the calculation of optimized geometries, binding energies, and vibrational frequencies [51, 52].

In the calculations carried out in this dissertation, the 6-31G basis set was employed. This set, part of the Pople split-valence Gaussian basis sets, describes the inner-shell orbitals using six contracted Gaussian functions, while the valence orbitals are represented by two combinations of Gaussian functions (three and one, respectively). Such configuration provides a flexible and efficient description of the electronic distribution, making the 6-31G basis particularly suitable for organic molecules and small biomolecular systems, offering a reasonable compromise between computational efficiency and theoretical accuracy [52].

3.3 Molecular Docking Modeling

Molecular docking (DOC, Figure 4) is a computational method whose main goal is to predict how small molecules, called ligands, interact and the affinity of these interactions within the active site of a target protein. This process usually involves estimating the interaction energy using specific scoring functions. [53].

For calculations to be feasible, it is essential to strike a balance between the accuracy of the results and the required computational time, which poses a considerable challenge in the field. The reversible interaction between a ligand (L) and a receptor (R), forming a ligand-receptor complex (RL), can be described by the chemical reaction shown in Equation (3.3):

$$[R] + [L] \rightleftharpoons [RL], \tag{3.3}$$

and the association constant (K_A), which expresses the binding affinity, is defined by:

$$K_A = \frac{[RL]}{[R][L]}. \tag{3.4}$$

The variation in binding free energy (ΔG) is related to K_A according to the equation:

$$\Delta G = -RT \ln K_A, \tag{3.5}$$

where R is the ideal gas constant (J/mol K) and T is the absolute temperature (K).

In molecular docking simulations, the focus is on estimating ΔG, allowing the classification of ligands according to their affinity for the active site. This technique, which emerged in the 1980s and has evolved significantly since then, has become a fundamental tool in drug development [54]. MDoc is effective in rapidly analyzing large libraries of compounds, identifying those that can modulate the biological activity of target proteins or enzymes, making it indispensable for virtual screening [55].

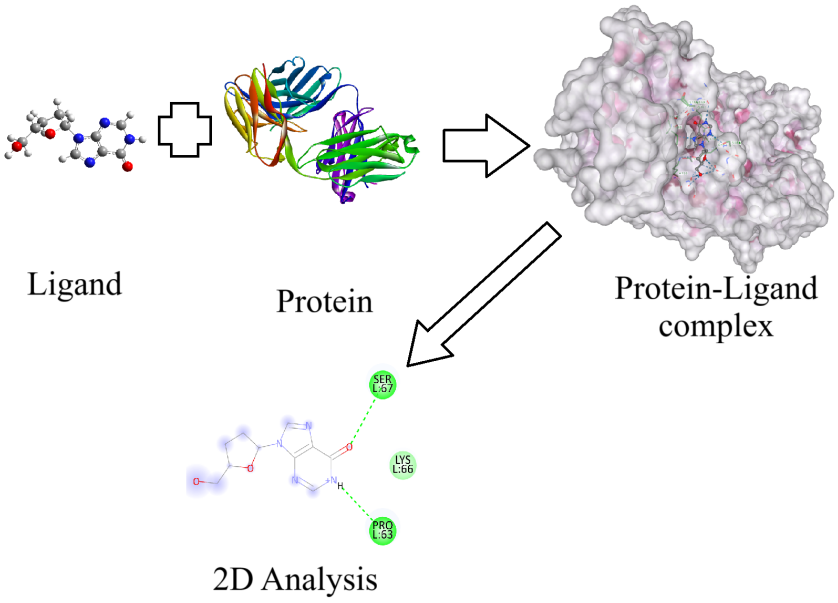

Figure 4 – Example of Molecular Docking

Source: Author.

However, a common trade-off exists between the accuracy of the results and the speed of the algorithms employed. The complexity lies in the need to explore the vast spatial conformation of the ligands and the possible structural changes of the protein during the interaction. DOC is based on the "lock and key"principle, predicting the orientations and adjustments that ligands make to accommodate themselves in the active site. It is widely used in structural modeling and biological activity prediction studies [56].

Furthermore, docking methods evaluate receptor-ligand complex formation and associated energies, classifying compounds according to their affinity. One of the difficulties is dealing with the flexibility of both the ligand and the protein, since the structural degrees of freedom can vary greatly, posing a challenge to current algorithms [57].

The approach to addressing this flexibility can vary depending on the model adopted: (i) considering the protein rigid and exploring only rotational and translational movements of

the ligand; (ii) assuming the protein rigid but allowing greater flexibility of the ligand; or (iii) treating both protein and ligand with varying degrees of flexibility [58].

The parameterization of scoring functions, which quantify the affinity of interactions, is complex, as it involves several mathematical approximations and molecular terms [59]. In general, an increase in the number of parameters analyzed improves accuracy but also increases computational cost, requiring a balance between these factors [60].

Scoring functions can be classified as force-field-based, empirical, knowledge-based, or consensus-based. Force-field-based functions calculate binding and non-bonding terms to estimate the interaction energy [61]. Ligand-receptor interactions are generally described by Van der Waals forces, calculated via the Lennard-Jones potential, and electrostatic interactions, modeled by a formulation similar to Coulomb's law that depends on the distance between charges [62].

However, these functions have limitations, such as the absence of entropic and solvation terms, in addition to the need to define cutoff distances to account for non-bonded relaxations, which makes it difficult to fully model the effects involved in molecular binding [63].

3.4 Electrostatic Potential Map

The Electrostatic Potential Map (MEP) is a key concept that will be explored in this research to relate the structural activity of the studied inhibitors to their electrostatic characteristics. Visualizing the MEP allows us to estimate relevant information about the molecules, especially regarding the interaction between ligands and receptors. For the analyzed molecules, the electrostatic potential at a point in space, $V(\mathbf{r})$, is calculated by the expression:

$$V(\mathbf{r}) = \sum_A \frac{Z_A}{|\mathbf{R}_A - \mathbf{r}|} - \int \frac{\rho(\mathbf{r}')}{|\mathbf{r}' - \mathbf{r}|} d\mathbf{r}', \tag{3.6}$$

where $\rho(\mathbf{r}')$ represents the electron density of the molecule at position $\mathbf{r}'$, Z_A is the nuclear charge of atom A located at $\mathbf{R}_A$, and the integration is carried out over all electronic coordinates $\mathbf{r}'$.

In this expression, Z_A is a constant scalar value corresponding to the atomic number of nucleus A, while $\mathbf{R}_A$, $\mathbf{r}$, and $\mathbf{r}'$ are position vectors that define the spatial coordinates of the nuclei and electrons. The term $|\mathbf{R}_A - \mathbf{r}|$ denotes the scalar distance between the point of evaluation $\mathbf{r}$ and nucleus A. The first summation term, $\sum_A \frac{Z_A}{|\mathbf{R}_A - \mathbf{r}|}$, represents the attractive potential due to all positive nuclei, whereas the second term, $\int \frac{\rho(\mathbf{r}')}{|\mathbf{r}' - \mathbf{r}|} d\mathbf{r}'$, corresponds to the repulsive potential generated by the negative electron density distribution.

The resulting potential $V(\mathbf{r})$ is a scalar field that varies in space and indicates regions of positive or negative electrostatic potential. Positive regions (often colored in blue on MEP

maps) correspond to electron-deficient, electrophilic areas, while negative regions (commonly in red) correspond to electron-rich, nucleophilic zones. This information is fundamental to understanding the preferential binding sites and the nature of ligand–receptor interactions.

The electrostatic potential is a three-dimensional property that can be evaluated at any point in space around the molecular system. Naturally, the MEP is calculated on a surface surrounding the molecule to better represent its characteristics. In specific aromatic systems, the validity of this approach can be verified by correlating the obtained MEP values with other theoretical or experimental quantities that depend on variable local charges. [64] For example, experimental substituent constants are related to local characteristics at different positions of the aromatic ring. Satisfactory correlations between local reactivity and MEP indicate that local variations in charge contribute significantly to changes in the electrostatic potential, which can be considered before performing molecular docking.

From a quantum mechanical perspective, the electrostatic potential is a well-defined quantity [65] and can be evaluated experimentally, for example, through X-ray diffraction studies [66]. One of the benefits of using MEP is the ability to identify regional features, or sites, in molecular space by evaluating the potential values at specific points. Several studies have shown that MEP is useful for estimating reactivity at particular sites in a molecule, both for chemical reactions and for intermolecular interactions, such as hydrogen bonds. However, the relationship between MEP values and local charges must be interpreted qualitatively, especially when the distance between the substituent group and the reaction center is significant.

3.5 Classical Molecular Dynamics

Molecular dynamics (MD) simulation is a powerful computational approach widely used to investigate complex biological systems, such as macromolecules [67]. Over time, MD simulations have proven valuable at various stages of scientific research, offering strategic support for the planning and interpretation of simulation-assisted experiments [68].

This methodology is grounded in the principles of classical mechanics, allowing the description of atomic motion over time within a defined molecular system [69]. According to the foundations of molecular mechanics (MM) [70], atomic interactions are described using Newtonian forces. These interactions are represented by empirical functions grouped into a set called a *force field* [71], which defines the total potential energy of the system, denoted by $V(r)$. This function is derived from the three-dimensional structure of the system and includes several terms that represent the energetic contributions of bonded and non-bonded interactions, such as bond stretching, angle bending, torsional rotation, electrostatic forces, and van der Waals interactions.

The general expression for the force field is given by:

$$V(r) = \sum V_{\text{bond}} + \sum V_{\text{angle}} + \sum V_{\text{dihedral}} + \sum V_{\text{vdW}} + \sum V_{\text{elec}}, \tag{3.7}$$

In this context:

- V_{bond} represents the energy due to bond stretching;
- V_{angle} corresponds to angular deformations between bonded atoms;
- V_{dihedral} is the energy associated with torsional (dihedral) rotations;
- V_{vdW} accounts for van der Waals interactions;
- V_{elec} refers to electrostatic interactions.

The harmonic contributions that describe variations in bond lengths and bond angles, according to Hooke's law, are given by:

$$V_{\text{bond}} = k_b(l - l_0)^2, \tag{3.8}$$

$$V_{\text{angle}} = k_\theta(\theta - \theta_0)^2, \tag{3.9}$$

where l and θ are the bond length and bond angle, l_0 and θ_0 are their equilibrium values, and k_b, k_θ are the corresponding force constants.

The torsional (dihedral) energy, which represents the rotational motion around a bond between four consecutively bonded atoms, is described by:

$$V_{\text{dihedral}} = \frac{V_n}{2}\left[1 + \cos(n\phi - \gamma)\right], \tag{3.10}$$

where V_n is the torsional energy barrier, n is the periodicity, ϕ is the dihedral angle, and γ is the phase shift [71].

Non-bonded interactions are typically modeled using van der Waals and Coulomb potentials. The van der Waals interaction is commonly represented by the Lennard-Jones potential:

$$V_{\text{vdW}} = 4\varepsilon_{ij}\left[\left(\frac{\sigma_{ij}}{r_{ij}}\right)^{12} - \left(\frac{\sigma_{ij}}{r_{ij}}\right)^{6}\right], \tag{3.11}$$

while the electrostatic interaction is modeled by Coulomb's law:

$$V_{\text{elec}} = \frac{q_i q_j}{4\pi\varepsilon_0\varepsilon_r r_{ij}}, \tag{3.12}$$

where ε_{ij} is the depth of the potential well, σ_{ij} the distance at which the potential is zero, r_{ij} the interatomic distance between atoms i and j, q_i and q_j the atomic charges, ε_0 the vacuum permittivity, and ε_r the dielectric constant of the medium.

Several force fields have been developed using different parameterizations. Some include additional terms to describe specific interactions such as hydrogen bonding, improper torsions, or adjustments to vibrational spectra [72].

MD simulation enables monitoring the evolution of atomic positions and interactions over time through the integration of Newton's equations of motion:

MD simulation enables monitoring the evolution of atomic positions and interactions over time through the integration of Newton's equations of motion:

$$\mathbf{F}_i(t) = m_i \mathbf{a}_i = -\nabla_{\mathbf{r}_i} V(\mathbf{r}), \tag{3.13}$$

where $\mathbf{F}_i$ is the total force acting on atom i, m_i is its mass, $\mathbf{a}_i$ is the acceleration, and $V(\mathbf{r})$ is the total potential energy of the system as a function of the atomic positions $\mathbf{r}$. The operator $\nabla_{\mathbf{r}_i}$ (nabla) denotes the gradient with respect to the position vector of atom i, and it yields a vector pointing in the direction of the greatest rate of increase of the potential energy.

By taking the negative of the gradient, the force is directed toward regions of lower potential energy, consistent with the physical tendency of systems to move toward equilibrium. These computed forces are then used to determine atomic trajectories through numerical integration of the equations of motion.

One of the most widely used algorithms for this integration is the Verlet algorithm, which estimates future positions based on current and previous ones, without the need to explicitly compute velocities:

$$\mathbf{r}(t + \Delta t) = 2\mathbf{r}(t) - \mathbf{r}(t - \Delta t) + \mathbf{a}(t)\Delta t^2, \tag{3.14}$$

This equation is derived from the forward and backward Taylor series expansions:

$$\mathbf{r}(t + \Delta t) = \mathbf{r}(t) + \mathbf{v}(t)\Delta t + \frac{1}{2}\mathbf{a}(t)\Delta t^2 + \cdots, \tag{3.15}$$

$$\mathbf{r}(t - \Delta t) = \mathbf{r}(t) - \mathbf{v}(t)\Delta t + \frac{1}{2}\mathbf{a}(t)\Delta t^2 + \cdots. \tag{3.16}$$

Before initiating an MD simulation, energy minimization is essential to eliminate steric clashes and reduce potential energy. Common methods include gradient descent [73], conjugate gradient [74], and Newton-Raphson [75], each employing different strategies based on the derivatives of the energy function to locate local minima.

Following minimization, the system is typically gradually heated to the desired temperature T_0, assigning atomic velocities according to the Maxwell-Boltzmann distribution.

During simulation, structural stability is frequently assessed using the root-mean-square deviation (RMSD) [76, 77], which evaluates the variation in atomic positions over time:

$$RMSD = \left[\frac{1}{N} \sum_{i=1}^{N} \left(\mathbf{r}_i(t) - \mathbf{r}_i(0) \right)^2 \right]^{1/2}, \tag{3.17}$$

where N is the number of atoms considered (typically Cα or backbone atoms), $\mathbf{r}_i(t)$ is the position of atom i at time t, and $\mathbf{r}_i(0)$ its initial position. Small RMSD values suggest structural stability, while larger deviations may indicate significant conformational changes. RMSD is particularly useful in analyzing similarities between molecular conformations, such as protein-ligand complexes.

3.6 Neural Networks

Artificial Neural Networks (ANNs) are computational models inspired by the functioning of biological neurons, composed of layers of interconnected units called artificial neurons. Each neuron performs a weighted summation of the inputs, followed by the application of a nonlinear activation function. These models are capable of capturing complex patterns and approximating functions in classification, regression, and prediction problems [78].

Mathematically, the operation of a single neuron can be expressed as:

$$y = f\left(\sum_{i=1}^{n} w_i x_i + b \right) \tag{3.18}$$

where w_i represents the weight associated with each input x_i, and b is the bias term.

In matrix-vector notation, for an entire layer of neurons, the transformation can be written as:

$$\mathbf{y} = f(\mathbf{W}\mathbf{x} + \mathbf{b}) \tag{3.19}$$

where:

- $\mathbf{x} \in \mathbb{R}^n$ is the input vector (molecular descriptors or spatial features);
- $\mathbf{W} \in \mathbb{R}^{m \times n}$ is the weight matrix, with m neurons in the layer;
- $\mathbf{b} \in \mathbb{R}^m$ is the bias vector;
- $f(\cdot)$ is the nonlinear activation function (e.g., ReLU, sigmoid, or hyperbolic tangent);

- $\mathbf{y} \in \mathbb{R}^m$ is the output vector produced by the layer.

During training, the parameters $\mathbf{W}$ and $\mathbf{b}$ are iteratively adjusted using optimization algorithms such as gradient descent, with the goal of minimizing a cost function [79].

In the context of molecular docking, neural networks are used to learn patterns inherent in protein–ligand interactions, correlating molecular structures with affinity scores. In **GNINA 1.3**, these networks enhance the pose refinement and affinity prediction processes, complementing traditional energy-based scoring functions [80].

3.6.1 Convolutional Neural Network

Convolutional neural networks (CNN) are a specialized class of networks designed to process data with spatial structure, such as images, 3D maps, or volumetric representations of molecular systems. Unlike densely connected networks, CNNs utilize *convolutional layers*, which apply filters (or kernels) that traverse the data to extract local and hierarchical features. [81]

The convolution operation is mathematically described by:

$$S(i,j) = (X * K)(i,j) = \sum_m \sum_n X(i-m, j-n) \cdot K(m,n) \tag{3.20}$$

where:

- X is the input matrix (or volume);
- K is the convolutional filter;
- $S(i,j)$ represents the output (feature map) after convolution at points (i,j).

In the case of three-dimensional data, such as molecular structures, convolution extends to volumes, allowing the capture of complex spatial relationships.

In GNINA 1.3, CNNs are fundamental to the scoring process, where protein-ligand complexes are represented as a three-dimensional (voxelized) grid. Each voxel stores information about atom types, charges, and physicochemical properties. CNNs process this representation to identify structural patterns correlated with binding affinities, providing a more robust and accurate assessment of the poses generated during docking [82].

The main advantage of CNNs in this context is their ability to exploit spatial and contextual information that traditional heuristic-based methods cannot fully capture, making them an extremely powerful tool in artificial intelligence-assisted molecular modeling [78].

3.7 Chapter Summary

This chapter presents the main computational modeling approaches used in the study of interactions between drugs and Marburg virus proteins. Density Functional Theory (DFT) was applied for structural optimization and electronic analysis of the ligands. Molecular docking allowed the prediction of binding modes and affinities, while the Molecular Electrostatic Potential (MEP) helped identify reactive regions. Classical Molecular Dynamics (MD) allowed the simulation of the temporal evolution of the complexes, complemented by analyses such as RMSD. Finally, Convolutional Neural Networks (CNNs) were employed to refine and evaluate molecular interactions, integrating artificial intelligence into the virtual screening process.

4 METHODOLOGY

4.1 Initial Considerations

This chapter describes in detail the methodological steps adopted to investigate the molecular interactions between the selected therapeutic candidates and MARV proteins, using computational molecular modeling techniques. The selection of tools and strategies described here is based on established practices in structural bioinformatics and molecular simulation, with an emphasis on model accuracy and reproducibility.

Initially, molecular electrostatic potential were constructed to analyze the molecular charge distribution, enabling the understanding of regions of reactivity and electronic affinity. Subsequently, the molecular docking technique was applied using the software AutoDock Vina (based on classical physics) and Gnina (employing deep learning), allowing the evaluation of the interaction energy between ligands and viral receptors, as well as the identification of the most favorable conformations. Finally, molecular dynamics (MD) simulations were performed to investigate the temporal stability of the formed complexes in an aqueous environment using the GROMACS package.

All tools were selected based on their scientific relevance, computational performance, and ability to provide realistic representations of the molecular systems investigated, integrating classical and modern simulation methods with artificial intelligence-based approaches.

4.2 Molecular Electrostatic potential Technique

Electrostatic potential distribution maps enable the visualization of the organization of electric charge within molecules, as well as their charge-related properties [83]. Furthermore, they allow observation of molecular measurements and shape. In the field of organic chemistry, these maps are valuable tools for estimating the behavior of complex molecules [84].

Generating an electrostatic potential distribution map begins with the acquisition of a specific data set: the electric field potential energy [85]. To achieve this, Gaussian 16 [86] was used to measure the energy contained at a given position relative to the atomic nuclei present in the molecule. The electrostatic field energy determines the intensity of the interactions between charges, nuclei, and electrons at a given point.

To accurately determine the molecular charge distribution, it is necessary to calculate a wide range of electrostatic potential energy levels. The most effective way to represent these data is through visualization, as illustrated in Figure 5, which depicts the electrostatic potential. These values are derived from the molecular electron distribution model, based on the Schrödinger

equation. To aid interpretation, a color scale is employed: red regions correspond to the lowest electrostatic potential energy, while blue regions indicate the highest values [87].

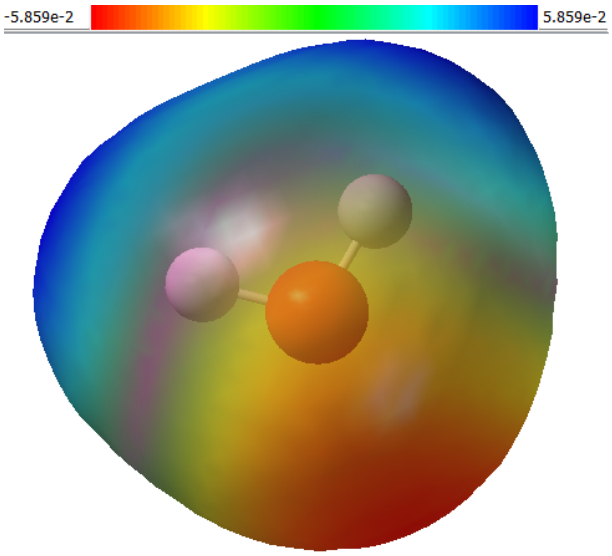

Figure 5 – Example of the Electrostatic Potential Map of Water Molecule

Source: Author.

Representations of the molecular electrostatic potential also reveal detailed information about the molecule's charge allocation [85]. This behavior results from the combined action of nuclear properties and electrostatic potential energy [88]. Broadly speaking, regions with high electrostatic potential indicate a lower electron density, while low potential regions reveal a higher electron concentration. This aspect of electrostatic potential distributions can be extended to understanding molecular processes in different contexts.

4.3 Molecular Docking

DOC is a tool for anticipating how a molecule will behave when interacting with another. To analyze the relationships between the therapeutic agents studied and the previously highlighted MARV conformations, we adopted the Autodock Vina 4.2 (ADV) and Gnina 1.3 (GNINA) computational resources. The ADV and GNINA evaluation algorithms cover all atoms of the ligands and proteins. The features used to conduct the DOC are shown below, ranging from ligand and receptor pretreatment to the docking procedure between them, performed on the ADV and GNINA platforms.

4.3.1 AutoDock Vina

AutoDock Vina (ADV) is one of the most widely used tools for molecular docking due to its efficiency, speed, and reliability in predicting ligand-receptor affinity. Developed by

Oleg Trott and Arthur J. Olson [89], ADV is based on a stochastic optimization algorithm that combines global and local searches to find the best orientation for a ligand within the protein's active site. The program uses an empirical energy function that estimates binding affinity based on van der Waals relationships, hydrogen bonds, and electrostatic interactions.

The approach adopted by ADV considers the ligand as flexible, allowing its torsion angles to be freely explored, while the receptor remains rigid during the simulation. This simplification reduces computational cost while maintaining satisfactory results for large-scale virtual screenings. System preparation involves adding polar hydrogens, assigning Kollman charges to receptors and Gasteiger charges to ligands, and defining a grid box centered on the active site. ADV is widely used in drug discovery protocols, capable of generating multiple docking poses, considered according to the calculated affinity energy. Due to its robustness and compatibility with auxiliary tools, such as AutoDock Tools, Vina remains a strategic choice in molecular interaction studies.

4.3.2 Architecture and Functioning of GNINA 1.3

Gnina 1.3 represents an evolution of traditional molecular docking methods by integrating deep learning, specifically through Convolutional Neural Networks (CNNs), into the ligand–receptor binding affinity evaluation process. Developed by McNutt *et al.* (2021) [25], *Gnina* builds upon the *AutoDock Vina* framework but incorporates CNN models trained on large experimental datasets, capable of capturing complex and non-linear molecular interaction patterns that escape traditional empirical scoring functions.

During the docking process with *Gnina*, the system setup resembles that of *Vina*, with the definition of the search box and the use of rigid receptor structures. However, during the scoring stage, the neural model — `general_default2018_4` — processes three-dimensional maps of ligand–receptor complexes, computing scores based on spatial and physicochemical features. The CNN model acts as an alternative scoring function, analyzing interaction potentials with greater precision. This approach enhances the ability to distinguish between correct and incorrect poses, resulting in more reliable predictions of intermolecular interactions [25].

The application of *Gnina* is particularly valuable in studies where pose classification accuracy is critical, such as in refined virtual screenings or post-docking refinement processes. The software's flexibility in generating multiple conformations and its predictive power make *Gnina* a state-of-the-art tool that combines molecular physics with artificial intelligence.

4.3.2.1 Neural Network Architecture

One of the standard CNN architectures used in *Gnina*, named `general_default`, is a three-dimensional convolutional neural network (3D-CNN) trained on thousands of protein–ligand complexes from the *PDBbind* database [90]. Its goal is to learn spatial patterns of

molecular interactions — such as hydrogen bonds, hydrophobic contacts, and electrostatic forces — through volumetric representations of molecules.

1. **Input layer:** the model receives a cubic grid (typically 30×30×30 Å) divided into voxels. Each voxel encodes atomic densities for different atom types (C, N, O, S, H, etc.) from both the ligand and the receptor.
2. **Convolutional layers:** several three-dimensional filters extract local interaction features. The initial layers detect simple atomic arrangements, while the deeper layers capture complex and non-linear spatial patterns related to binding affinity.
3. **Pooling layers:** reduce spatial resolution, highlighting the most informative regions and improving computational efficiency.
4. **Fully connected layers:** combine the extracted features into a global molecular representation that integrates geometric and energetic properties.
5. **Output layer:** the CNN produces two main outputs:
   - *Pose score*: evaluates the geometric plausibility of the predicted ligand pose.
   - *Affinity score*: estimates the binding free energy (ΔG) in kcal/mol.

4.3.2.2 Training and Integration with the Docking Process

The `general_default2018_4` model was trained using the *PDBbind 2018* dataset, which contains thousands of protein–ligand complexes with experimentally known binding affinities. The loss function combines the mean squared error (MSE) for affinity prediction with a binary classification term for pose correctness. This hybrid training strategy allows the network to learn both to quantitatively estimate binding energy and to qualitatively distinguish physically realistic binding poses [80, 91].

During the docking process, *Gnina* initially generates multiple poses using the search algorithm inherited from *Vina*. These poses are then re-evaluated by the CNN, which reorders them based on its learned spatial and physicochemical understanding of molecular interactions. This process results in higher accuracy and consistency in predicting binding conformations [80, 91].

In summary, *Gnina* 1.3, with its CNN model `general_default2018_4`, represents a significant advance in molecular docking by combining classical molecular mechanics principles with three-dimensional deep learning techniques, allowing for more accurate modeling of drug-protein interactions as shown in Figure 6 [80, 91].

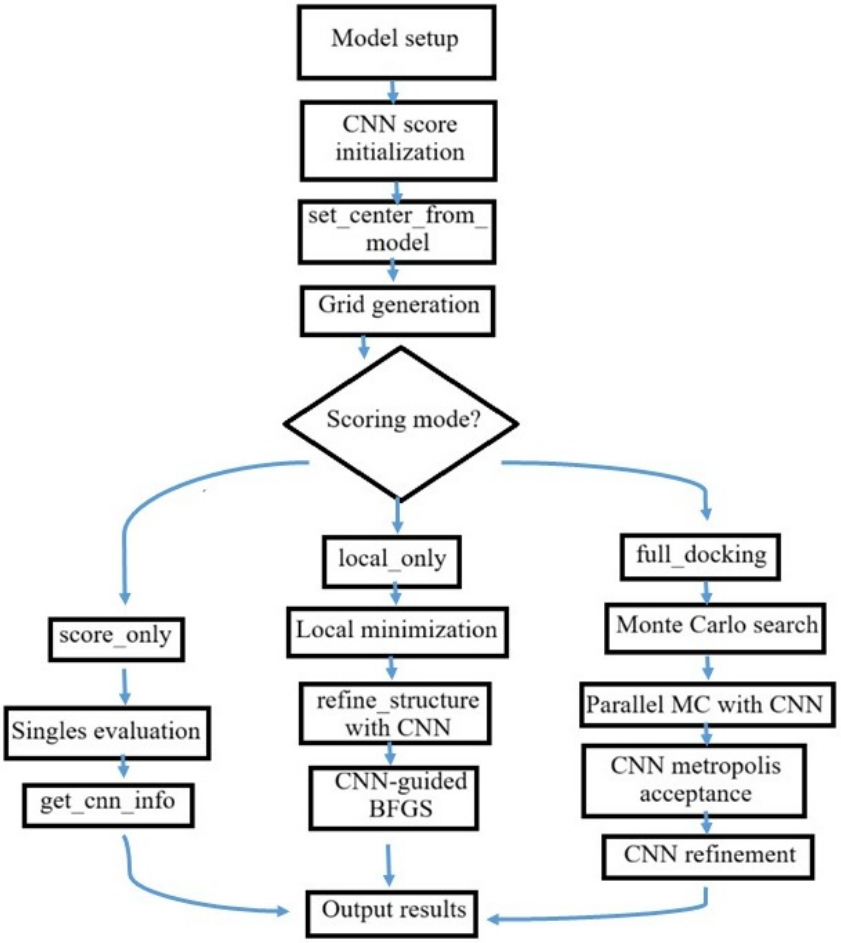

Figure 6 – CNN Scoring Workflow.

Source: adapted from the GNINA guide [80, 91]

4.4 Receptor and Ligand Preparation Steps

All simulated experiments were performed in accordance with the receptor-ligand interaction model [92], in which six structures from Protein Data Bank [35] were selected as receptors, and molecules belonging to three drugs were selected as ligands, all of which are potential candidates for the treatment of MARV. The receptor structures were optimized using the CHARMM-GUI (CHM) platform [93] to establish optimal conditions that correspond to the various previously defined targets.

We applied the CHM in the form of a multifunctional scalar function, aiming to improve several targets, for which evaluation constitutes the restrictive element, having its performance been clearly defined through the use of varied optimization algorithms. For this purpose, we made use of the AMBERFF14SB force field model [94], with the intention of identifying the most favorable conformation based on the total system, in which we also determined its restricted potential electrostatic charges (RESP) [95]. The polarizable continuum model (PCM) was also adopted at this stage [96]. The ligands were selected by informing their identifiers in

the PubChem [97] repository during the upload of the four ligands, after being improved with the aid of the Gaussian16 (G16) software employing DFT [98] with the B3LYP (Hybrid DFT functional that combines Hartree-Fock exchange with Becke (B88) and Lee-Yang-Parr (LYP) corrections to accurately calculate molecular energies and properties) and 6-31 + (d, p) (Set of basis functions used to describe atomic orbitals in quantum calculations) functionals [99]. The entire process followed the same characteristics shown in Figure 7.

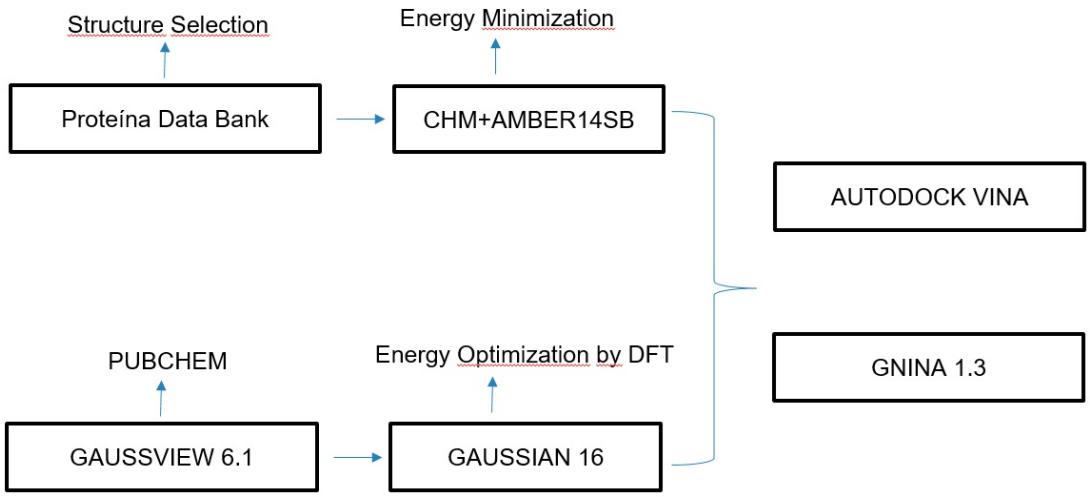

Figure 7 – Docking Process Flowchart.

Source: Author.

Furthermore, for each of the three selected ligands, 20 spatial arrangements were generated across the macrostructures using the stochastic optimization strategy of ADV [100] combined with the neural networks in GNINA [80]. From these, the lowest-energy structure of each ligand was selected, following the criteria of Guedes et al. (2014) [101], and adopted as the configuration for subsequent investigation. At this stage, ligands were modeled as flexible structures, while receptors were kept rigid. The affinity energy (also referred to as binding affinity) of the protein–ligand interactions was then evaluated by ADV and GNINA using their respective scoring functions.

4.5 Docking approach adopted for ADV and GNINA

After the ligand refinement and receptor energy adjustment steps, molecular docking was performed using the Autodock Vina (ADV) and Autodock Tools (ADT) software. The ligands had their torsion angles fully relaxed, and flexible docking was performed on the ligands, maintaining the receptors in rigid conformations throughout the procedure.

After the insertion of polar hydrogens into the receptors, partial charges were assigned to the connected atoms based on the Kollman model [102], for both the ligands and receptors. Charges were applied and polar hydrogens [103] were selected on the ligands and receptors,

taking into account typical and atypical hydrogen interactions. The grid box was parameterized based on the Lennard-Jones expression for interatomic interactions [104, 105] with electrostatic factors by assigning values to all receptor atoms. The grid box was configured for the simulations considering the following dimensions:

Table 1 – Grid box dimensions used for molecular docking simulations of MARV proteins in the x, y, and z directions (in Å).

Macromolecule	x **(Å)**	y **(Å)**	z **(Å)**
GP2	78	60	56
VP24	60	40	42
VP30	56	66	72
VP35	86	88	68
VP40	60	52	50
NP	100	76	54

Source: Author.

The empirical free energy function, combined with the Lamarckian genetic algorithm (LGA) [106], was used for molecular docking predictions, utilizing the most relevant variables.

For the docking step with Gnina, the `general_default2018_4` neural network model was used. First, the internal active region of the protein where docking occurs was defined (the same one used in ADV), delimiting the search box that specifies where the ligand will be positioned and explored. Then, the Convolutional Neural Network (CNN) model was activated using the `-scoring general_default2018_4` parameter, which allows the CNN to evaluate the interactions that may occur between the ligand-receptor complex. Gnina can generate different docking poses, that is, different ways for the ligand to fit into the protein's active cavity. The total number of orientations generated for the top 20 positions was adjusted.

Thus, the docking protocol in Gnina 1.3 represents a modern and robust approach to estimating intermolecular bonds, combining traditional methods with machine learning, aiming to deliver extremely reliable results.

Based on the evidence obtained through DOC, which yielded 20 conformations for each ligand-receptor interaction, Discovery Studio Visualizer 4.5 was used for visualization. Among these, for each molecular system, the conformation with the most favorable interaction energy value associated with chemically plausible bonds (i.e., with lengths consistent with standard chemical bond patterns) was chosen. Additionally, three-dimensional visualizations and PDBQT-format files were generated with the aid of the software [107].

4.6 Protocol for MD Simulations

During the MD work, the Root Mean Square Deviation (RMSD) was calculated, as described by Bel et al. (2019) [108] and Peele et al. (2020) [109]. This calculation is widely used in stability and conformational analyses of macromolecular systems during computer simulations. The RMSD enables us to assess structural fluctuations over time and, consequently, the system's equilibrium. Small positional changes indicate when the molecule remains close to its equilibrium conformation, while abrupt increases indicate significant conformational changes or instabilities in the molecular interaction.

MD evaluations were performed using the CHARMM36 interaction field (Huang, 2017; CHARMM36), which interacts with MARV virus macromolecules, according to the implementation of version 2024.2 of the GROMACS software package (Berendsen, 1995; GROMACS). The simulated tests were developed in an explicit aqueous medium, with a system box filled with aqueous TIP3 molecules (Gereben2011SPCE), and chloride and sodium ions were added to neutralize the total charge.

The initial models, obtained after the DOC step, were subjected to an energy reduction using the steepest gradient method. This step provided the starting configurations for the models, with an average of the presented systems of approximately 25,500 atoms.

Autonomously generated force field structures were used, tailored to the specific simulation requirements, each containing specific parameterizations for different types of dynamic processes. Some fields include terms inserted to describe interactions such as hydrogen bonds or interactions involving bond angles and distances, aiming for greater precision in the vibrational spectra of the molecules present (Stipe et al., 1998). Among the force functions most commonly used for modeling biological systems, the most notable are AMBER [110], CHARMM [111], and GROMOS [112].

The simulated tests were performed under constant NPT (The system has constant number of particles, pressure and temperature) and NVT (The system has a constant number of particles, volume and temperature) conditions, with a fixed number of molecules, temperature, and pressure, as described by Almeida 2022 *et al*, [113]. Ensuring the geometry of the aqueous molecules, the SETTLE calculation was also used [114], while the long-range electrostatic interaction relations were used using the Particle-Mesh Ewald (PME) method [115]. The pressure was maintained at 1 bar, and the system's temperature was set to 303 K, with a thermal coupling of 0.1 Fs, applied separately to water (TIP3P) and ions.

Each simulated test was performed for 100 ns, with the first nanosecond dedicated to establishing the system's dynamic equilibrium. The simulated movements and models were analyzed using GROMACS's native tools. The conjugate gradient algorithm was used to impose constraints on covalent bonds with hydrogen atoms.

For quantitative analysis, the CPPTRAJ application [116] was used to extract the RMSD

measurements and hydrogen bonds observed during the temporal simulation. Additionally, the TRJCONV module [117] was used to process the simulated trajectories and generate graphs that relate the RMSD to the simulation time interval.

4.7 Chapter Summary

This chapter systematically presented the methodological steps employed in the computational analysis of the interactions between ligands and proteins of the Marburg virus. The adopted strategy was based on an integrated workflow, encompassing calculations of electronic properties to atomistic-level dynamic simulations, thereby ensuring a multiscale assessment of the behavior of the investigated biomolecular systems.

Initially, the MEP distribution was calculated in order to identify regions of higher or lower electron density within the molecules. For this purpose, the Gaussian16 package was employed, with electronic structure calculations based on Density Functional Theory (DFT), using the B3LYP functional and the 6-31+G(d,p) basis set. Visualization of the electrostatic potential maps was performed using the GaussView software, enabling the graphical interpretation of regions prone to attractive or repulsive interactions.

In the subsequent step, molecular docking was carried out to predict the binding modes between the selected ligands and the target proteins of the Marburg virus. This task was performed using AutoDock Vina and Gnina. AutoDock Vina enabled the generation of multiple candidate protein–ligand conformations, based on a stochastic search algorithm combined with an empirical scoring function. In parallel, Gnina was employed to refine the results through CNNs, which provided a more robust evaluation of binding affinity and structural complementarity, overcoming inherent limitations of traditional scoring functions. The process considered different interaction modes, prioritizing conformations with the most favorable binding energies and chemically plausible interactions.

Subsequently, the selected conformations were subjected to classical molecular dynamics (MD) simulations in order to validate the conformational stability of the protein–ligand complexes over time. These simulations were conducted using the GROMACS package, with biomolecular force fields widely adopted in the literature. Parameters such as the RMSD and the number of hydrogen bonds were monitored as direct indicators of the stability and persistence of intermolecular interactions.

Therefore, the applied methodology integrated state-of-the-art computational tools, enabling a detailed analysis of ligand–protein interactions. The combination of electronic property calculations, molecular docking with artificial intelligence, and molecular dynamics simulations provided a comprehensive and multiscale perspective of the interactions, from surface properties to dynamic behavior at the atomic level. This set of techniques ensured greater reliability of the results and offered valuable insights into the therapeutic potential of the investigated compounds.

5 RESULTS AND DISCUSSION

5.1 Initial Considerations

This chapter presents the results of molecular docking simulations performed with the ADV and GNINA 1.3 programs. The main objective was to investigate the affinity between the antiviral ligands—Ivermectin, Lopinavir, Nafamostat, and Remdesivir—and the Marburg virus proteins (GP2, VP24, VP30, VP35, VP40, and NP). The analysis focused on the most energetically favorable interactions associated with the formation of stable complexes.

Docking estimates the affinity energy in kcal/mol, with more negative values indicating more stable binding. The GNINA simulations generally presented lower energies than the ADV simulations.

To complement this, electrostatic potential maps were used, which show the distribution of charges on the molecular surface, helping to identify regions important for hydrogen bonding and electrostatic interactions.

The stability of the complexes was assessed using RMSD, which measures the structural variation between conformations for the five outermost structures. Low RMSD values indicate that the complex structure remains stable over time, reinforcing the reliability of the binding modes found.

Furthermore, the binding modes were analyzed, considering hydrogen bonds, hydrophobic interactions, and other non-covalent forces, essential for understanding molecular recognition patterns and identifying key residues with therapeutic potential. The main findings of these simulations are discussed below, highlighting the compounds with the highest affinity for each viral protein.

5.2 DOC Results

5.2.1 Results obtained by ADV and GNINA

The observed interactions revealed very close bonds, characterized by attractive properties. These interactions can be directly related to the formation of more stable associations between macromolecular configurations, as they depend on variations in the electronegative tendency of the atoms. Furthermore, the position assumed involving the ligands located in the catalytic site favors bonds involving the existing amino acids, resulting in distinct associations depending on the specific location of each ligand.

The strength of local ligand–amino acid interactions is directly related to bond interacti-

ons: the lower the energy values, the more stable and stronger these interactions are. Consequently, the highest binding energy values obtained (presented in Table 2) in the simulations likely correspond to the conformations adopted by the ligands in the biological environment. In Figures 8- 31, we present images of the configurations that resulted in the most favorable binding energy values associated with the four ligands analyzed. Notably, these interactions occur around the catalytic region of the structures—for example, Figure 17 shows the interaction of Lopinavir with the VP40 protein—suggesting that the obtained evidence may be related to the effectiveness of a therapeutic approach against the MARV virus.

When analyzing the results generated by docking, it is common to use the minimum affinity energy level as a criterion to establish the ideal interaction between the ligand and the protein of interest [118]. However, in this study, we adopted the statistical average based on the Boltzmann distribution of the binding connections, providing a more realistic assessment, as lower-energy states occur more frequently within the system. We suggest that this approach is more appropriate than using a simple average of the binding scores or exclusively selecting the highest score obtained.

The data presented in Table 2 demonstrate that, in the absence of interference, Ivermectin presented greater interaction potential compared to the other compounds analyzed. The GNINA software was essential for this analysis, as it automatically finds potential binding sites (also known as cavities or active sites) through the support of its convolutional neural networks.

Regarding the crystal structures of the analyzed complexes, the program frequently identified different binding sites, considering those with the lowest affinity energy parameters were considered the most favorable. Throughout the simulations, it was possible to map the macrostructure sectors that favor non-covalent interactions involving the ligands, confirming that all of them have greater affinity for the active site of the receptors.

Table 2 – Scores from simulations performed with Gnina and AutoDock Vina (ADV).

Complex	Ligand	Gnina (kcal/mol)	ADV (kcal/mol)
GP2	Ivermectin	**-9.01**	-8.1
	Lopinavir	-7.37	-7.1
	Nafamostat	-7.16	-7.2
	Rendezvir	-6.56	-6.2
NP	Ivermectin	**-10.27**	-9.4
	Lopinavir	-9.22	-8.6
	Nafamostat	-8.59	-8.6
	Rendezvir	-7.92	-7.0
VP24	Ivermectin	**-8.74**	-8.3
	Lopinavir	-8.67	-7.6
	Nafamostat	-7.99	-8.0
	Rendezvir	-7.46	-7.5
VP30	Ivermectin	**-10.22**	-9.3
	Lopinavir	-8.05	-7.5
	Nafamostat	-8.01	-8.1
	Rendezvir	-7.11	-7.0
VP35	Ivermectin	**-8.74**	-8.1
	Lopinavir	-7.70	-7.0
	Nafamostat	-7.33	-6.9
	Rendezvir	-7.09	-6.7
VP40	Ivermectin	**-10.54**	-9.4
	Lopinavir	-10.46	-9.5
	Nafamostat	-10.00	-10.1
	Rendezvir	-9.59	-9.4

Source: Author.

The DOC analysis also highlighted the importance of the protein's malleability in association with the ligand, allowing for a better understanding of the observed interactions. Only the protein-ligand conformations with the best scores were analyzed in detail. The findings in Table 2 present the energy affinity measurements obtained for the ligands bound to the GP2, VP24, VP30, VP35, VP40, and NP proteins. These values reflect the preliminary information obtained by the fitting tool used, representing the relative energy affinity value of the interactions.

Considering the simulations conducted with antiviral drugs, Ivermectin presented the lowest energy affinity parameters, standing out among the other compounds in the predominance of interactions observed in the analyzed macrostructures. Next, Lopinavir, nafamostat, and Remdesivir stood out. Ivermectin obtained the lowest average energy affinity values, as determined by the simulations, suggesting that its structure anchors more stably to the target proteins than those of other potential pharmaceutical compounds.

The DOC presented by Gnina 1.3 demonstrated the most promising results regarding energetic affinity for most of the complexes analyzed. Therefore, based on these data, Gnina 1.3 can be evaluated as the more effective approach of the two for this type of analysis.

Figures 8- 13 illustrate the interactions between molecules involving Ivermectin, specifically with amino acids. The molecular connection between Ivermectin and GP2, as illustrated in Figure 8, shows a set of five interactions. Ivermectin interacts strongly with GP2 through hydrogen bonds (mainly with Asn619 and Arg581), indicating good chemical affinity. Furthermore, hydrophobic interactions also contribute to the consistency of the complex. Figure 9 characterizes the interactions with VP35, resulting in a total of seven bonds. The predominant interactions occur through hydrogen bonds, such as between Asn225 and the ligand, 2.38 Å, and between Lys211 and the ligand, 2.55 Å and 2.65 Å, where the ligand accepts oxygen and the protein donates hydrogen. Furthermore, hydrophobic interactions are present, as seen with Lys211, Lys237, and Lys241, which contribute to the system's stability. A Pi-Alkyl interaction also occurs between Tyr240 and the ligand, which is important for the hydrophobic interaction. These interactions indicate a strong affinity between the ligand and the protein structure.

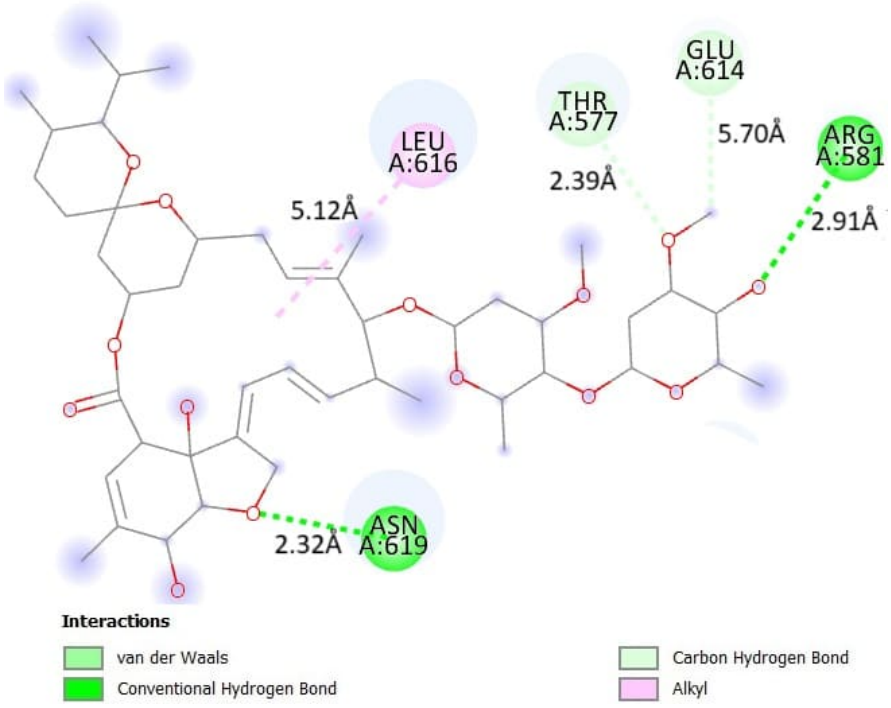

Figure 8 – Interactions of Ivermectin with GP2 protein (PDB ID: 4G2K).

Source: Author.

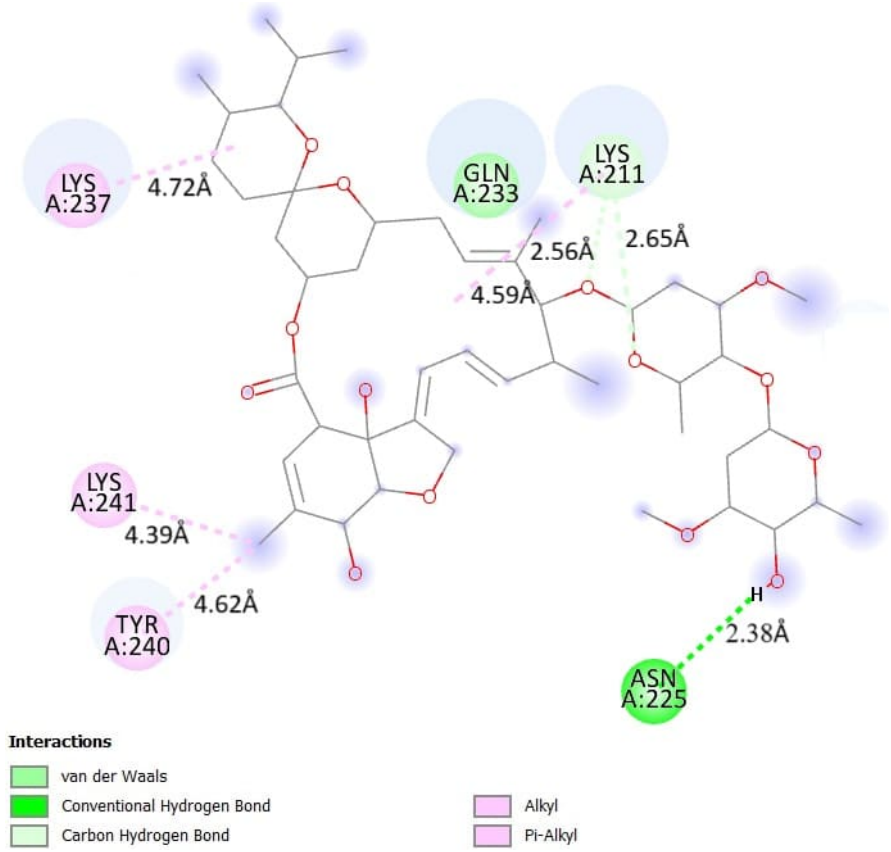

Figure 9 – Ivermectin interactions with VP35 protein (PDB ID: 4GH9).

Source: Author.

The central portion of the ligand molecule, as previously observed, showed that intramolecular bonds resulted in more favorable energies, especially when simulating with VP40 (Figure 10), which exhibited interactions based on hydrogen bonds. This is because these are relatively strong interactions, typical of hydrogen atoms bonded to electronegative atoms (such as oxygen and nitrogen) and which have lone electron pairs. This class of chemical interactions occurs frequently in biological environments, especially between amino acids and ligands, in which nitrogen and oxygen atoms (such as those in Gln143, Gly87, and others) are involved in the formation of these bonds. During the DOC process, both water molecules and co-crystallized ligands were excluded, and the ligand energy was minimized using the B3LYP/6-31G level of theory, thereby preparing it for the docking process. Among the docked conformational arrangements of the analyzed substance, the one closest to the orientation of the co-crystallized ligand, with a good score, was selected for evaluation of molecular interactions in Discovery Studio Visualizer 4.5.

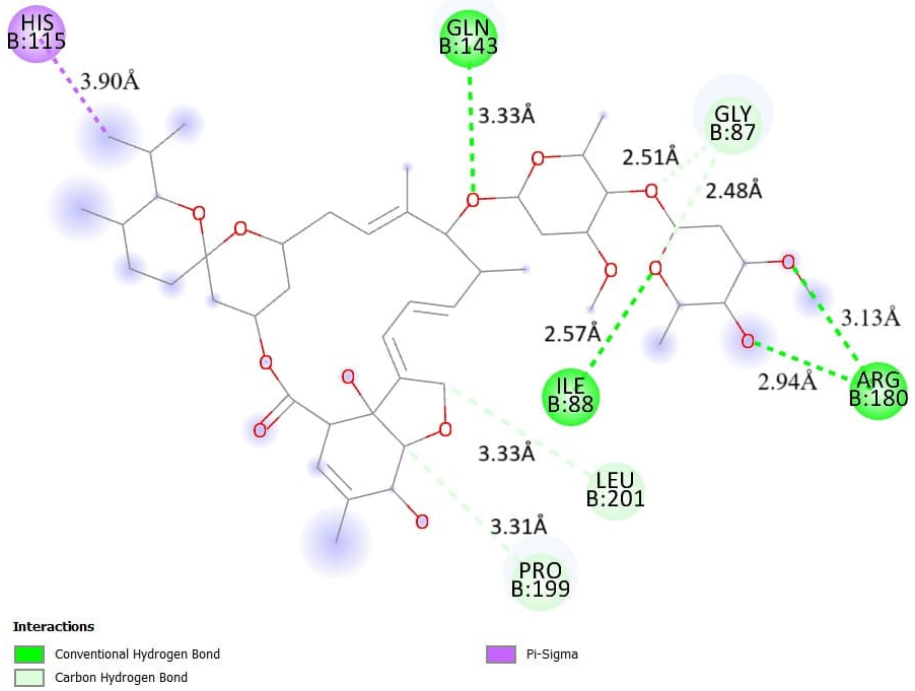

Figure 10 – Ivermectin interactions with VP40 protein (PDB ID: 5B0V).

Source: Author.

The drug created hydrogen bonds with GP2, VP30 (Figure 13), VP35, VP24 (Figure 12), VP35, VP40, and NP. The existence of this interaction form is essential in molecular arrangement and ligand associations, such as protein pairing and molecular detection. The hydrogen bonding investigation corresponds to the docking evaluation; high affinity was detected in the interaction, which may suggest a level of control of this class of interactions in the context of affinity energy. In the active region of NP (Figure 11), conventional hydrogen bonds predominate. Examples include the binding between Lys21:HZ1 and ligand:O, 2.59 Å, Lys21:HZ2 and ligand:O, 2.36 Å, and Arg187:NH1 and ligand:O, 3.14 Å. Complementarily, hydrophobic interactions occur, such as Pi-Sigma between ligand:C and Phe190 (3.48 Å) and Alkyl-Alkyl between Lys21 and the ligand, 4.90 Å. Hydrogen bonds play a crucial role in stabilizing the complex, while hydrophobic interactions contribute to additional stability, but to a lesser extent. Based on Ivermectin's DOC scores, studies on these interactions and their contemporary applications for the potential treatment of MARV are needed.

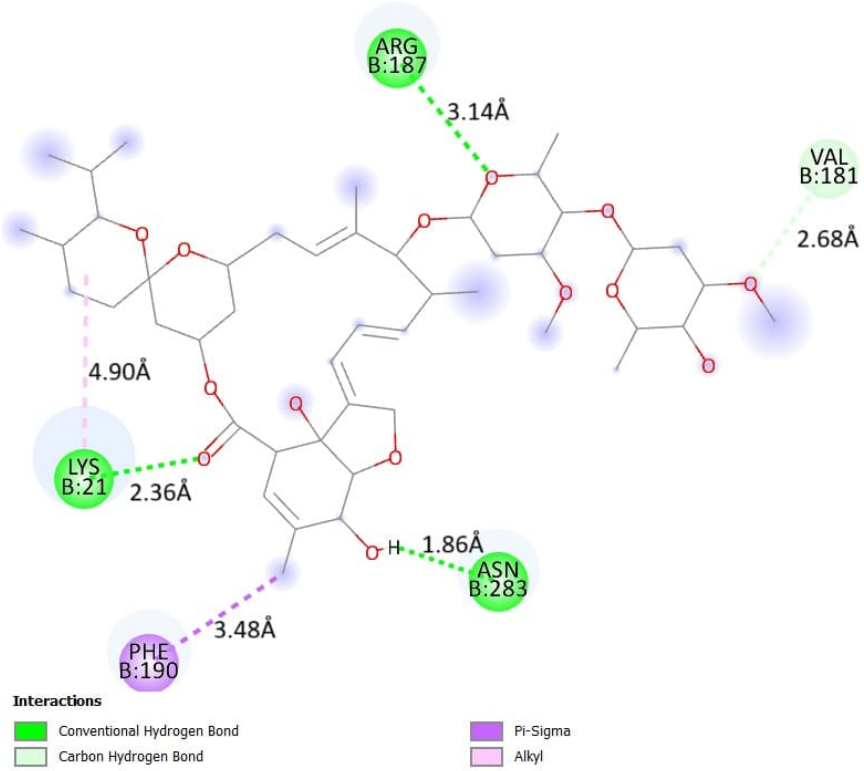

Figure 11 – Ivermectin interactions with NP protein (PDB ID: 5F5M).

Source: Author.

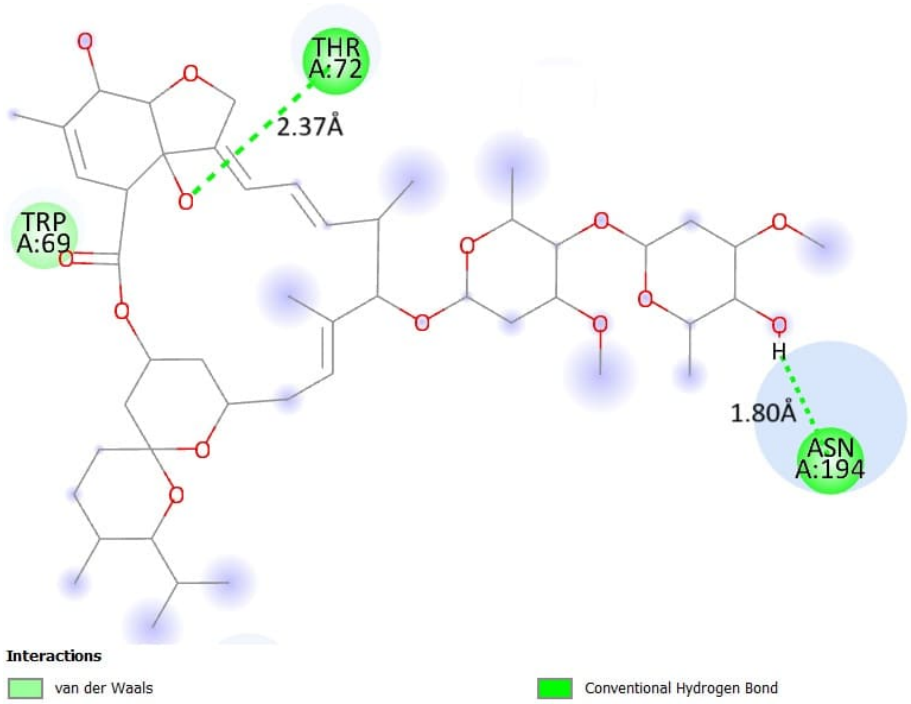

Figure 12 – Ivermectin interactions with VP24 protein (PDB ID: 4OR8).

Source: Author.

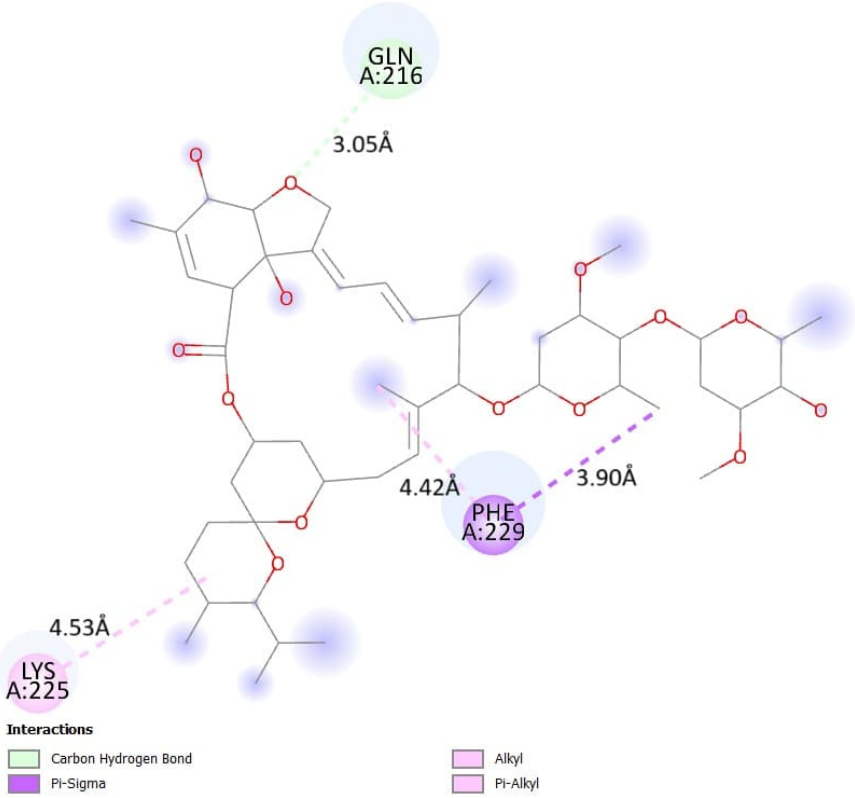

Figure 13 – Ivermectin interactions with VP30 protein (PDB ID: 5T3W).

Source: Author.

To evaluate the binding energy and the affinity of inhibitors for the enzyme's active site, the binding site was extracted and analyzed. The results (Table 2) indicate that, although some inhibitors exhibit lower affinity and binding energies, they still show measurable interaction with the enzymatic active site, justifying their inclusion in comparative studies. Ivermectin displayed the strongest energetic affinity among the tested inhibitors, reaffirming its potential as an effective inhibitor.

As illustrated in Figures 14 to 19, the conformations obtained by Lopinavir are presented. In the GP2 catalytic site (Figure 14), bonds occurred only with amino acids. First, a conventional hydrogen bonding interaction exists between the Lopinavir hydrogen atom and the GP2 oxygen atom, with a distance of 2.49 Å. This interaction demonstrates a strong and stable bond between two parts of the ligand, which contributes to its structural stability. Furthermore, Lopinavir forms a hydrogen bond with the amino acid Gln623:OE1 (distance of 3.65 Å). In this case, the interaction occurs through a carbon-hydrogen bond, where the ligand carbon atom donates hydrogen to the oxygen of Gln623.

Another interaction is the hydrophobic π-π stacked interaction between two parts of the ligand itself, with a distance of 5.23 Å. This interaction involves Pi orbitals and highlights an intramolecular affinity of Lopinavir that is not directly associated with any specific amino acid. Lopinavir also interacts hydrophobically with several amino acids, such as Leu570, Ile620, and

Leu573, forming π-Alkyl interactions. These interactions involve the correlation between the ligand's π orbitals and the amino acid's alkyl groups. The distances of these interactions range from 4.15 Å to 5.14 Å, with some interactions repeated, as seen in the case of ILE620, which appears in two distinct interactions.

Finally, Lopinavir forms a π-Alkyl interaction with the amino acid Arg581 (distance of 5.37 Å), which reinforces the predominant presence of hydrophobic interactions between the ligand and hydrophobic amino acid residues, such as Leu570, Ile620, and Leu573.

The noncovalent interaction involving the surface of a π-system with high electron density exhibits significant binding energy, reaching values in solution comparable to those of conventional bonds. Analogous to other noncovalent interactions, hydrophobic bonds, such as those observed in Pi-Alkyl and Pi-Pi Stacked interactions, are crucial in determining protein conformation, molecular affinity, and the catalytic function of enzymes. The interaction between Lopinavir and the GP2 domain of the receptor provides evidence of an attractive interaction between the electrophilic region, as evidenced by the hydrophobic interactions between the ligand and amino acid residues such as Leu570, Ile620, Arg581, and Leu573.

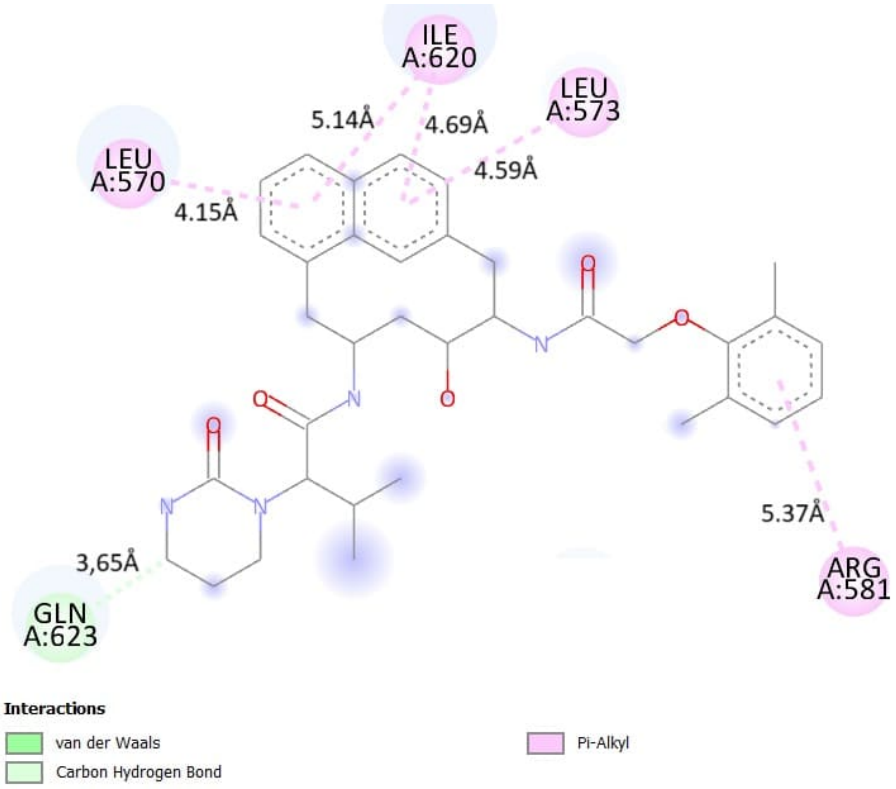

Figure 14 – Lopinavir interactions with GP2 protein (PDB ID: 4G2K).

Source: Author.

In Figure 15, Lopinavir and VP35 revealed the presence of several hydrogen bonds, both electrostatic and hydrophobic, which together aid in the fixation of the formed complex. Among the hydrogen interactions, a conventional bond stands out between the hydrogen of the

ligand (Lopinavir) and the OE1 atom of residue Gln233, at a distance of 2.31 Å. This interaction is considered strong and stable, playing a decisive role in anchoring the ligand in the active region of the protein. Furthermore, two C–H···O hydrogen bonds were observed. The first occurs between the HA hydrogen of residue Lys211 and the oxygen of Lopinavir, at a distance of 2.71 Å. The second involves a carbon atom of Lopinavir itself acting as a donor, and again, the OE1 atom of Gln233 serves as an acceptor, at a distance of 3.72 Å. Although these bonds are weaker than conventional hydrogen bonds, they still contribute to the overall interaction of the system.

Regarding electrostatic interactions, a π-cation interaction was identified between the positively charged HZ1 group of residue Lys237 and the electron cloud of the π orbitals of Lopinavir. This interaction, with a distance of 3.25 Å, is particularly relevant because it involves an attractive force between opposite charges, which favors the positioning and stability of the ligand within the protein's catalytic site.

Furthermore, the complex exhibits several hydrophobic interactions, predominantly of the π-alkyl and π-sigma types. The π-sigma interaction was observed between the methyl group of residue Ile284 (CG2 atom) and the π orbitals of Lopinavir, at a distance of 3.50 Å. The π-alkyl interactions involve the electron cloud of Lopinavir interacting with alkyl side chains of various residues, such as Val234 (5.36 Å), Lys237 (4.10 Å), Pro282 (5.32 Å), and Pro293 (4.36 Å). These interactions significantly contribute to ligand binding, strengthening its affinity with the protein, especially in hydrophobic regions.

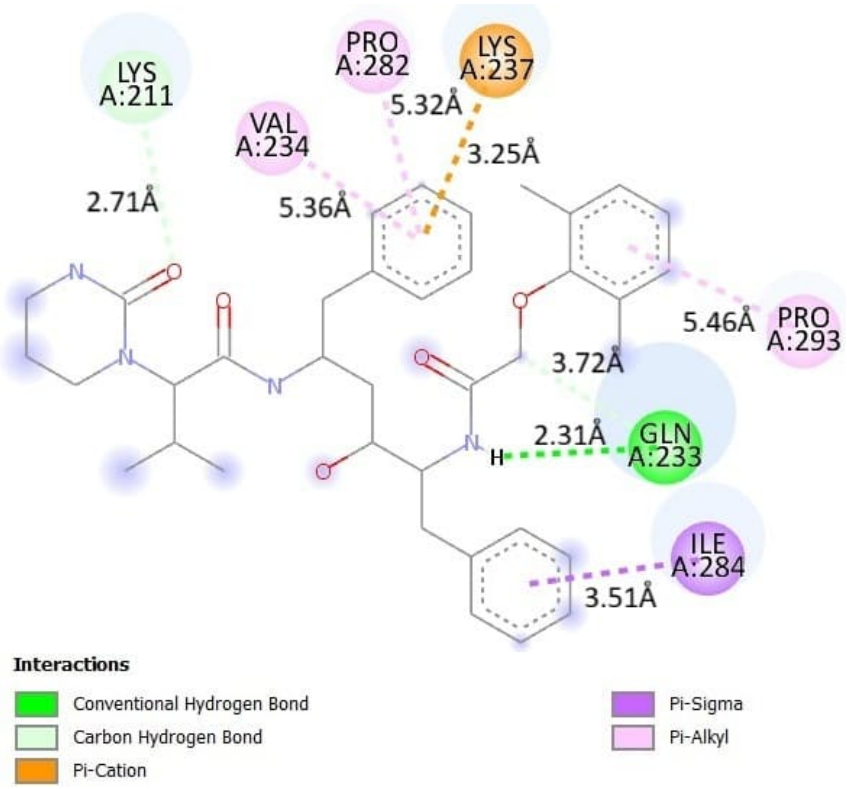

Figure 15 – Lopinavir interactions with VP35 protein (PDB ID: 4GH9).

Source: Author.

The evaluation of the predicted conformations indicates that Lopinavir has a high potential for interaction with the receptor. A significant number of hydrogen bonds were identified (Figures 15, 16, 17, 18, 19) and both these interactions and the affinity energy levels obtained were used to ensure the stability of the formed complex. The molecular docking technique demonstrated effectiveness in selecting a potential structure. Furthermore, the detailed characterization of the hydrogen bonds corroborates the findings obtained in the docking evaluation, suggesting that these interactions play a relevant role in modulating the affinity energy.

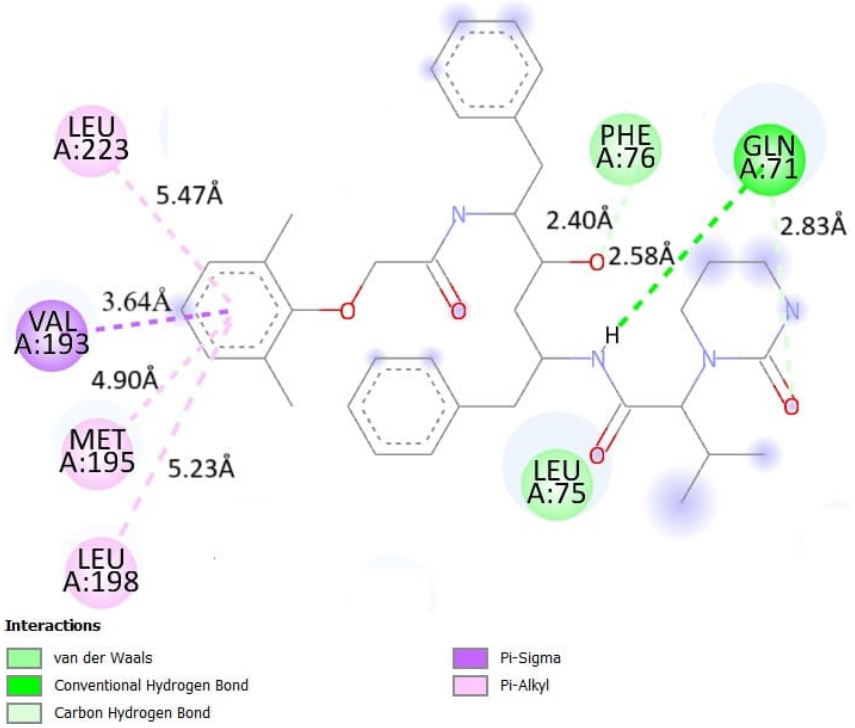

Figure 16 – Lopinavir interactions with VP24 protein (PDB ID: 4OR8).

Source: Author.

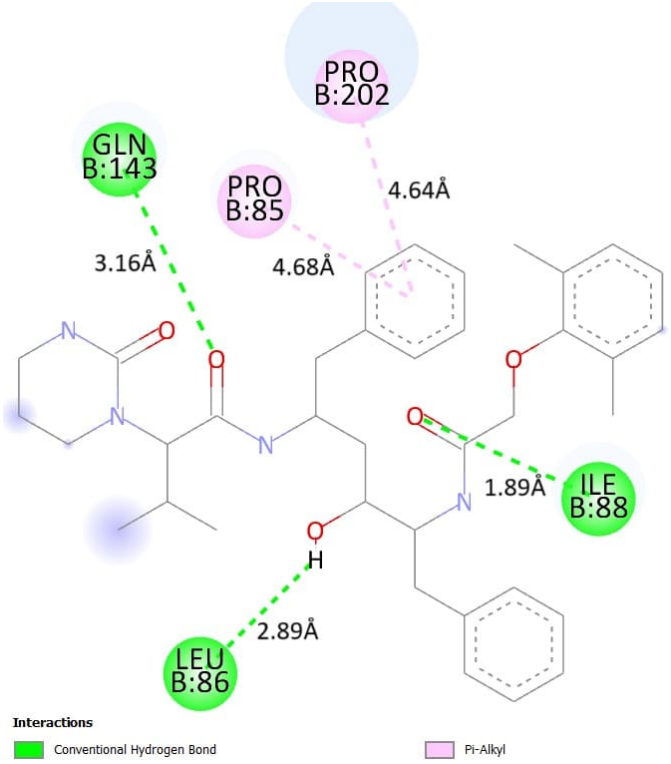

Figure 17 – Lopinavir interactions with VP40 protein (PDB ID: 5B0V).

Source: Author.

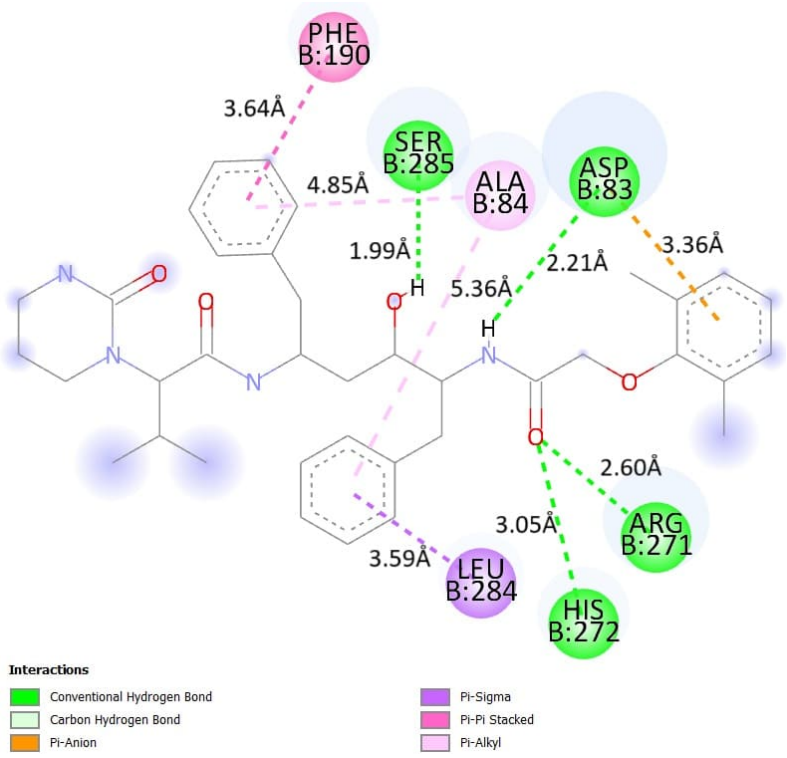

Figure 18 – Lopinavir interactions with NP protein (PDB ID: 5F5M).

Source: Author.

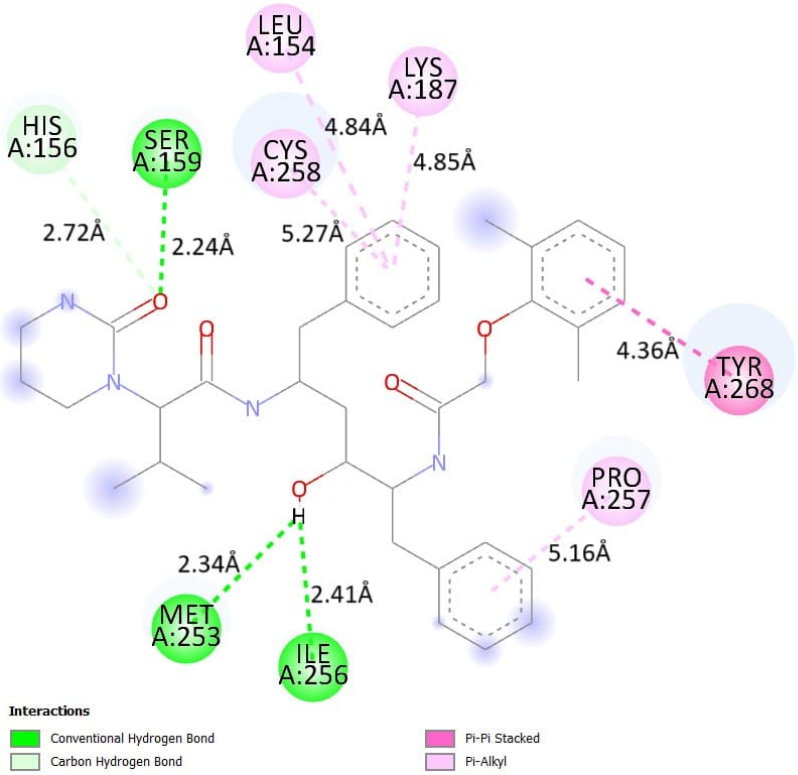

Figure 19 – Lopinavir interactions with VP30 protein (PDB ID: 5T3W).

Source: Author.

The conformations adopted by the ligands within the active site enable them to form associations with adjacent amino acids. Each conformation can establish interactions with different local residues. As binding energies decrease, the molecular interactions occurring between the ligand and the involved amino acids increase. Analyses performed through molecular docking, aimed at identifying and understanding binding interactions and affinities, corroborate previous findings, showing that GP2 interactions are predominantly mediated by hydrogen bonds (Figure 24). The interactions with VP35 (Figure 20), VP24 (Figure 21), VP40 (Figure 22), NP (Figure 25), and VP30 (Figure 23) involved the formation of hydrogen bonds and π-alkyl interactions with several amino acids. All macrostructures exhibited π-alkyl interactions within aromatic rings, indicating potential for reactivity. It was also observed that, in the various receptor–Nafamostat combinations evaluated, hydrophobic π-alkyl interactions were consistently preserved.

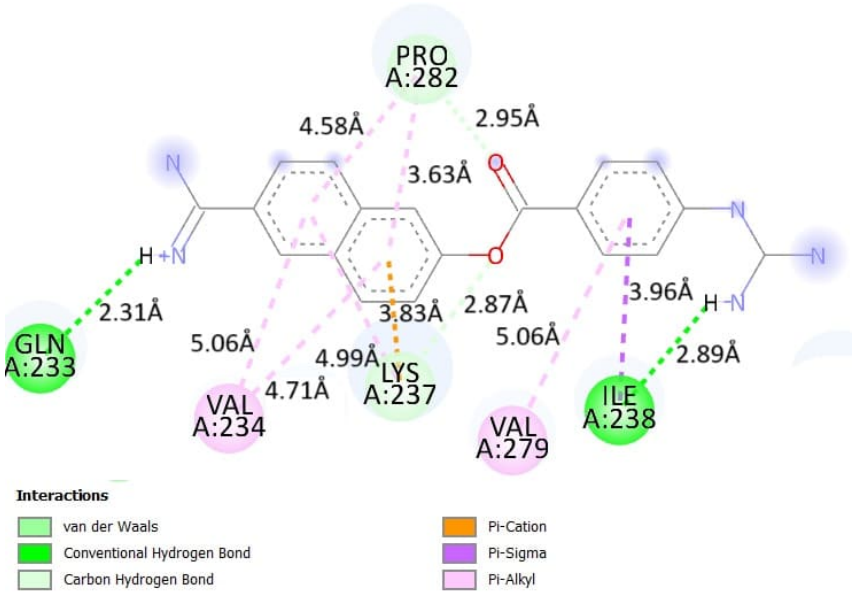

Figure 20 – Interactions of Nafamostat with VP35 protein (PDB ID: 4GH9).

Source: Author.

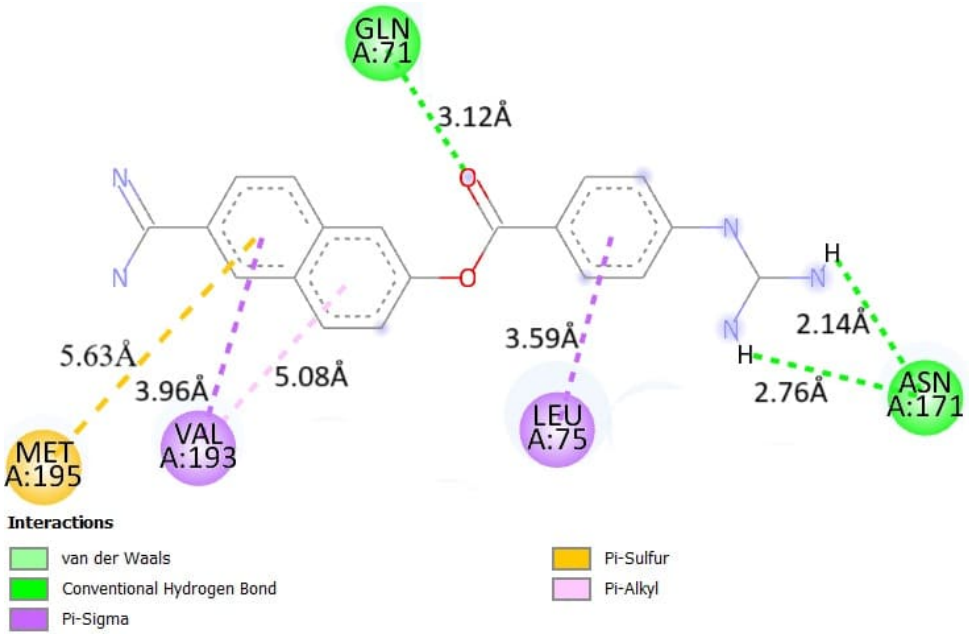

Figure 21 – Interactions of Nafamostat with VP24 protein (PDB ID: 4OR8).

Source: Author.

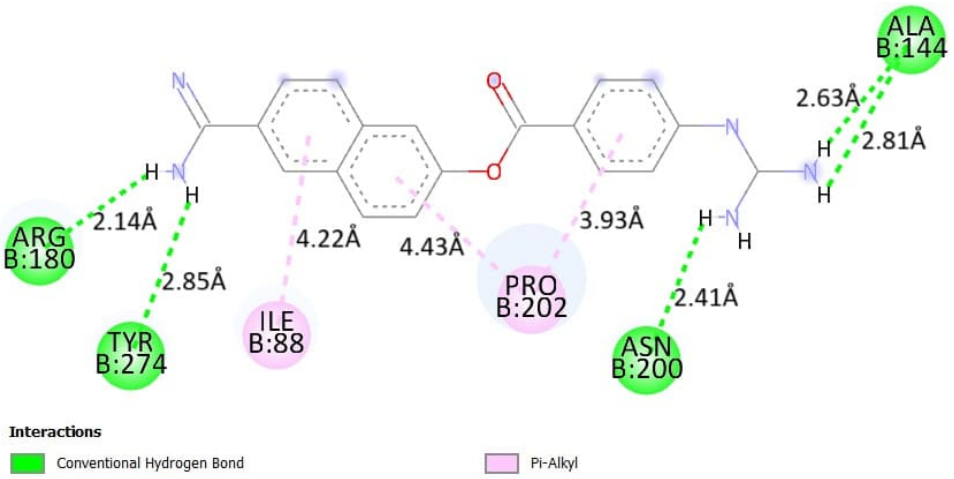

Figure 22 – Interactions of Nafamostat with VP40 protein (PDB ID: 5B0V).

Source: Author.

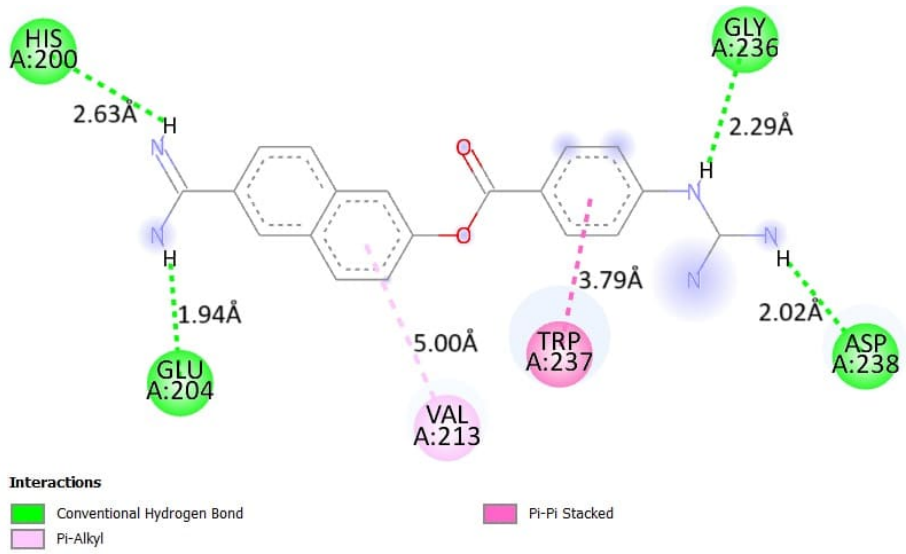

Figure 23 – Interactions of Nafamostat with VP30 protein (PDB ID: 5T3W).

Source: Author.

These results suggest a high probability of interaction, indicating promising trends in the development of therapies. In addition to investigating the effect of electronegative groups, other factors were also evaluated. Thus, inhibiting the relationship between the GP2 protein and the cellular receptor may reduce the level of viral spread.

For Nafamostat, in Figure 24, the combined presence of strong hydrogen bonds, C-H X interactions, and hydrophobic contacts indicates that Nafamostat forms a well-stabilized complex with the protein. The observed distances are within ranges suitable for effective non-covalent interactions, suggesting that the ligand has good potential to act as an inhibitor or modulator of the target protein. Interactions with conserved residues and proximity to the active site (as observed with Thr577, Ile611, Ile613, and Arg581) may also indicate functional and biological relevance

of the binding. Figure 25 of Nafamostat with NP highlights several conventional hydrogen bonds with residues Asp351, Glu354, and Gln346, in addition to attractive charge interactions with Glu350. Stacked Pi-Alkyl and Amide-Pi interactions are also observed, contributing to the stability of the complex. These interactions indicate a strong affinity of Nafamostat for the active site of the NP protein, reinforcing its potential as an inhibitor.

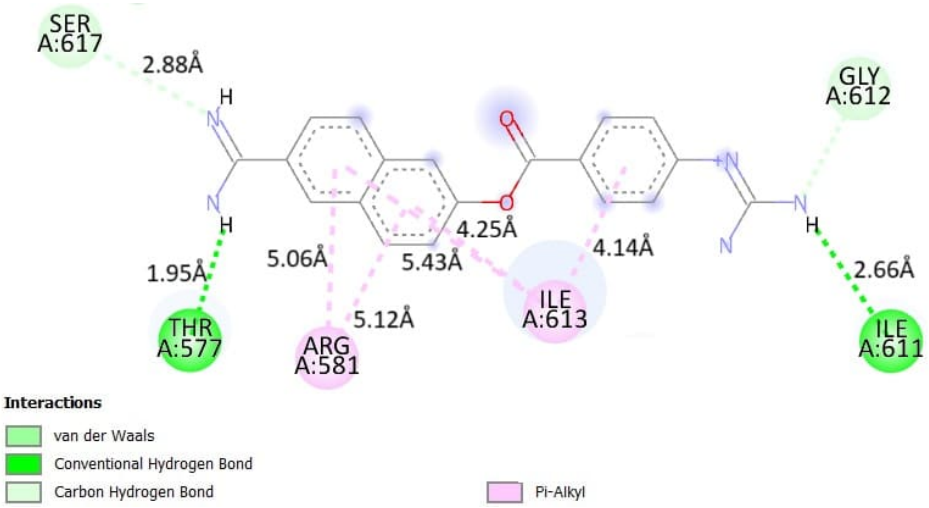

Figure 24 – Interactions of Nafamostat with GP2 protein (PDB ID: 4G2K).

Source: Author.

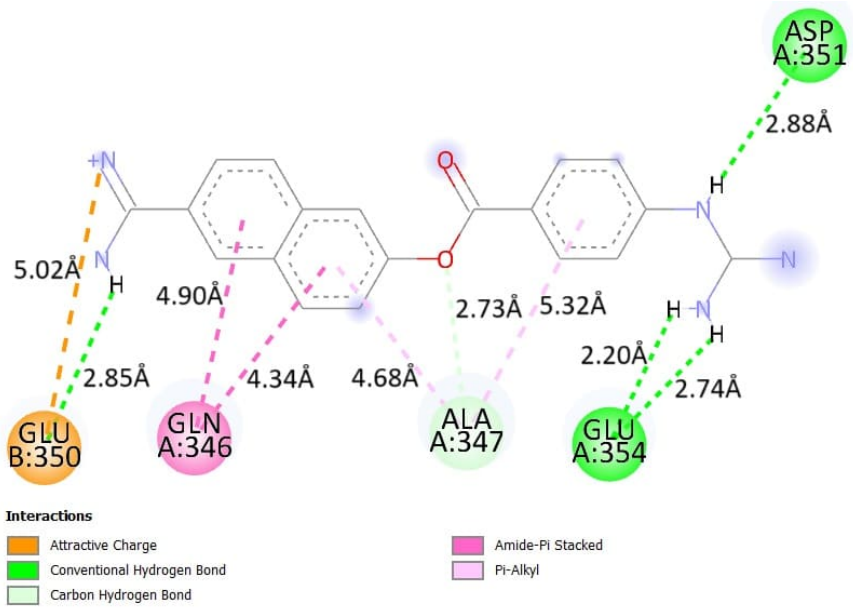

Figure 25 – Interactions of Nafamostat with NP protein (PDB ID: 5F5M).

Source: Author.

The molecular docking of Remdesivir is shown in Figures 26, 26, 27, 28, 29, 30 and 31. Redensivir and the MARV GP2 protein (Figure 26) revealed strong hydrophobic interactions, particularly of the alkyl and pi-alkyl types. Residues Leu570, Ile620, Ile613, Leu573, and Arg581

were identified as the main contact points, with distances ranging from 4.0 to 5.4 Å, indicating favorable positioning of the ligand in the active site. These hydrophobic interactions suggest that Remdesivir can effectively stabilize in the protein environment, favoring the functional blockade of the viral protein.

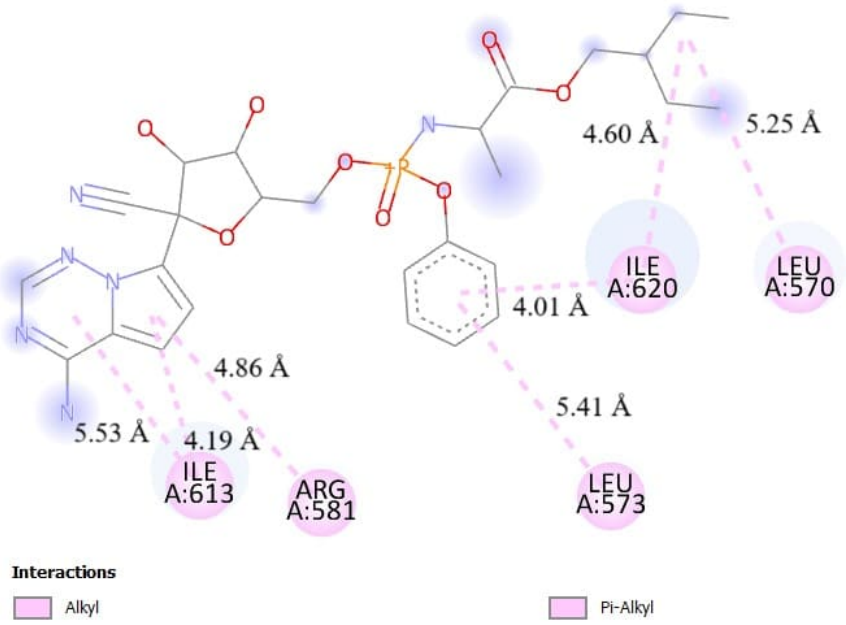

Figure 26 – Interactions of Remdesivir with GP2 Protein (PDB ID: 4G2K).

Source: Author.

The interaction between Remdesivir and the Marburg virus VP35 protein (Figure 27) revealed a robust binding pattern in the active site. Three hydrogen bonds were identified, notably the interactions between the oxygen of Remdesivir and residues Gln233 (2.89 Å) and Tyr317 (2.24 Å), characterized as conventional hydrogen bonds. Furthermore, the ligand molecule acted as a hydrogen donor in interaction with the OE1 atom of Gln233 (2.05 Å), and a C-H···N bond was observed between Gln233 and the nitrogen of Remdesivir (2.98 Å). A π-donor hydrogen bond was also identified between Gln233:NE2 and the π orbitals of Remdesivir (3.66 Å), which reinforces the stability of the complex.

Complementing the binding profile, several alkyl and π-alkyl hydrophobic interactions were observed with residues Val286, Lys211, Ala214, Leu215, Val234, Lys237, and Pro282, with distances ranging from 4.3 to 5.4 Å. These interactions indicate that Remdesivir efficiently accommodates in a predominantly nonpolar cavity, promoting stabilization of the ligand-receptor complex. The set of interactions observed suggests a high affinity of Remdesivir for VP35, supporting its potential as an inhibitor in molecular models of Marburg virus.

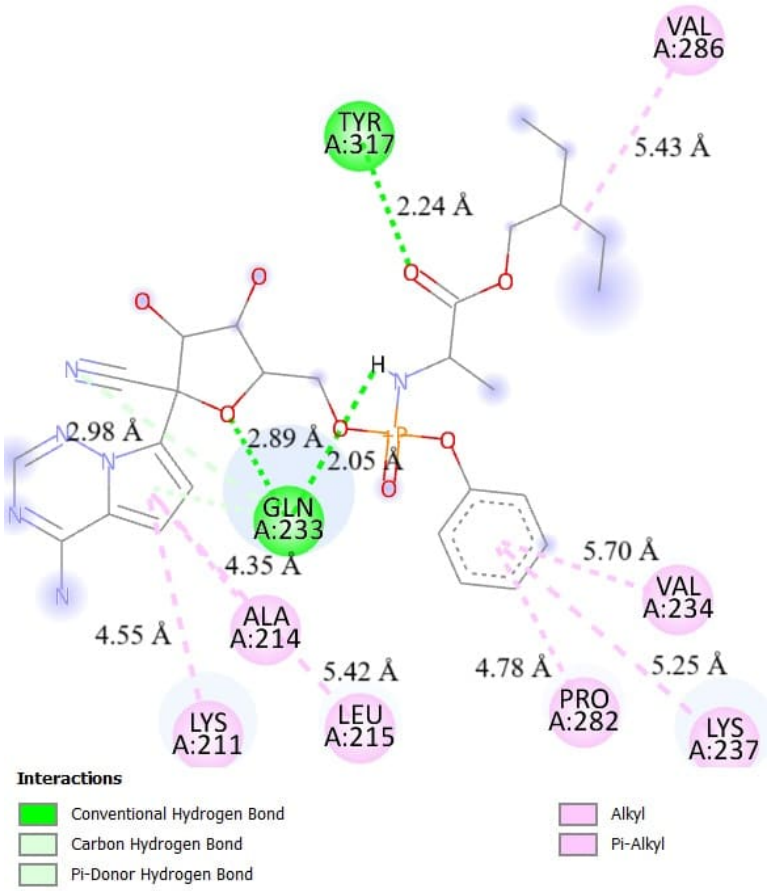

Figure 27 – Remdesivir interactions with VP35 protein (PDB ID: 4GH9).

Source: Author.

The molecular docking between Remdesivir and VP24 (Figure 28) was characterized primarily by conventional hydrogen bonds, as well as π-sigma and π-alkyl hydrophobic interactions. Five classical hydrogen bonds with distances ranging from 2.21 to 3.20 Å were identified, involving residues Gln71, Thr72, Asn194, and Met195, indicating strong complementarity between the donor and acceptor sites. Furthermore, two C-H···O/N bonds (weak hydrogen bonds) also contributed to the stabilization of the complex. In the hydrophobic context, π-sigma interactions with residues Leu75 and Trp69, and π-alkyl interactions with Val170, Val193, and Leu75, whose distances ranged from 3.58 to 5.11 Å, stand out.

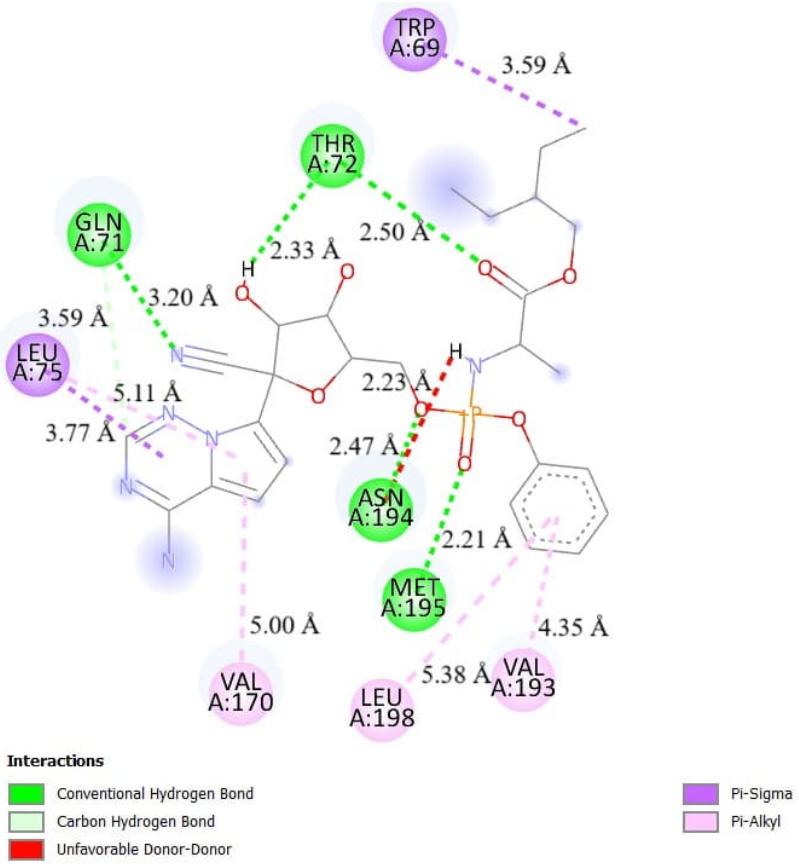

Figure 28 – Remdesivir interactions with VP24 protein (PDB ID: 4OR8).

Source: Author.

In the interaction of Remdesivir with VP30, in Figure 29, four conventional hydrogen bonds with distances ranging from 2.00 to 2.90 Å were identified, involving residues Cys258, Asp269, and Gln265, as well as an intramolecular interaction between atoms of the ligand itself. Additionally, three C–H···O bonds were observed with residues GLY155 and Pro257, in addition to an intraligand bond, all with distances consistent with weak but stabilizing interactions.

Regarding hydrophobicity, two π–π T-shaped interactions between the aromatic ring of Remdesivir and residue Tyr268 stand out, with distances of approximately 4.87 Å, suggesting coupling by perpendicular stacking. π–alkyl interactions were also recorded with residues Tyr268, Pro257 and Leu154, ranging from 4.71 to 5.42 Å, which reinforce the anchoring of the drug in hydrophobic regions of the active cavity.

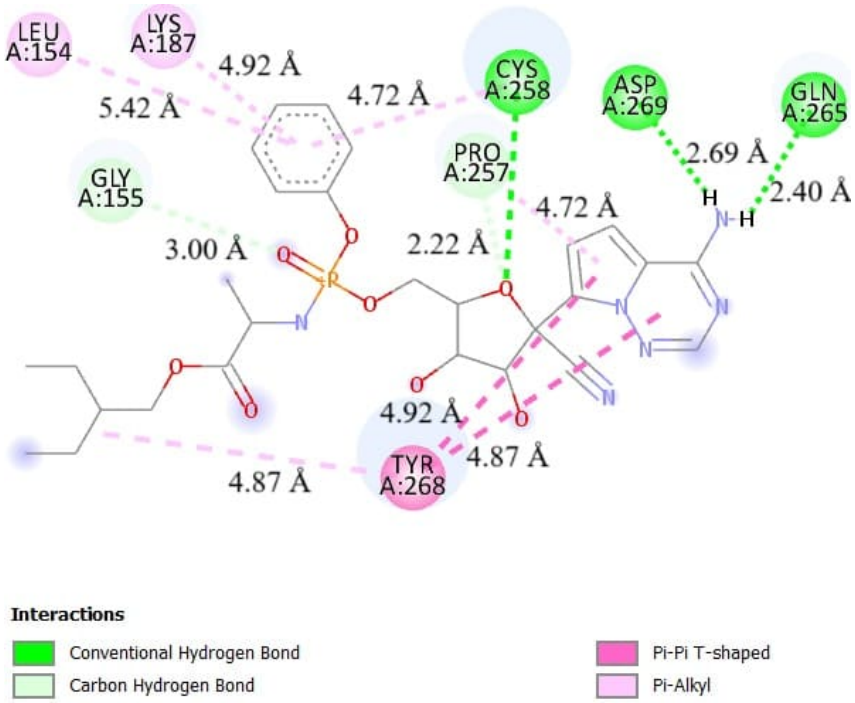

Figure 29 – Remdesivir interactions with VP30 protein (PDB ID: 5T3W).

Source: Author.

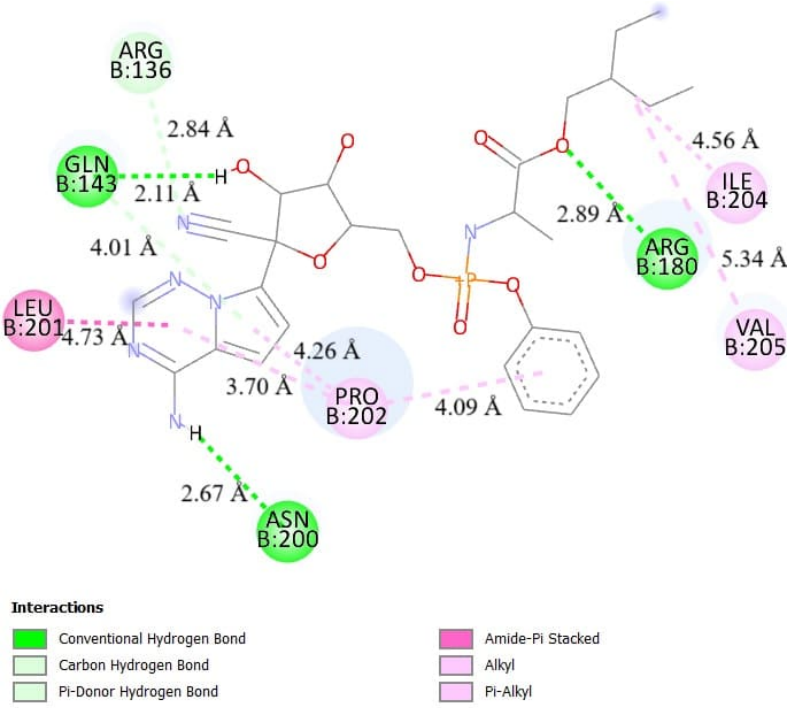

Figure 30 – Remdesivir interactions with VP40 protein (PDB ID: 5B0V).

Source: Author.

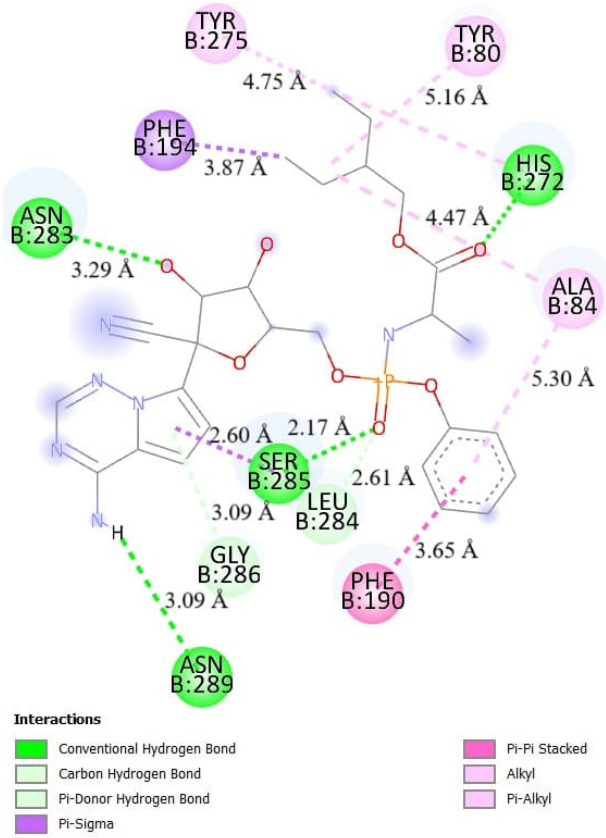

Figure 31 – Remdesivir interactions with NP protein (PDB ID: 5F5M).

Source: Author.

In this study, it was observed that, in most combinations between the receptor and Ivermectin evaluated, conventional hydrogen bonds were maintained. This characteristic highlights the potential for interaction and suggests its possible use as an antiviral therapy. In addition to the influence of electronegative groups, other factors were also taken into account. Thus, interrupting the binding between the GP2 protein and the cellular receptor emerges as a promising strategy for reducing viral infection. Ivermectin demonstrated the highest binding affinity, in terms of modulus, with the binding site present in all macrostructures evaluated. Evidence suggests that it exhibits superior affinities in the various structures studied, highlighting its potential as a broad-acting antiviral agent effective in protecting against new and resurgent viral diseases, such as MARV.

5.3 Molecular Electrostatic Potential Analysis

The biological effect of a ligand is directly related to its affinity for the target receptor. During the docking stage in the enzymatically active domain, certain conformations are favored to increase interactions with specific residues in the protein. This contributes to increased electrostatic and hydrophobic interactions, as well as the energy associated with binding affinity, favoring the establishment of an enzyme-ligand complex.

The interaction investigation revealed that groups present in the various ligand conformations analyzed interact systematically with enzyme residues, indicating that these groups are crucial to the pharmacological activity of these compounds. The conformational evaluation revealed that the conformational regions explored by each ligand were quite distinct.

The best positions obtained in the DOC were used to generate MEP maps, which identified regions with the greatest efficiency in accommodating inhibitors, both structurally and electrostatically. These regions utilize a specific set of interactions with each ligand. MEP has been used to understand and estimate the reactivity of ligands in electrophilic and nucleophilic processes.

The MEP significantly contributes to the identification of initial receptor-ligand interactions and serves as an important indicator of the bioactive state. The various values of the molecular surface electrostatic potential are represented by colors: red reveals the sites of the most negative potential, while blue shows areas with the most positive electrostatic potential, and green represents sites of intermediate potential. The potential scale is verified in the following order: red < orange < yellow < green < blue, as illustrated in Figure 32.

Therefore, the electrostatic potential profiles of inhibitors significantly influence receptor binding, directly affecting inhibition efficacy. The MEP maps generated for the ligands highlight highly electronegative regions (in red), generally located on oxygen atoms, which participate in relevant chemical interactions. In polar molecular species, such as the analyzed drugs, the MEP highlights regions of high or low electron density, revealing so-called "electron wells."

It was also found that the molecular forms of Ivermectin and Lopinavir have a more pronounced electronegative character, which significantly contributes to the electron mobility in their structures, followed by Remdesivir and Nafamostat. Therefore, the MEP serves as a valuable indicator of the preferred sites for electrophilic and nucleophilic attacks, as well as for understanding molecular recognition during the interaction phenomenon.

As illustrated in Figure 32, the chemically reactive sites and the relative reactivity of the atoms in the ligands are shown. The MEP has proven effective in identifying receptor regions more likely to interact with electrophilic or nucleophilic species and has been widely used to determine the ideal position of ligands in the molecular complex. Regions with a negative electrostatic potential (shades of red) indicate greater attraction for protons, while positive regions (shades of blue) indicate repulsion. Negative areas of the MEP are associated with electrophilic reactivity, while positive areas are associated with nucleophilic reactivity.

Finally, the intensity of the electrostatic field directly influences the interaction between the substrate and the receptor, as molecular recognition occurs thanks to the complementarity of these surfaces.

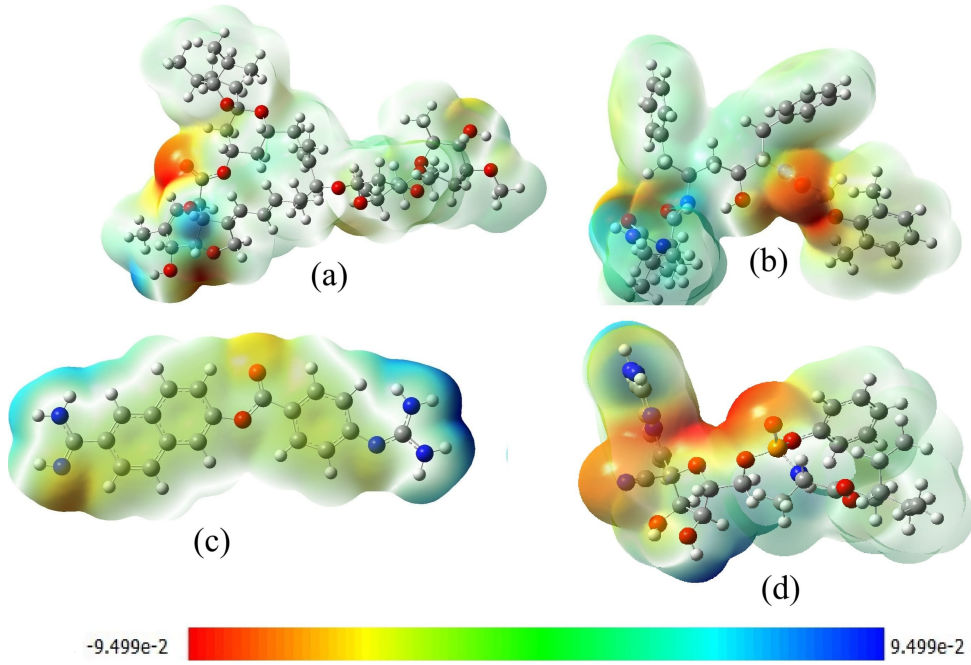

Figure 32 – The molecular electrostatic potential for the title compound in: a) Ivermectin, b) Lopinavir, c) Nafamostat, and (d) Remdesivir.

Source: Author.

5.4 MD Results

5.4.1 RMSD

RMSD is a metric commonly used to analyze the average distance between atoms in superimposed structures, essential for comparing their similarity. In addition to indicating the degree of structural similarity, RMSD also provides clues about the equilibrium of the simulated system, signaling the moment at which the structure reaches the average conformation that demonstrates greatest stability. At the beginning of simulations, a marked increase in RMSD parameters is common, reflecting initial adjustments until a plateau is reached, which suggests structural stability. Investigating RMSD results over time enables us to determine the time required for structures to reach a state of stabilization.

To determine the stability of complexes formed between proteins and ligands, molecular dynamics simulations were run for 100 nanoseconds with three drug candidates in different MARV protein structures. The RMSDs observed for each complex were then analyzed (Figures 33, 34 and 35). This metric is crucial for assessing the stability of the complexes during simulation, with lower values indicating greater stability. Overall, the average RMSDs ranged from 0.5 to 2.0 Å.

Figure 33 shows that the Ivermectin compounds proved to be more stable during interactions with VP24, VP35 and VP40. However, in the simulations with Ivermectin, small oscillations

were observed between 20 and 40 ns and from 50 to 70 ns, with a general stability pattern for the GP2 protein. On the other hand, in the simulations involving Nafamostat, shown in Figure 35, good RMSD values were recorded for interactions with GP2 and VP24, suggesting possible stability. Despite this, a more pronounced positional change of the ligand was observed between 10 and 20 ns in the VP35 structure, although the simulation overall showed good stability.

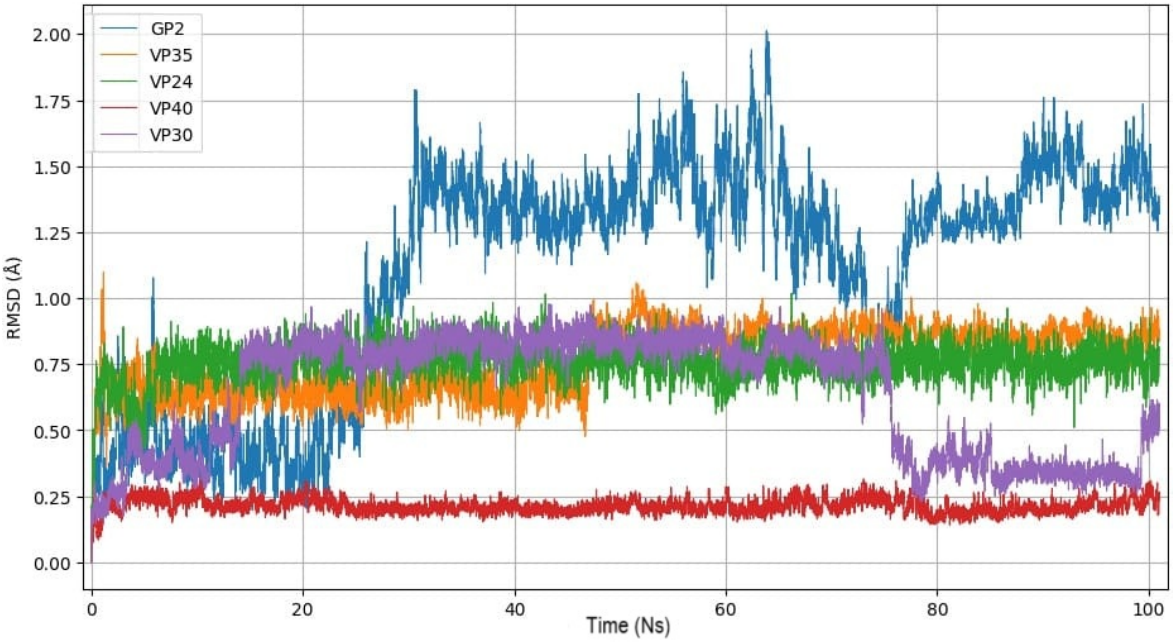

Figure 33 – RMSD versus time of receptors with Ivermectin

Source: Author.

Lopinavir, Figure 34, presented the highest average RMSD values; the most stable binding was observed with VP35 and VP40, while GP2 resulted in the largest deviation values. Overall, the Ivermectin-containing complex proved to be more stable compared to the analyzed macrostructures (Figure 33), although significant positional variations occurred, possibly due to the specific nature of the proteins involved. The six complexes analyzed reached an equilibrium state between 80 and 100 ns, with subsequent progressive stabilization.

The initial stabilization observed in the RMSD was expected, reflecting the cooperation between the inhibitor and the target protein, which reduces the protein's flexibility. This stability is attributed to the compound's affinity for the catalytic site. Additionally, a detailed examination of the protein backbone mobility revealed that the Ivermectin interaction area exhibited less flexibility, which impacted the extent of displacement throughout the simulation. Such structural interactions favored more stable structural forms. In the context of these interactions, it is noteworthy that the electrostatic effects between polar groups and the surrounding environment can be described by models based on dipoles subjected to force fields, allowing the construction of more accurate electrostatic charge models for molecules with polar bonds.

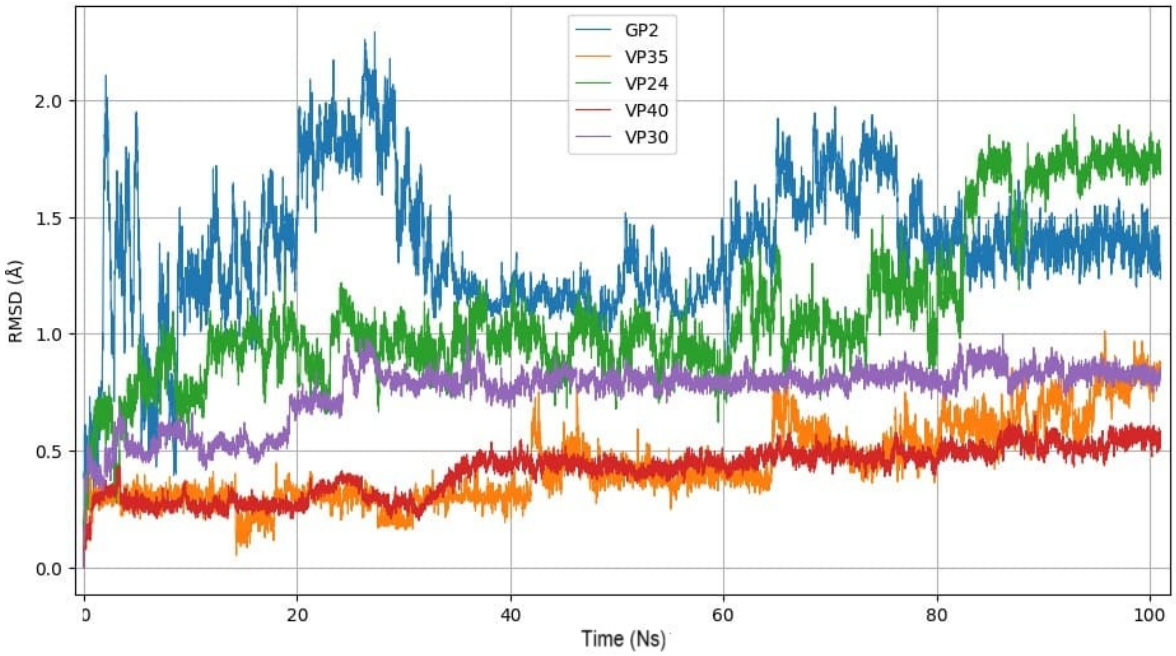

Figure 34 – RMSD versus time of receptors with Lopinavir

Source: Author.

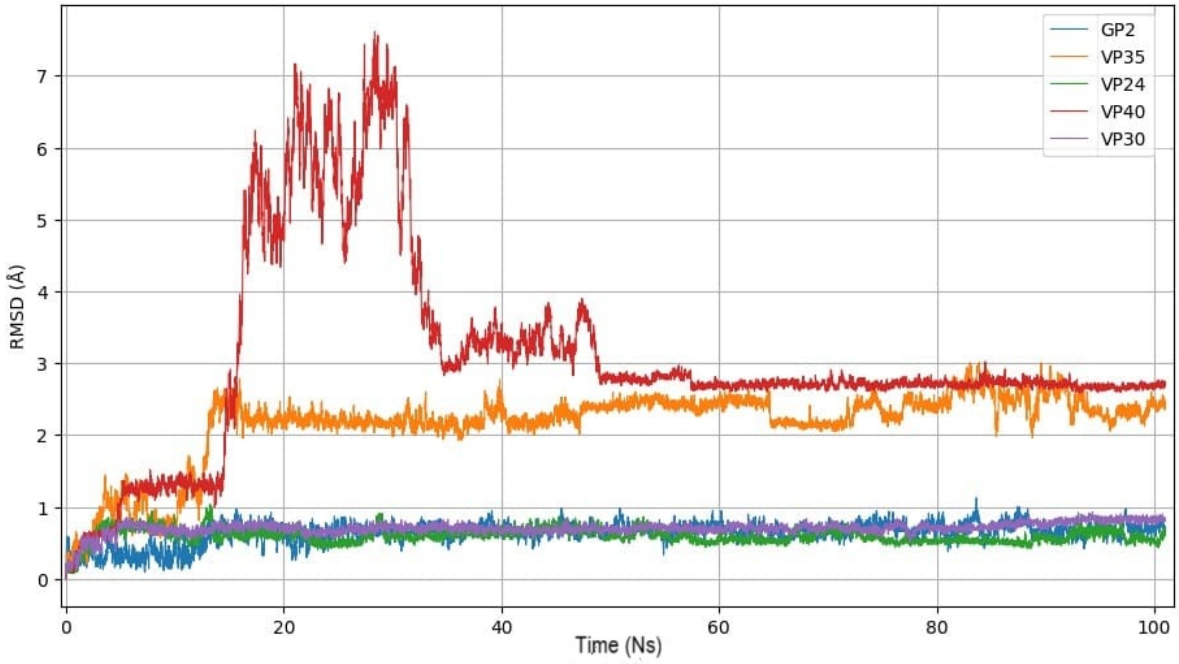

Figure 35 – RMSD versus time of receptors with Nafamostat

Source: Author.

5.5 Hydrogen Interactions Over Time

Interactions over time were investigated by quantifying the hydrogen bonds formed between the ligands and the MARV structures. The average hydrogen bonds (HBs) are represen-

ted in Table 3 and presented in Figures 38, 39, 40, 36 and 37, reveal that Ivermectin established greater stability with VP40 throughout the three-step simulation, with peaks of four hydrogen bonds, compared to the other structures throughout the computational calculation. Although it presented a lower number of interactions with VP35, brief intervals were observed where no hydrogen bonds were present, indicating that the interaction is non-permanent but recurrent. This may be related to the structural flexibility of the binding region, ligand movement, or the presence of water or ions in the binding site.

Table 3 – Analysis of hydrogen bonds between Ivermectin and Marburg virus proteins during a 100 ns simulation.

Complex	**Peak**	**Range**	**Stability**	**Observations**
GP2–Ivermectin	3	1–2	Moderate	Isolated peaks between 35–45 ns.
VP24–Ivermectin	4	1–2	High	Interactions with some peaks; reasonable affinity.
VP30–Ivermectin	4	1–2	High	Continuous profile with variation; pattern similar to VP24.
VP35–Ivermectin	3	1–2	Moderate	Good interaction up to 40 ns; subsequent decline in bonds.
VP40–Ivermectin	5	2–4	High	Better interaction profile; consistent and intense connections.

Source: Author.

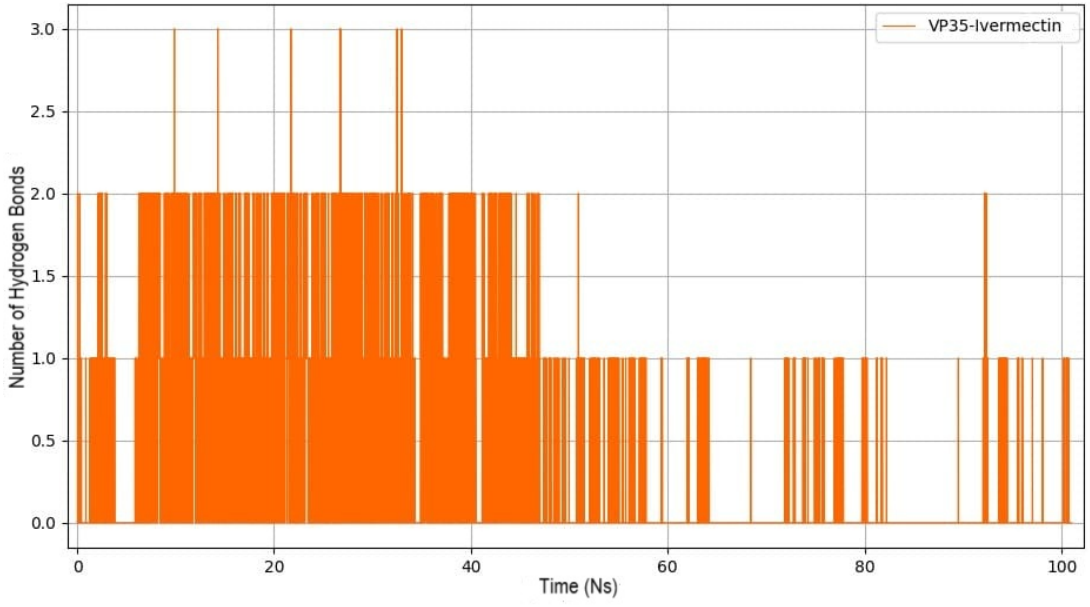

Figure 36 – Number of Hydrogen Bonds of VP35 with Ivermectin over Time

Source: Author.

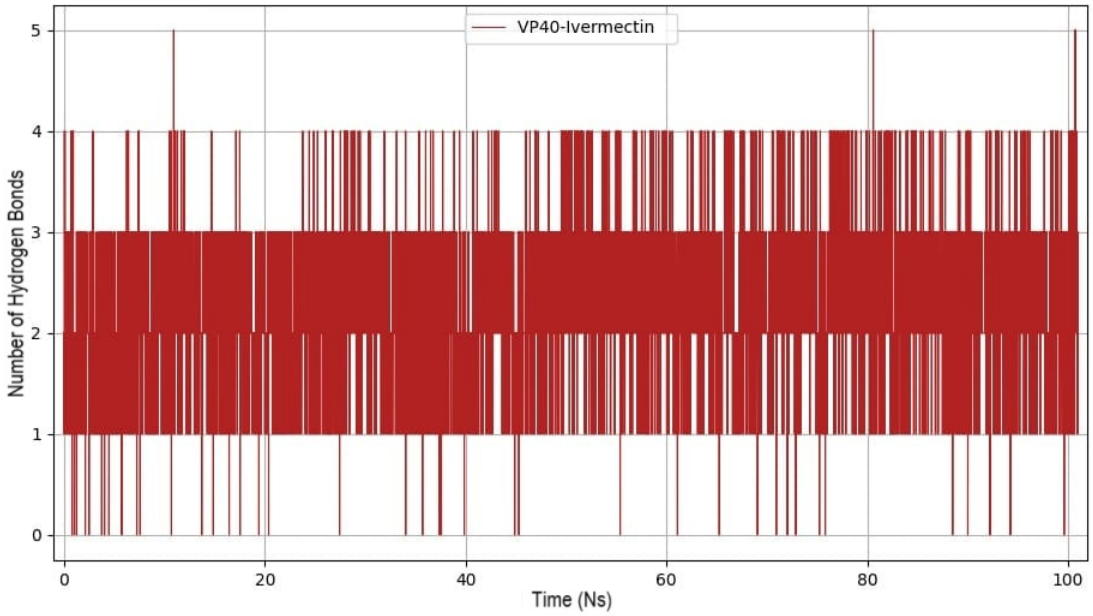

Figure 37 – Number of Hydrogen Bonds of VP40 with Ivermectin over Time

Source: Author.

The correlation between the number of hydrogen bonds and the RMSD values suggests that Ivermectin exhibits good stability over time. For GP2, Figure 38, between 40–60 ns and 70–90 ns, a higher density of two simultaneous bonds is observed, suggesting more consistent interactions in these segments. Although hydrogen bonds are not the only force involved (hydrophobic and van der Waals interactions are also important), their behavior over time in the structures is a good indicator of the complex's affinity and stability.

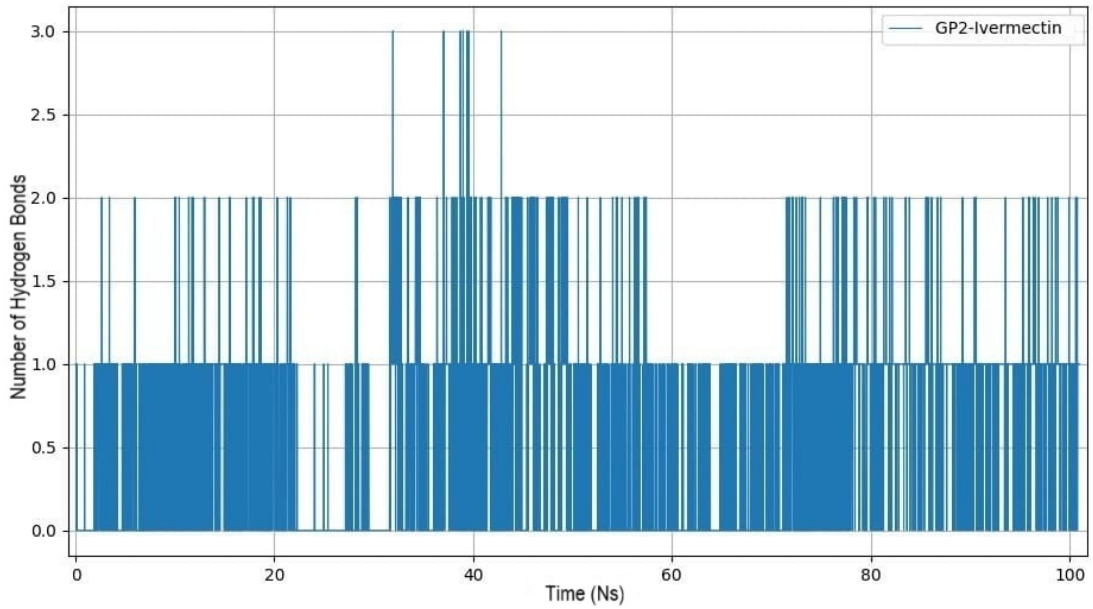

Figure 38 – Number of Hydrogen Bonds of GP2 with Ivermectin over Time

Source: Author.

These results indicate that Ivermectin exhibits varying levels of interaction with Marburg virus proteins, with strong binding to VP40, followed by VP24 (Figure 39) and VP30 (Figure 40), while GP2 and VP35 exhibited less stable interactions. These data are fundamental for understanding the molecular mechanisms of Ivermectin's action and its potential application in combating the Marburg virus.

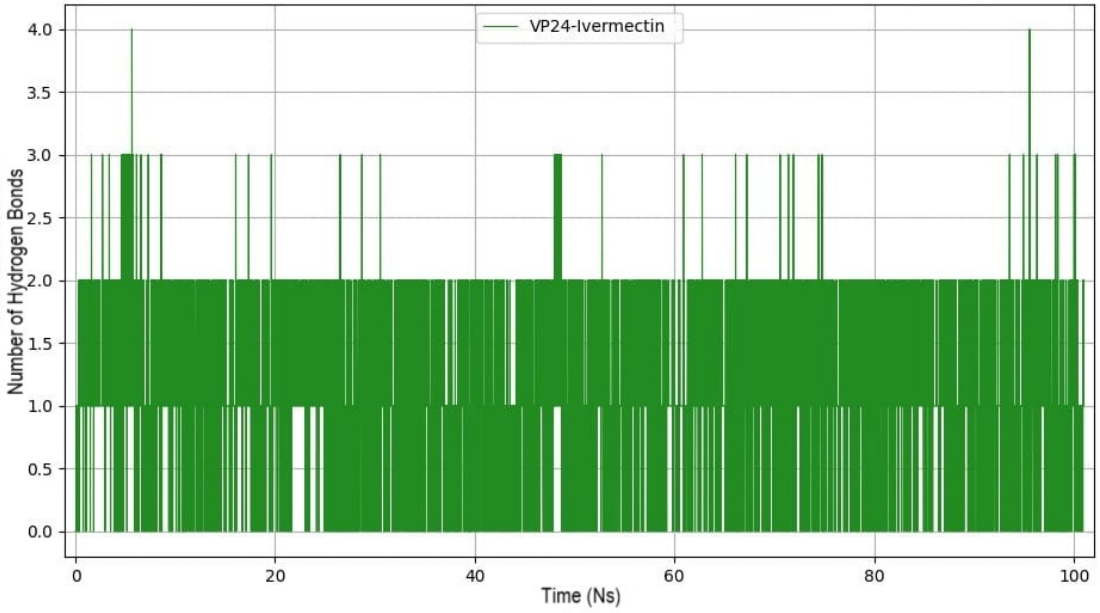

Figure 39 – Number of Hydrogen Bonds of VP24 with Ivermectin over Time

Source: Author.

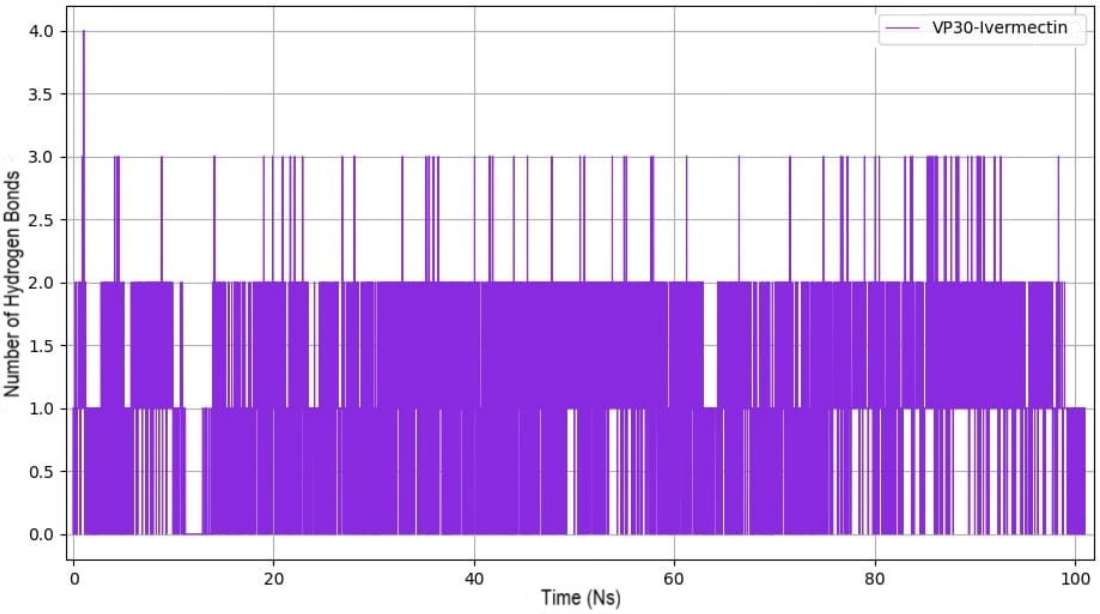

Figure 40 – Number of Hydrogen Bonds of VP30 with Ivermectin over Time

Source: Author.

Hydrogen bonds constitute a specific type of dipole-dipole intermolecular interaction that occurs when a hydrogen atom, previously bonded to a highly electronegative atom, approaches another electronegative atom with a non-bonding electron pair. As shown in Table 4 and Figures 41, 42, 43, 44 and 45, the compound Lopinavir exhibited an average of one to two hydrogen bonds with the MARV structures throughout the simulation, demonstrating its interaction potential. It is also observed that the interaction with the VP24 structure revealed reduced values at the end of the simulation and for GP2 at the beginning.

Hydrogen bonds are generally more intense than van der Waals forces or simple dipole-dipole forces, although they are still less energetic than covalent or ionic bonds. The analysis between receptor and ligand revealed relevant pharmacophoric characteristics, which were corroborated by the results of DOC and MD. Furthermore, hydrogen bonds play a crucial role in modulating the structural flexibility of proteins, which can potentially directly affect their stability and biological function.

Table 4 – Analysis of hydrogen bonds between Lopinavir and Marburg virus proteins during a 100 ns simulation.

Complex	**Peak**	**Range**	**Stability**	**Observations**
GP2–Lopinavir	8	0–5	High	Intense peak between 50–60 ns; bindings vary over time.
VP24–Lopinavir	5	0–3	Moderate	Constant variations, with notable peaks between 10–20 ns and 70–80 ns.
VP30–Lopinavir	4	0–2	Moderate	Constant variations, with notable peaks between 10–20 ns and 70–80 ns.
VP35–Lopinavir	3	0–2	Low	Sparse binding and low peaks, mainly between 70–80 ns.
VP40–Lopinavir	6	0–4	Moderate	High peak at the beginning and gradual decline after 30 ns.

Source: Author.

The results indicate that the GP2–Lopinavir complex presented the largest binding peak, reaching up to 8 simultaneous bonds, with high stability observed especially between 50 and 60 ns, suggesting a strong interaction in that time range.

The VP24–Lopinavir complex demonstrated moderate stability, with peaks of up to 5 bonds and constant variations over time, including significant peaks between 10–20 ns and 70–80 ns. This indicates a dynamic, but less constant, affinity compared to GP2.

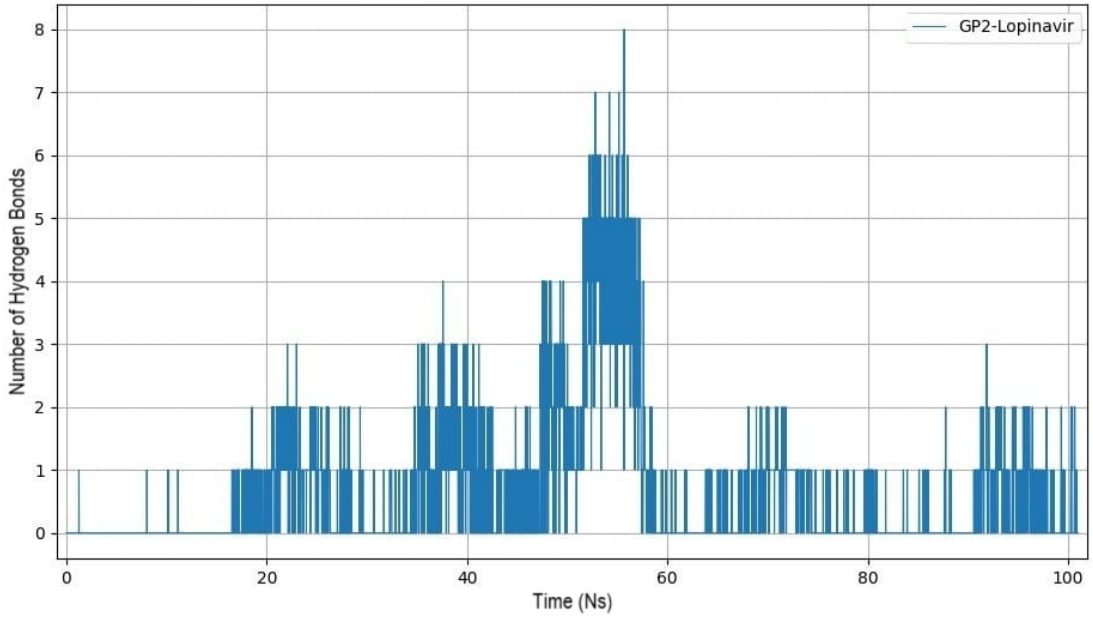

Figure 41 – Number of Hydrogen Bonds of GP2 with Lopinavir over Time

Source: Author.

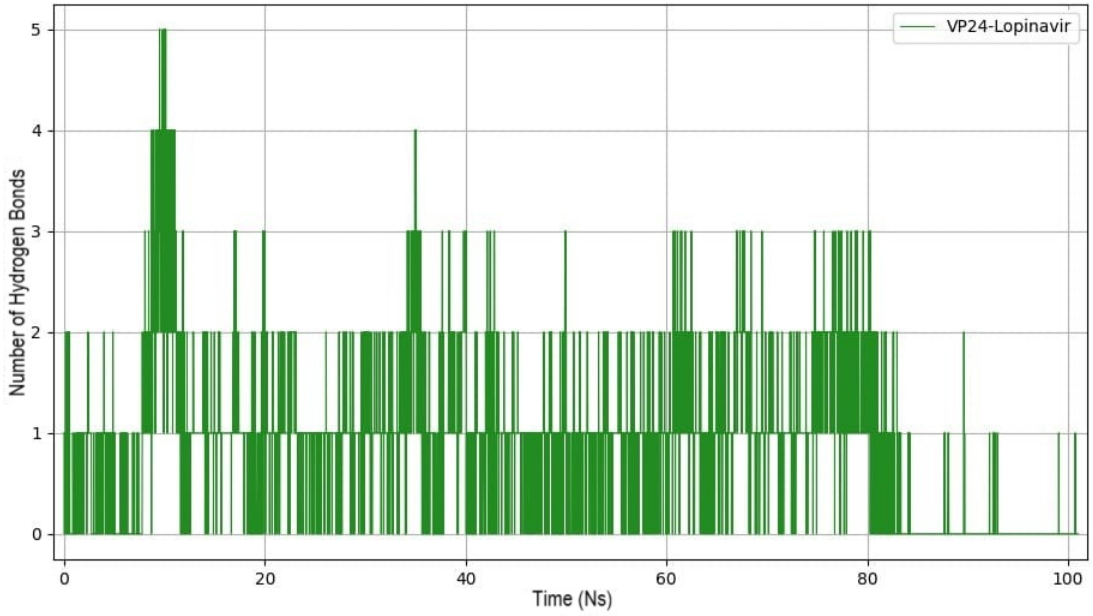

Figure 42 – Number of Hydrogen Bonds of VP24 with Lopinavir over Time

Source: Author.

The interaction with VP30, Figure 43,exhibited similar behavior, with a maximum peak of 4 bonds and moderate stability, characterizing continuous binding with fluctuations throughout the simulation. VP35–Lopinavir,Figure 44, on the other hand, showed sparser and less stable bonds, reaching a maximum peak of 3 bonds, mainly concentrated in the 70–80 ns range, indicating lower affinity.

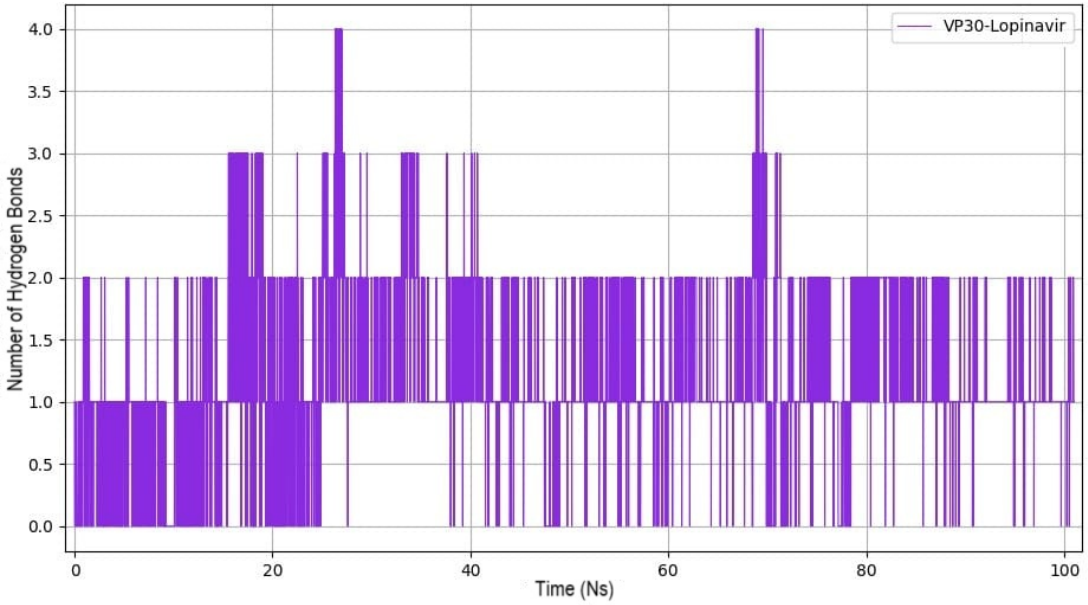

Figure 43 – Number of Hydrogen Bonds of VP30 with Lopinavir over Time

Source: Author.

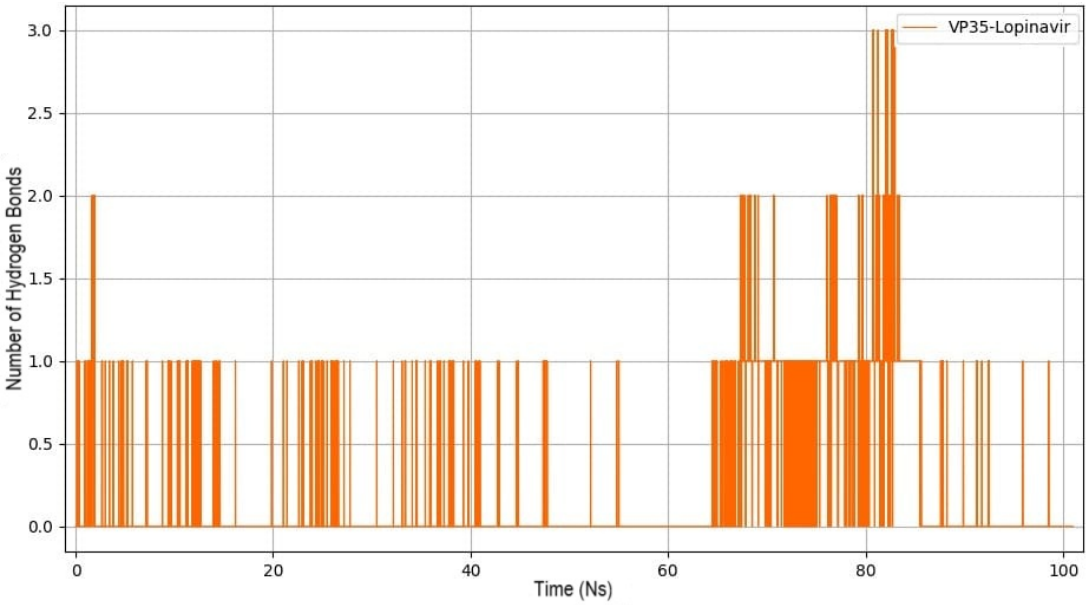

Figure 44 – Number of Hydrogen Bonds of VP35 with Lopinavir over Time

Source: Author.

Finally, the VP40–Lopinavir complex exhibited a peak of up to 6 bonds (Figure 45), with moderate stability. A pronounced peak was observed in the early stages of the simulation, followed by a gradual decline in the number of bonds formed after 30 ns, suggesting a more effective interaction early in the process.

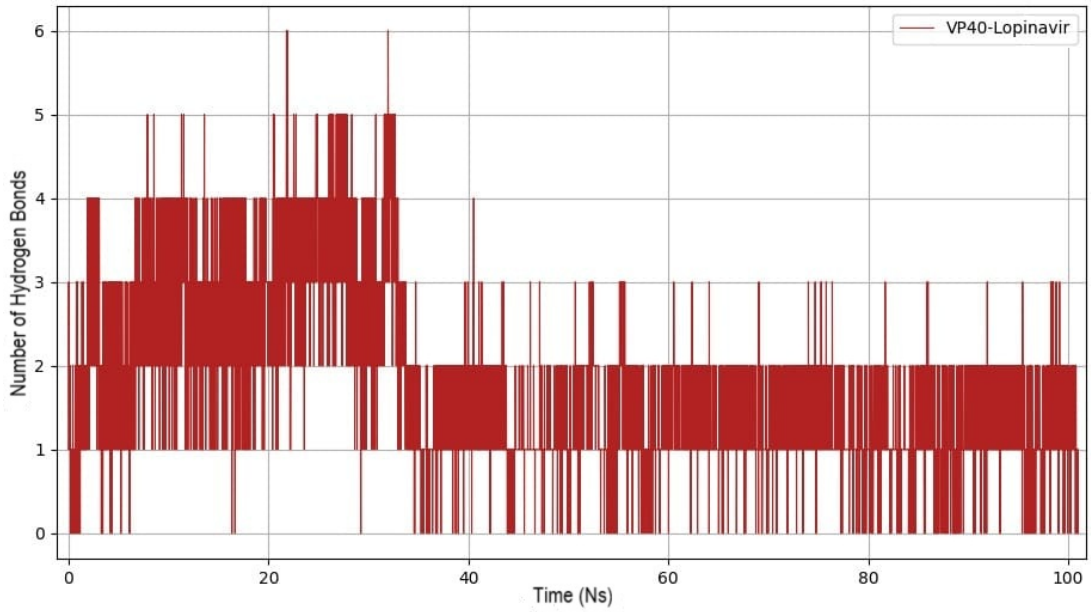

Figure 45 – Number of Hydrogen Bonds of VP40 with Lopinavir over Time

Source: Author.

These data indicate that Lopinavir exhibits varying levels of interaction with Marburg virus proteins, with the highest affinity for GP2, followed by VP40, VP24, and VP30, and the lowest affinity for VP35. This information is relevant to understanding the antiviral potential of Lopinavir against this virus and may aid in the development of targeted therapies.

Hydrogen bonds are attractive intermolecular forces that occur when a dipole-dipole interaction occurs between a hydrogen atom covalently bonded to a highly electronegative element and another electronegative atom located nearby. In the case of the Namostat molecule, its linear structure favors the formation of these bonds, which was reflected in the results obtained with the drug. Among all the simulations performed, this compound presented the highest number of hydrogen bonds per unit time for the GP2 (Figure 46), VP24 (Figure 47), VP30 (Figure 48), VP35 (Figure 49), and VP40 (Figure 50) interactions , which maintained an average of approximately four to five bonds throughout the simulation, with peaks of six to eight bonds, as shown in table 5.

This behavior corroborates the structural stability data observed by RMSD. The predominance of these interactions can be explained by the presence of oxygen and nitrogen atoms in the Namostat structure, whose lone electron pairs and high electronegativity facilitate bond polarization. This allows an electrostatic attraction to occur between the hydrogen of one molecule and the oxygen of another, thus forming a hydrogen bond.

Table 5 – Analysis of hydrogen bonds between Nafamostat and Marburg virus proteins during a 100 ns simulation.

Complex	**Peak**	**Range**	**Stability**	**Observations**
GP2–Nafamostat	6	2–5	High	Continuous and stable interactions, with minimal fluctuations throughout the simulation.
VP24–Nafamostat	8	3–6	High	Continuous and stable interactions, with minimal fluctuations throughout the simulation.
VP30–Nafamostat	6	3–5	High	Uniform and persistent profile, maintaining stable interactions over long periods.
VP35–Nafamostat	8	2–5	High	High connection frequency; dynamic profile with well-distributed stability.
VP40–Nafamostat	7	3–5	High	Progressive increase in stability after 40 ns, with a constant number of connections.

Source: Author.

These bonds are considered special intermolecular interactions, present only in compounds whose hydrogen atoms are bonded to strongly electronegative elements, such as oxygen or nitrogen. Compared to other interactions such as dipole-dipole and London dispersion forces, hydrogen bonds are significantly more intense, directly influencing the stability and functionality of the structures involved. The GP2–Nafamostat complex exhibited stable behavior, with 2 to 5 bonds maintained continuously throughout 100 ns, with a peak at 6 bonds. This indicates strong affinity and persistence of hydrophilic interactions with protein residues.

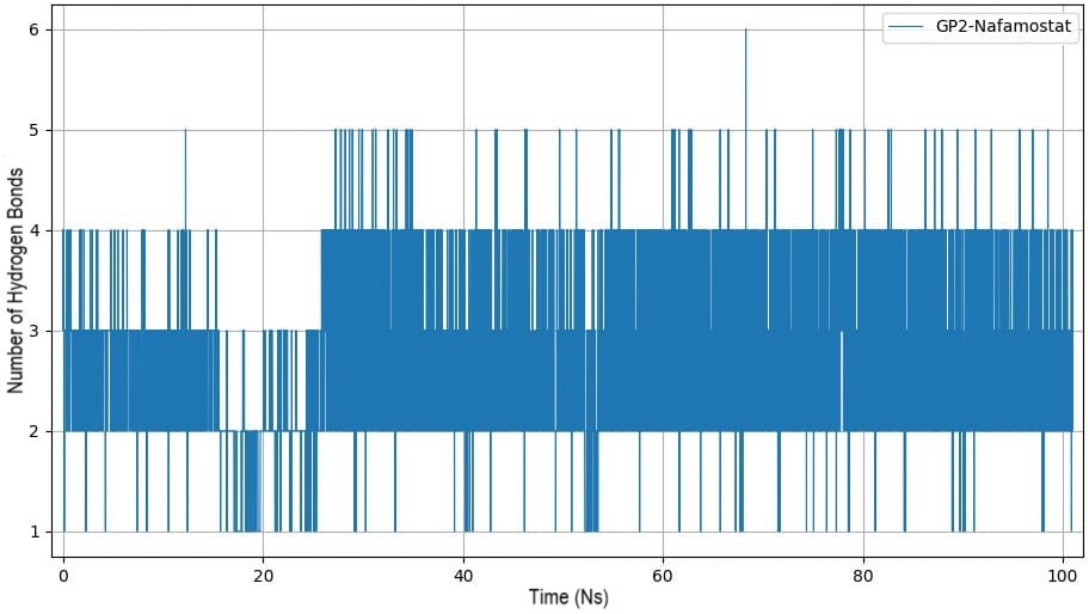

Figure 46 – Number of Hydrogen Bonds of GP2 with Nafamostat over Time

Source: Author.

For VP24–Nafamostat, the highest number of hydrogen bonds was observed among all complexes, with peaks of up to 8 bonds and a range predominantly between 3 and 6 hydrogen bonds. The density and consistency of these interactions suggest high conformational compatibility between the drug and the VP24 protein.

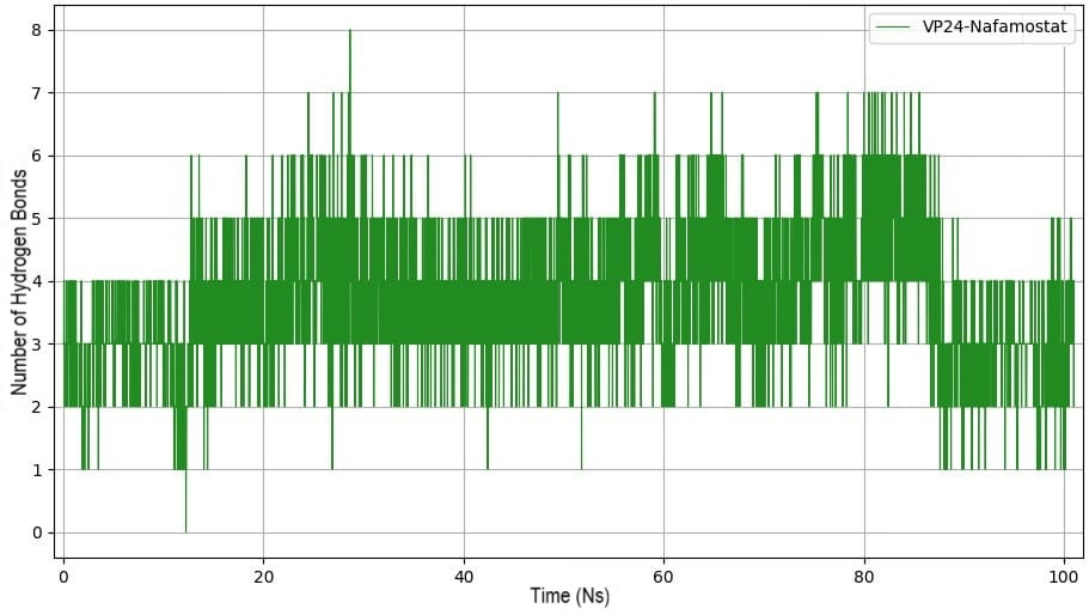

Figure 47 – Number of Hydrogen Bonds of VP24 with Nafamostat over Time

Source: Author.

The VP30–Nafamostat complex exhibited a uniform pattern, characterized by a continuous range of 3 to 5 bonds and very few interruptions, indicating prolonged stability of the

intermolecular interaction and reinforcing its therapeutic potential.

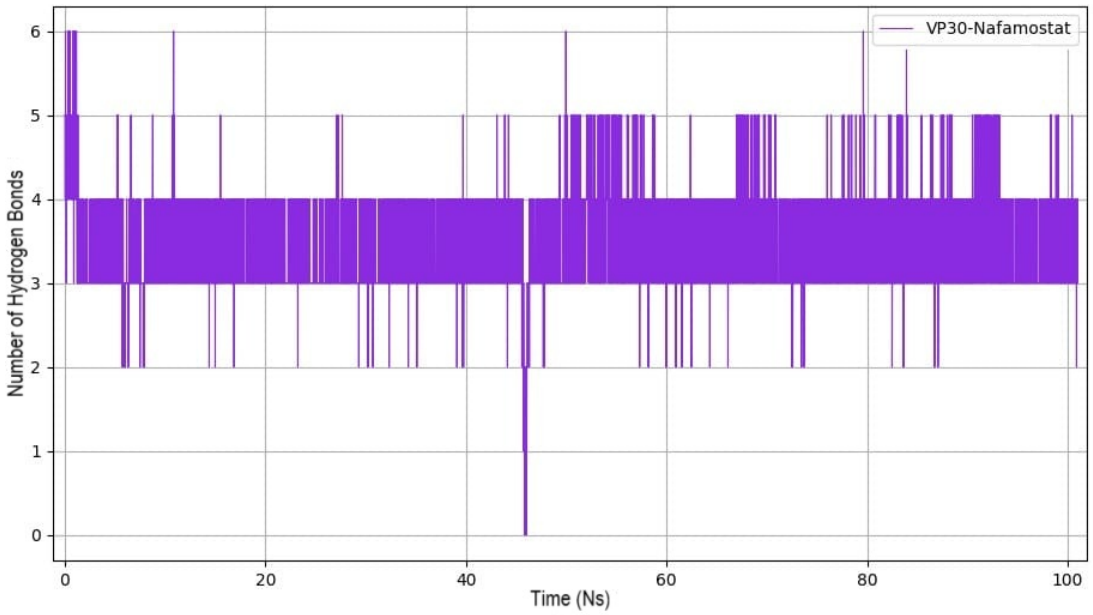

Figure 48 – Number of Hydrogen Bonds of VP30 with Nafamostat over Time

Source: Author.

In the case of VP35–Nafamostat, the dynamics were characterized by a high frequency of interactions, ranging from 2 to 5 bonds, with peaks of up to 8 bonds. The distribution was homogeneous throughout the simulation, indicating strong retention in the bonding region.

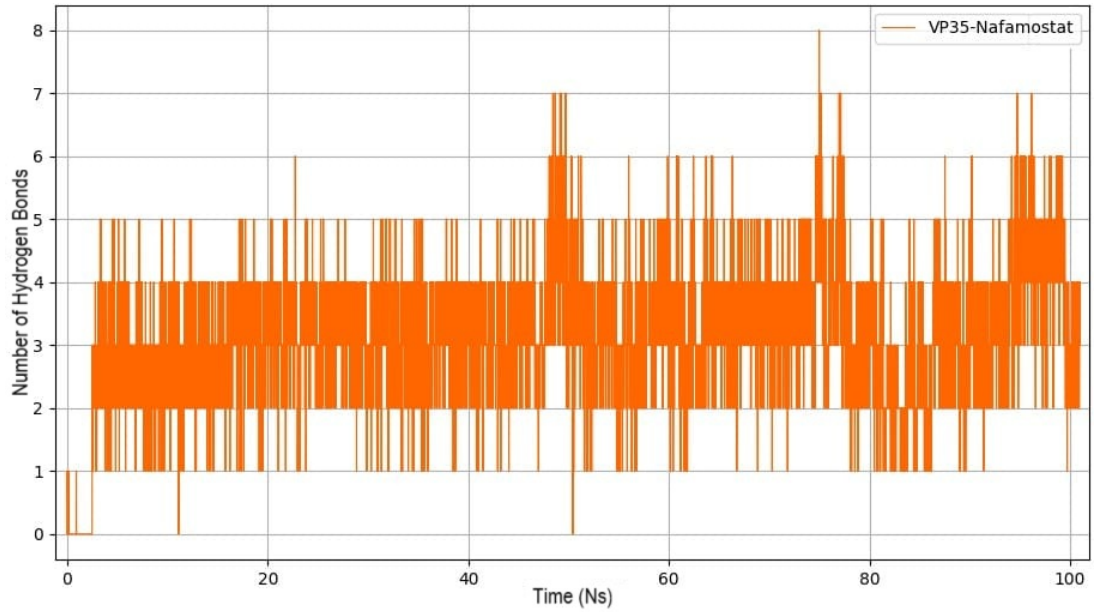

Figure 49 – Number of Hydrogen Bonds of VP35 with Nafamostat over Time

Source: Author.

Finally, VP40–Nafamostat (Figure 50) showed a gradual growth pattern in hydrogen

bonds until approximately 40 ns, at which point stability intensified. The complex reached up to 7 bonds, maintaining a range of 3 to 5 with high regularity.

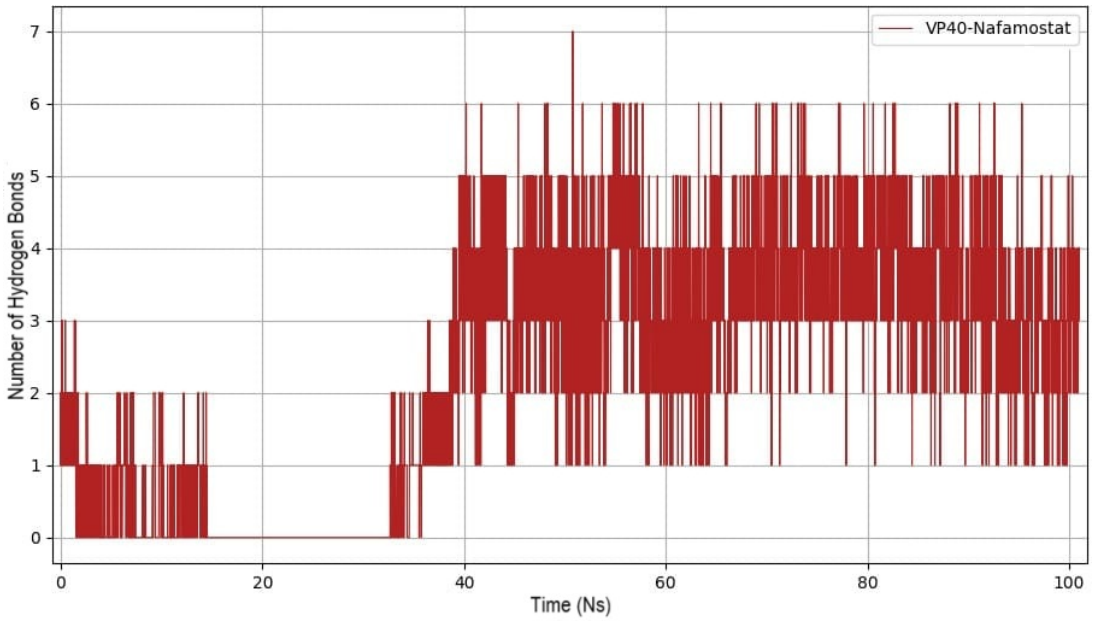

Figure 50 – Number of Hydrogen Bonds of VP40 with Nafamostat over Time

Source: Author.

These results demonstrate that Nafamostat is capable of establishing stable and intense hydrogen bond interactions with multiple Marburg virus proteins, being particularly effective with VP24, VP30, and VP35. The consistent binding profile throughout the simulation suggests a high antiviral potential and reinforces its value as a candidate for inhibiting viral replication.

Molecular dynamics simulations performed over 100 ns allowed us to evaluate the interactions between three drugs (Nafamostat, Ivermectin, and Lopinavir) and the main proteins of the Marburg virus. The results revealed that Ivermectin and Nafamostat presented more consistent interactions, as analyzed by the number and stability of hydrogen bonds over time, compared to those found in the DOC.

Nafamostat demonstrated the best performance among the compounds analyzed, forming stable interactions with all target proteins, with continuous binding profiles and high hydrophilic contact peaks—especially with VP24, VP30, and VP40. This behavior indicates strong affinity and potential antiviral efficacy, warranting further investigation.

Ivermectin, although exhibiting lower interaction intensity compared to nafamostat, displayed relevant binding patterns, primarily with VP40 and VP30, suggesting its ability to functionally interfere with viral targets.

On the other hand, Lopinavir presented a lower number and continuity of hydrogen bonds, indicating less stable interactions and a weaker overall affinity with viral proteins. Despite

this, some degree of interaction was observed in complexes such as GP2 and VP24, which may justify their combined use or as a basis for structural modifications in future derivatives.

In summary, the data point to nafamostat and ivermectin as promising candidates for combating Marburg virus, with lopinavir showing more limited results, but still relevant in specific contexts or as a comparative reference.

6 CONCLUSION

This research identified potential inhibitors of the main structures located on the surface and internally of Marburg through a combined computational procedure that repositioned inhibitory agents. Following our molecular docking assays, a series of ligand positions was generated, and the conformation that showed the highest docking score, associated with effective interactions, was selected as the most suitable for evaluation.

Analyzing the interactions and their attractive properties clearly demonstrates that these bonds within large molecular structures play a crucial role in forming stable interactions, exploiting the electronegativity difference between atoms. Within the active site, ligands interact with amino acid residues. Ivermectin exhibited acceptable affinity energy levels in molecular docking, with values of -9.01 kcal/mol for GP2, -8.74 kcal/mol for VP24, -10.22 kcal/mol for VP30, -8.74 kcal/mol for VP35, -10.54 kcal/mol for VP40, and -10.27 kcal/mol for NP.

Each assumed orientation can promote interactions with several amino acids in the specific region. As binding energies decrease, the strength of interactions between the ligand structures and the amino acid groups increases, and within the biological environment, the highest binding energy values are likely to be found in these tested positions.

Based on the data obtained through DOC, it was found that the four ligands tended to interact directly with the active sites of the macrostructures, suggesting that these regions have a greater chemical affinity for these molecules. Among the ligands evaluated, Ivermectin presented the most favorable results. Additionally, the DOC approach enabled the identification of the most suitable amino acids for establishing chemical bonds with the ligands.

The high charge density observed in the MEP analysis gave the receptor a greater propensity for reactivity to potential chemical interactions, which could result in the inhibition or neutralization of the virus-associated protein. Electrostatic interaction is considered a constant characteristic of ionic systems; applying both simulation approaches, larger molecules tend to exhibit greater polarizability. The charge distribution in interacting molecules directly influences the electrostatic potential, which is represented by the dipole moment of these molecules. The dipole moment tends to increase as the disparity in electronegativity between the bonded atoms increases. The number of hydrogen bonds observed showed that, in order of stability, Nafamostat and Ivermectin, followed by Lopinavir, demonstrated significant stability.

This study addressed a crucial question and the urgent need for new drugs to treat MARV infection. As demonstrated in this integrated study, computational analysis focused on the inhibition of the main external and internal configurations of MARV provided promising clues and evidence that indicate the need for further experimental confirmation. We hope that the information and computational predictions generated in this work, as well as the potential

clinical insights, will contribute to the advancement of identifying effective inhibitors of the main MARV structures.

Our computational approach to ligand repositioning identified potential drug candidates that, if validated through experimental and clinical studies, could represent a significant contribution to addressing the potential global crisis caused by MARV. Although simulation results can broaden understanding and aid in the interpretation of experimental data, this methodology has limitations and disadvantages. Observations from computational simulations were evaluated, demonstrating that the ligands possess interaction properties capable of attracting proteins. The results of these computational studies suggested that the binding capabilities of these inhibitors have the potential to be exploited in the development of therapeutic agents.

6.1 Contributions of this Dissertation

This dissertation contributes by proposing an approach that combines molecular docking, molecular dynamics, and electrostatic potential mapping to identify potential Marburg virus inhibitors. The work highlights ivermectin as a viral combatant, based on energy affinity values and detailed analysis of molecular interactions with the active site residues of the virus proteins. Regarding the number of hydrogen bonds, Nafamostat appears slightly more promising. Furthermore, the results highlight the importance of the electrostatic distribution of proteins in their interactions with ligands, providing valuable insights that can inform the development of antivirals. This study demonstrates the use of computational tools to support the search for treatments against emerging pathogens, such as MARV, and expands the frontiers of knowledge in the application of engineering in the context of biotechnology and healthcare.

6.2 Future Work – Application of Nanomaterials as MARV Virus Sensors

The methodology developed in this study can be applied to the analysis of nanomaterial sensors for Marburg virus detection. Carbon-based materials, including nanotubes, nanospheres, activated carbon, and graphene, exhibit physicochemical properties such as surface area, electrical conductivity, and sensitivity to molecular variations in the environment. These materials can recognize MARV particles. The interaction between the sensor and viral biomarkers can be converted into detectable optical, electrical, or electrochemical signals, enabling the development of portable, low-cost, and highly accurate devices for early diagnosis. Furthermore, the integration of nanomaterials, such as graphene and carbon nanotubes, with docking using artificial intelligence tools like GNINA can improve detection and analysis, making them a valuable tool in epidemiological monitoring and control of outbreaks of MARV and other highly lethal pathogens.

References

[1] C. Joseph Chan, "The human immunodeficiency virus: Biology, immunology, and therapy edited by emilio a. emini princeton, nj: Princeton university press, 2002. 532 pp., illustrated. $75.00 (cloth)," *Clinical Infectious Diseases*, vol. 35, no. 8, pp. 1025–1025, Oct. 2002.

[2] M. Gopikrishnan, S. Haryini, and G. P. D. C, "Emerging strategies and therapeutic innovations for combating drug resistance in staphylococcus aureus strains: A comprehensive review," *Journal of Basic Microbiology*, vol. 64, no. 5, p. 2300579, 2024.

[3] S. A. Hudu, A. O. Jimoh, K. A. Adeshina, E. G. Otalike, A. Tahir, and A. A. Hegazy, "An insight into the success, challenges, and future perspectives of eliminating neglected tropical disease," *Scientific African*, vol. 24, p. e02165, 2024.

[4] V. Patel and M. Shah, "Artificial intelligence and machine learning in drug discovery and development," *Intelligent Medicine*, vol. 2, no. 3, pp. 134–140, 2022.

[5] L. J. V. Piddock, Y. Alimi, J. Anderson, D. de Felice, C. E. Moore, J.-A. Røttingen, H. Skinner, and P. Beyer, "Advancing global antibiotic research, development and access," *Nature Medicine*, vol. 30, no. 9, pp. 2432–2443, 2024. [Online]. Available: https://doi.org/10.1038/s41591-024-03218-w

[6] O. I. González Peña, M. López Zavala, and H. Cabral Ruelas, "Pharmaceuticals market, consumption trends and disease incidence are not driving the pharmaceutical research on water and wastewater," *International Journal of Environmental Research and Public Health*, vol. 18, no. 5, p. 2532, 2021.

[7] I. Muegge, J. Bentzien, and Y. Ge, "Perspectives on current approaches to virtual screening in drug discovery," *Expert Opinion on Drug Discovery*, vol. 19, no. 10, pp. 1173–1183, Oct. 2024.

[8] V.-K. Tran-Nguyen, A.-C. Camproux, and O. Taboureau, "Classypose: A machine-learning classification model for ligand pose selection applied to virtual screening in drug discovery," *Advanced Intelligent Systems*, vol. 6, p. 2400238, 2024.

[9] S. Zhong, S. Liang, Y. Zhong, Y. Zheng, and F. Wang, "Measure on innovation efficiency of china's pharmaceutical manufacturing industry," *Frontiers in Public Health*, vol. 10, p. 1024997, 11 2022.

[10] S. Kumar, "Innovative drug discovery research by pharmaceutical companies in india and china," *Journal of Medicinal Chemistry*, vol. 67, no. 12, pp. 9773–9775, 2024.

[11] A. Gikas, "Evaluating factors enhancing profitability and sustainability of the pharmaceutical industry in greece," in *Financial Stability, Economic Growth and Sustainable Development*. Routledge, 2024, pp. 133–146.

[12] A. V. Sadybekov and V. Katritch, "Computational approaches streamlining drug discovery," *Nature*, vol. 616, no. 7958, pp. 673–685, 2023. [Online]. Available: https://doi.org/10.1038/s41586-023-05905-z

[13] SWISS INSTITUTE OF BIOINFORMATICS. (2025) Marburg virus. [Online]. Available: https://viralzone.expasy.org/224

[14] S. Srivastava, D. Sharma, S. Kumar, A. Sharma, R. Rijal, A. Asija, S. Adhikari, S. Rustagi, S. Sah, Z. H. Al-qaim, P. Bashyal, A. Mohanty, J. J. Barboza, A. J. Rodriguez-Morales, and R. Sah, "Emergence of marburg virus: a global perspective on fatal outbreaks and clinical challenges," *Frontiers in Microbiology*, vol. 14, p. 1239079, 2023.

[15] B. L. Ligon, "Outbreak of marburg hemorrhagic fever in angola: A review of the history of the disease and its biological aspects," *Seminars in Pediatric Infectious Diseases*, vol. 16, no. 3, pp. 219–224, 2005, adolescent and Sexually Transmitted Infections-An Update. [Online]. Available: https://www.sciencedirect.com/science/article/pii/S1045187005000464

[16] G. Sharma, A. R. Sharma, and J. C. Kim, "Recent advancements in the therapeutic development for marburg virus: updates on clinical trials," *Current Infectious Disease Reports*, vol. 26, pp. 57–67, 2024.

[17] M. R. Islam, S. Biswas, U. Amena, M. M. Rahman, M. M. Rahman, M. H. Rumi, T. M. Tallei, K. Dhama, and T. B. Emran, "Modified oxymatrine as novel therapeutic inhibitors against monkeypox and marburg virus through computational drug design approaches," *Journal of Cellular and Molecular Medicine*, vol. 28, no. e70116, 2024.

[18] T. I. Adelusi, A.-Q. K. Oyedele, I. D. Boyenle, A. T. Ogunlana, R. O. Adeyemi, C. D. Ukachi, M. O. Idris, O. T. Olaoba, I. O. Adedotun, O. E. Kolawole, Y. Xiaoxing, and M. Abdul-Hammed, "Molecular modeling in drug discovery," *Informatics in Medicine Unlocked*, vol. 29, p. 100880, 2022.

[19] T. Pantsar and A. Poso, "Binding affinity via docking: fact and fiction," *Molecules*, vol. 23, no. 8, p. 1899, 7 2018.

[20] D. C. Karnopp, D. L. Margolis, and R. C. Rosenberg, *System dynamics: modeling, simulation, and control of mechatronic systems*. John Wiley & Sons, 2012.

[21] R. Zhang, J. Lan, Q. Chen, Y. Liu, L. Hu, J. Cao, H. Zhao, and Y. Shen, "Hesperidin alleviates acute necrotizing pancreatitis by activating sirt1 – molecular docking, molecular

dynamics simulation, and experimental validation," *Combinatorial Chemistry & High Throughput Screening*, vol. 27, no. 12, pp. 1745–1757, 2024.

[22] I. M. Alsaady, L. H. Bajrai, T. A. Alandijany, H. S. Gattan, M. M. El-Daly, S. A. Altwaim, R. T. Alqawas, V. D. Dwivedi, and E. I. Azhar, "Cheminformatics strategies unlock marburg virus vp35 inhibitors from natural compound library," *Viruses*, vol. 15, no. 8, p. 1739, 2023.

[23] M. K. Lo, R. Jordan, A. Arvey, J. Sudhamsu, P. Shrivastava-Ranjan, A. L. Hotard, M. Flint, L. K. McMullan, D. Siegel, M. O. Clarke, R. L. Mackman, H. C. Hui, M. Perron, A. S. Ray, T. Cihlar, S. T. Nichol, and C. F. Spiropoulou, "Gs-5734 and its parent nucleoside analog inhibit filo-, pneumo-, and paramyxoviruses," *Scientific Reports*, vol. 7, no. 1, p. 43395, 2017. [Online]. Available: https://doi.org/10.1038/srep43395

[24] R. Das, A. Bhattarai, B. Tamang, and N. Thakur, "Identification of potential vp40 inhibitor of marburg virus through molecular docking, pharmacokinetic analysis and molecular dynamics simulation," *Scientific Reports*, vol. 15, no. 1, p. 27129, 2025. [Online]. Available: https://doi.org/10.1038/s41598-025-12917-4

[25] A. T. McNutt, P. Francoeur, R. Aggarwal, T. Masuda, H. M. Meli, J. R. Ragoza, S. H. Sunseri, and D. R. Koes, "GNINA 1.0: molecular docking with deep learning," *Journal of Cheminformatics*, vol. 13, no. 1, p. 43, 2021.

[26] H.-W. Ackermann and L. Berthiaume, *Atlas of Virus Diagrams*, 1st ed. CRC Press, 1995. [Online]. Available: https://doi.org/10.1201/9781003418238

[27] J. A. Galán-Torres, "Las fiebres hemorrágicas víricas," *Sanidad Militar*, vol. 79, no. 2, p. 72, 2023.

[28] M. P. Kiley, "Filoviridae: Marburg and ebola viruses," in *Laboratory Diagnosis of Infectious Diseases: Principles and Practice. Volume II: Viral, Rickettsial, and Chlamydial Diseases*. New York, NY: Springer, 1988, pp. 595–601.

[29] J. F. Koellhoffer, V. N. Malashkevich, J. S. Harrison, R. Toro, R. C. Bhosle, K. Chandran, S. C. Almo, and J. R. Lai, "Crystal structure of the marburg virus gp2 core domain in its postfusion conformation," *Biochemistry*, vol. 51, no. 39, pp. 7665–7675, 10 2012.

[30] S. Bale, J.-P. Julien, Z. A. Bornholdt, C. R. Kimberlin, P. Halfmann, M. A. Zandonatti, and et al., "Marburg virus vp35 can both fully coat the backbone and cap the ends of dsrna for interferon antagonism," *PLoS Pathogens*, vol. 8, no. 9, p. e1002916, 2012.

[31] A. Zhang, Z. Bornholdt, D. Abelson, and E. Saphire, "Crystal structure of marburg virus vp24," *Journal of Virology*, vol. 88, no. 10, pp. 5859–5863, 5 2014.

[32] S. Oda, T. Noda, K. J. Wijesinghe, P. Halfmann, Z. A. Bornholdt, D. M. Abelson, T. Armbrust, R. V. Stahelin, Y. Kawaoka, and E. O. Saphire, "Crystal structure of marburg virus vp40 reveals a broad, basic patch for matrix assembly and a requirement of the n-terminal domain for immunosuppression," *Journal of Virology*, vol. 90, no. 4, pp. 1839–1848, Dec. 2015.

[33] B. D. S. L. G. Liu, W. Wang, X. W. Y. Liu, C. R. Z. Yang, and Y. Guo, "Structural insight into nucleoprotein conformation change chaperoned by vp35 peptide in marburg virus," *Journal of Virology*, vol. 91, 2017.

[34] R. N. Kirchdoerfer, C. L. Moyer, D. M. Abelson, and E. O. Saphire, "The ebola virus vp30-np interaction is a regulator of viral rna synthesis," *PLOS Pathogens*, vol. 12, no. 10, pp. 1–22, 10 2016.

[35] RCSB Protein Data Bank. (2024) Rcsb pdb: The research collaboratory for structural bioinformatics protein data bank. [Online]. Available: https://www.rcsb.org/

[36] B. Kaur, C. Blavo, and M. S. Parmar, "Ivermectin: A multifaceted drug with a potential beyond anti-parasitic therapy," *Cureus*, 03 2024, open Access, Creative Commons Attribution License CC-BY 4.0.

[37] C. Aldous, E. Gkioulekas, and P. Oldfield, "Ivermectin," in *Controversies in the Pandemic*, J. Varon, P. E. Marik, M. Rendell, J. Iglesias, C. de Souza, and P. Prabhudesai, Eds. Jaypee Brothers Medical Publishers, 2024, pp. 434–471.

[38] A. Chandwani and J. Shuter, "Lopinavir/ritonavir no tratamento da infecção pelo hiv-1: uma revisão," *Terapêutica e Gestão de Riscos Clínicos*, vol. 4, no. 5, pp. 1023–1033, 2008.

[39] J. H. Shrimp, S. C. Kales, P. E. Sanderson, A. Simeonov, M. Shen, and M. D. Hall, "An enzymatic tmprss2 assay for assessment of clinical candidates and discovery of inhibitors as potential treatment of covid-19," *ACS Pharmacology & Translational Science*, vol. 3, no. 5, pp. 997–1007, Sep. 2020.

[40] G. Z. Ghali and M. G. Z. Ghali, "O mesilato de nafamostat atenua as sequelas fisiopatológicas da isquemia neurovascular," *Pesquisa de Regeneração Neural*, vol. 15, no. 12, pp. 2217–2234, 12 2020.

[41] M. Hoffmann, H. Hofmann-Winkler, J. C. Smith, N. Krüger, P. Arora, L. K. Sørensen, O. S. Søgaard, J. B. Hasselstrøm, M. Winkler, T. Hempel, L. Raich, S. Olsson, O. Danov, D. Jonigk, T. Yamazoe, K. Yamatsuta, H. Mizuno, S. Ludwig, F. Noé, M. Kjolby, A. Braun, J. M. Sheltzer, and S. Pöhlmann, "Camostat mesylate inhibits sars-cov-2 activation by tmprss2-related proteases and its metabolite gbpa exerts antiviral activity," *eBioMedicine*, vol. 65, Mar. 2021.

[42] M. G. Santoro and E. Carafoli, "Remdesivir: From ebola to covid-19," *Biochemical and Biophysical Research Communications*, vol. 538, pp. 145–150, 2021.

[43] E. P. Tchesnokov, J. Y. Feng, D. P. Porter, and M. Götte, "Mechanism of inhibition of ebola virus rna-dependent rna polymerase by remdesivir," *Viruses*, vol. 11, no. 4, p. 326, 2019.

[44] F. Grundeis, K. Ansems, K. Dahms, V. Thieme, M. I. Metzendorf, N. Skoetz, C. Benstoem, A. Mikolajewska, M. Griesel, F. Fichtner, and M. Stegemann, "Remdesivir for the treatment of covid-19," *Cochrane Database of Systematic Reviews*, vol. 1, no. 1, p. CD014962, 2023.

[45] D. P. Porter, J. M. Weidner, L. Gomba, R. Bannister, C. Blair, R. Jordan, J. Wells, K. Wetzel, N. Garza, S. Van Tongeren, G. Donnelly, J. Steffens, A. Moreau, J. Bearss, E. Lee, S. Bavari, T. Cihlar, and T. K. Warren, "Remdesivir (gs-5734) is efficacious in cynomolgus macaques infected with marburg virus," *The Journal of Infectious Diseases*, vol. 222, no. 11, pp. 1894–1901, 2020.

[46] R. W. Cross, C. Woolsey, A. N. Prasad *et al.*, "Oral obeldesivir provides postexposure protection against marburg virus in nonhuman primates," *Nature Medicine*, vol. 31, pp. 1303–1311, 2025.

[47] N. C. for Biotechnology Information, "Pubchem," 2025, accessed on: Sept. 19, 2024. [Online]. Available: https://pubchem.ncbi.nlm.nih.gov/

[48] MolView, "Molview," 2025, accessed on: Sept. 19, 2024. [Online]. Available: https://app.molview.com/

[49] D. S. Sholl and J. A. Steckel, *Density Functional Theory: A Practical Introduction*. Hoboken: Wiley, 2009.

[50] Y. Shi and A. Wasserman, "Inverse kohn–sham density functional theory: Progress and challenges," *The Journal of Physical Chemistry Letters*, vol. 12, no. 22, pp. 5308–5318, 2021. [Online]. Available: https://doi.org/10.1021/acs.jpclett.1c00752

[51] D. Sharma and S. N. Tiwari, "Electronic structure and vibrational spectra of 1ocb liquid crystal: a dft study," *Emerging Materials Research*, vol. 6, no. 2, pp. 322–330, July 2017. [Online]. Available: https://doi.org/10.1680/jemmr.15.00052

[52] I. N. Levine, D. H. Busch, and H. Shull, *Quantum Chemistry*. Upper Saddle River, NJ: Pearson Prentice Hall, 2009.

[53] R. Agarwal, A. Singh, and S. Sen, "Role of molecular docking in computer-aided drug design and development," in *Pharmaceutical Sciences: Breakthroughs in Research and Practice*. IGI Global, 2017, p. 28.

[54] P. J. Goodford, "Drug design by the method of receptor fit," *Journal of Medicinal Chemistry*, vol. 27, no. 5, pp. 557–564, 1984.

[55] D. Vlachakis, Ed., *Molecular Docking*. BoD – Books on Demand, 2018.

[56] A. Tripathi and V. A. Bankaitis, "Molecular docking: From lock and key to combination lock," *Journal of Molecular Medicine and Clinical Applications*, vol. 2, no. 1, p. 106, 2017.

[57] E. S. İstifli, Ed., *Molecular Docking*. London: IntechOpen, 2023, creative Commons License.

[58] D. E. Clark, *Algoritmos Evolutivos em Design Molecular*. EUA: John Wiley & Sons, Inc., 1999.

[59] L. N. Trefethen, "Pseudospectra of linear operators," *SIAM Review*, vol. 39, no. 3, pp. 383–406, 1997.

[60] S. Saikia and M. Bordoloi, "Molecular docking: Challenges, advances and its use in drug discovery perspective," *Current Drug Targets*, vol. 20, no. 5, pp. 501–521, 2019.

[61] M. S. Musa and S. T. Chowdhury, "Molecular docking: Aiming for a perfect fit," in *Molecular Modeling and Docking Techniques for Drug Discovery and Design*. Chittagong, Bangladesh: IGI Global, 2025, p. 24. [Online]. Available: https://doi.org/10.4018/979-8-3693-5598-5.ch012

[62] M. Kumar, S. K. Tamang, M. Dabi *et al.*, "Effect of surface charge on wettability and electrolyte behavior on graphene surfaces using molecular dynamic simulation," *Scientific Reports*, vol. 15, p. 17415, 2025. [Online]. Available: https://doi.org/10.1038/s41598-025-02331-1

[63] T. Eakin, J. Ferdaous, S. Hossain, J. Ferdous, and S. M. A. Kawsar, "Enhancing the efficiency of medicinal chemistry through computational chemistry," in *Molecular Modeling and Docking Techniques for Drug Discovery and Design*. Chittagong, Bangladesh: IGI Global, 2025, p. 34.

[64] S. Lakshminarayanan, V. Jeyasingh, K. Murugesan, N. Selvapalam, and G. Dass, "Molecular electrostatic potential (mep) surface analysis of chemo sensors: An extra supporting hand for strength, selectivity & non-traditional interactions," *Journal of Photochemistry and Photobiology*, vol. 6, p. 100022, 2021.

[65] O. Noureddine, N. Issaoui, and O. Al-Dossary, "Dft and molecular docking study of chloroquine derivatives as antiviral to coronavirus covid-19," *Journal of King Saud University - Science*, vol. 33, no. 1, p. 101248, 2021.

[66] M. Guin, S. Halder, S. Chatterjee, and S. Konar, "Synthesis, x-ray crystal structure of cu(ii) 1d coordination polymer: In view of hirshfeld surface, fmo, molecular electrostatic potential (mep) and natural bond orbital (nbo) analyses," *Journal of Molecular Structure*, vol. 1270, p. 133949, 2022.

[67] S. Ghahremanian, M. M. Rashidi, K. Raeisi, and D. Toghraie, "Molecular dynamics simulation approach for discovering potential inhibitors against sars-cov-2: A structural review," *Journal of Molecular Liquids*, vol. 354, p. 118901, 2022.

[68] P. Qu, D. Li, R. Lazim, R. Xu, D. Xiao, F. Wang, X. Li, and Y. Zhang, "Improved thermostability of thermomyces lanuginosus lipase by molecular dynamics simulation and in silico mutation prediction and its application in biodiesel production," *Fuel*, vol. 327, p. 125039, 2022.

[69] M. S. Badar, S. Shamsi, J. Ahmed, and M. A. Alam, "Molecular dynamics simulations: Concept, methods, and applications," in *Transdisciplinarity*, ser. Integrated Science, N. Rezaei, Ed. Springer, Cham, 2022, vol. 5.

[70] H. Kamberaj, "Advances and challenges in computer simulations of biological and molecular systems," in *Book of Abstracts Third International Conference of the National Institute of Physics*, 2025, p. 26.

[71] J. Wahlers, A. R. Rosales, N. Berkel, A. Forbes, P. Helquist, P.-O. Norrby, and O. Wiest, "A quantum-guided molecular mechanics force field for the ferrocene scaffold," *The Journal of Organic Chemistry*, vol. 87, no. 18, pp. 12 334–12 341, 2022.

[72] W. Kang, F. Jiang, and Y.-D. Wu, "How to strike a conformational balance in protein force fields for molecular dynamics simulations?" *WIREs Computational Molecular Science*, vol. 12, p. e1578, 2022.

[73] X. Wang, J. Li, L. Yang, F. Chen, Y. Wang, J. Chang, J. Chen, W. Feng, L. Zhang, and K. Yu, "Dmff: An open-source automatic differentiable platform for molecular force field development and molecular dynamics simulation," *Journal of Chemical Theory and Computation*, vol. 19, no. 17, pp. 5897–5909, 2023.

[74] H. Lin, Y. Shi, E. Shang, and S. Dai, "An energy minimization strategy based on an improved nonlinear conjugate gradient method for accelerating the charged polymer dynamics simulation," *Phys. Chem. Chem. Phys.*, vol. 25, pp. 12 290–12 307, 2023.

[75] S. Sasidharan, V. Gosu, T. Tripathi, and P. Saudagar, "Molecular dynamics simulation to study protein conformation and ligand interaction," in *Protein Folding Dynamics and Stability*, P. Saudagar and T. Tripathi, Eds. Singapore: Springer, 2023.

[76] T. Fukutani, K. Miyazawa, S. Iwata, and H. Satoh, "G-rmsd: Root mean square deviation based method for three-dimensional molecular similarity determination," *Bulletin of the Chemical Society of Japan*, vol. 94, no. 2, pp. 655–665, 2021.

[77] A. Robitzsch, "Statistical properties of estimators of the rmsd item fit statistic," *Foundations*, vol. 2, no. 2, pp. 488–503, 2022.

[78] L. Fu, *Neural Networks in Computer Intelligence*. USA: McGraw-Hill, Inc., 1994.

[79] T. Khanna, *Foundations of neural networks*. USA: Addison-Wesley Longman Publishing Co., Inc., 1990.

[80] A. T. McNutt, Y. Li, R. Meli, and et al., "Gnina 1.3: the next increment in molecular docking with deep learning," *Journal of Cheminformatics*, vol. 17, p. 28, 2025.

[81] R. Venkatesan and B. Li, *Convolutional Neural Networks in Visual Computing: A Concise Guide*, 1st ed. CRC Press, 2017.

[82] J. Sunseri and D. R. Koes, "Virtual screening with gnina 1.0," *Molecules*, vol. 26, no. 23, p. 7369, 2021.

[83] G. Tsaparlis, G. Pantazi, E. T. Pappa, and B. Byers, "Using electrostatic potential maps as visual representations to promote better understanding of chemical bonding," *Chemistry Teacher International*, vol. 3, no. 4, pp. 391–411, 2021.

[84] C. H. Suresh, G. S. Remya, and P. K. Anjalikrishna, "Molecular electrostatic potential analysis: A powerful tool to interpret and predict chemical reactivity," *WIREs Computational Molecular Science*, vol. 12, p. e1601, 2022.

[85] E. Scrocco and J. Tomasi, "The electrostatic molecular potential as a tool for the interpretation of molecular properties," in *New Concepts II*, ser. Topics in Current Chemistry Fortschritte der Chemischen Forschung. Springer, Berlin, Heidelberg, 1973, vol. 42, pp. 95–170.

[86] M. J. Frisch, G. W. Trucks, H. B. Schlegel, G. E. Scuseria, M. A. Robb, J. R. Cheeseman, G. Scalmani, V. Barone, G. A. Petersson, H. Nakatsuji, X. Li, M. Caricato, A. V. Marenich, J. Bloino, B. G. Janesko, R. Gomperts, B. Mennucci, H. P. Hratchian, J. V. Ortiz, A. F. Izmaylov, J. L. Sonnenberg, D. Williams-Young, F. Ding, F. Lipparini, F. Egidi, J. Goings, B. Peng, A. Petrone, T. Henderson, D. Ranasinghe, V. G. Zakrzewski, J. Gao, N. Rega, G. Zheng, W. Liang, M. Hada, M. Ehara, K. Toyota, R. Fukuda, J. Hasegawa, M. Ishida, T. Nakajima, Y. Honda, O. Kitao, H. Nakai, T. Vreven, K. Throssell, J. A. J. Montgomery, J. E. Peralta, F. Ogliaro, M. J. Bearpark, J. J. Heyd, E. Brothers, K. N. Kudin, V. N. Staroverov, T. A. Keith, R. Kobayashi, J. Normand, K. Raghavachari, A. P. Rendell, J. C. Burant, S. S. Iyengar, J. Tomasi, M. Cossi, J. M. Millam, M. Klene, C. Adamo, R. Cammi,

J. W. Ochterski, R. L. Martin, K. Morokuma, O. Farkas, J. B. Foresman, and D. J. Fox, *Gaussian 16, Revision B.01*, Gaussian, Inc., Wallingford CT, 2016, revision B.01.

[87] A. Fatima, H. Arora, P. Bhattacharya, N. Siddiqui, K. M. Abualnaja, P. Garg, and S. Javed, "Dft, molecular docking, molecular dynamics simulation, mmgbsa calculation and hirshfeld surface analysis of 5-sulfosalicylic acid," *Journal of Molecular Structure*, vol. 1273, p. 134242, 2023.

[88] C. F. Matta, "Modeling biophysical and biological properties from the characteristics of the molecular electron density, electron localization and delocalization matrices, and the electrostatic potential," *Journal of Computational Chemistry*, vol. 35, no. 16, pp. 1165–1198, 2014.

[89] O. Trott and A. J. Olson, "Autodock vina: Improving the speed and accuracy of docking with a new scoring function, efficient optimization, and multithreading," *Journal of Computational Chemistry*, vol. 31, no. 2, pp. 455–461, 2010.

[90] R. Wang, X. Fang, Y. Lu, and S. Wang, "The pdbbind database: collection of binding affinities for protein–ligand complexes with known three-dimensional structures," *Journal of Medicinal Chemistry*, vol. 47, no. 12, pp. 2977–2980, 2004. [Online]. Available: https://doi.org/10.1021/jm030580l

[91] "Gnina 4.2 cnn scoring guide," https://deepwiki.com/gnina/gnina/4.2-cnn-scoring-guide, 2025, accessed: October 10, 2024.

[92] M. H. R. Molla, M. O. Aljahdali, M. A. A. Sumon, A. H. Asseri, H. N. Altayb, M. S. Islam, A. A. Alsaiari, F. A. D. M. Opo, N. Jahan, F. Ahammad, and F. Mohammad, "Integrative ligand-based pharmacophore modeling, virtual screening, and molecular docking simulation approaches identified potential lead compounds against pancreatic cancer by targeting fak1," *Pharmaceuticals*, vol. 16, no. 1, p. 120, 2023.

[93] S. Jo, T. Kim, V. G. Iyer, and W. Im, "CHARMM-GUI: a web-based graphical user interface for CHARMM," *Journal of Computational Chemistry*, vol. 29, no. 11, pp. 1859–1865, 2008.

[94] H. Guterres, S.-J. Park, H. Zhang, T. Perone, J. Kim, and W. Im, "CHARMM-GUI high-throughput simulator for efficient evaluation of protein–ligand interactions with different force fields," *Protein Science*, vol. 31, no. 9, p. e4413, 2022.

[95] D. J. Huggins, "Comparing the performance of different amber protein forcefields, partial charge assignments, and water models for absolute binding free energy calculations," *Journal of Chemical Theory and Computation*, vol. 18, no. 4, pp. 2616–2630, 2022. [Online]. Available: https://doi.org/10.1021/acs.jctc.1c01208

[96] M. A. Chiacchio, L. Legnani, E. M. A. Fassi, G. Roda, and G. Grazioso, "Development of AMBER Parameters for Molecular Simulations of Selected Boron-Based Covalent Ligands," *Molecules*, vol. 28, no. 6, p. 2866, 2023.

[97] National Center for Biotechnology Information, "PubChem Compound Database," https://pubchem.ncbi.nlm.nih.gov/, 2024, accessed: 2024. [Online]. Available: https://pubchem.ncbi.nlm.nih.gov/

[98] L. J. Bartolotti and K. Flurchick, "Uma introdução à teoria do funcional da densidade," in *Revisões em Química Computacional*, K. B. Lipkowitz and D. B. Boyd, Eds. Wiley, 1996, ch. 4, [S.l.].

[99] L. Emami, M. Hassani, P. Mardaneh, and et al., "6-bromo quinazoline derivatives as cytotoxic agents: design, synthesis, molecular docking and md simulation," *BMC Chemistry*, vol. 18, p. 125, 2024.

[100] J. Eberhardt, D. Santos-Martins, A. F. Tillack, and S. Forli, "Autodock vina 1.2.0: New docking methods, expanded force field, and python bindings," *Journal of Chemical Information and Modeling*, vol. 61, no. 8, pp. 3891–3898, 2021.

[101] I. A. Guedes, C. S. de Magalhães, and L. E. Dardenne, "Receptor-ligand molecular docking," *Biophysical Reviews*, vol. 6, no. 1, pp. 75–87, 2014.

[102] S. Yakoubi, "Enhancing plant-based cheese formulation through molecular docking and dynamic simulation of tocopherol and retinol complexes with zein, soy and almond proteins via svm-machine learning integration," *Food Chemistry*, vol. 452, p. 139520, 2024.

[103] A. Díaz-Holguín, M. Saarinen, D. D. Vo, A. Sturchio, N. Branzell, I. Cabeza de Vaca, H. Hu, N. Mitjavila-Domènech, A. Lindqvist, P. Baranczewski, M. J. Millan, Y. Yang, J. Carlsson, and P. Svenningsson, "Alphafold accelerated discovery of psychotropic agonists targeting the trace amine-associated receptor 1," *Science Advances*, vol. 10, no. 32, p. eadn1524, 2024.

[104] E. Tuntufye, L. Paul, J. Raymond, M. Chacha, A. S. Paluch, and D. M. Shadrack, "In silico analysis of vitamin d interactions with aging proteins: docking, molecular dynamics, and solvation free energy studies," *ChemEngineering*, vol. 8, no. 5, p. 104, 2024.

[105] S. Abdullah, A. Iqbal, A. K. Ashok, F. C. Kaouche, M. Aslam, S. Hussain, J. Rahman, M. M. Hayat, and M. Ashraf, "Anti-enzymatic and dna docking studies of montelukast: A multifaceted molecular scaffold with in vitro investigations, molecular expression analysis and molecular dynamics simulations," *Heliyon*, vol. 10, no. 2, p. e24470, 2024.

[106] P. Kumar and A. Kumar, "State-of-the-art modeling techniques in performing docking algorithms and scoring," in *Computational Drug Discovery: Molecular Simulation for Medicinal Chemistry*, P. A. Chawla, D. Singh, K. Dua, M. Dhanasekaran, and V. Chawla, Eds. Berlin, Boston: De Gruyter, 2024, ch. 4, pp. 65–80.

[107] Accelrys Software Inc., *Discovery Studio Modeling Environment, Release 3.5*, Accelrys Software Inc., San Diego, CA, 2012, proprietary molecular modeling software.

[108] E. W. Bell and Y. Zhang, "Dockrmsd: an open-source tool for atom mapping and rmsd calculation of symmetric molecules through graph isomorphism," *Journal of Cheminformatics*, vol. 11, p. 40, 2019.

[109] K. A. Peele, C. P. Durthi, T. Srihansa, S. Krupanidhi, V. S. Ayyagari, D. J. Babu, M. Indira, A. Ranganadha Reddy, and T. C. Venkateswarulu, "Molecular docking and dynamic simulations for antiviral compounds against sars-cov-2: a computational study," *Informatics in Medicine Unlocked*, vol. 19, p. 100345, 2020.

[110] J. Wang, R. M. Wolf, J. W. Caldwell, P. A. Kollman, and D. A. Case, "Development and testing of a general amber force field," *Journal of Computational Chemistry*, vol. 25, no. 9, pp. 1157–1174, 2004.

[111] K. Vanommeslaeghe, E. Hatcher, C. Acharya, S. Kundu, S. Zhong, J. Shim, E. Darian, O. Guvench, P. Lopes, I. Vorobyov, and A. D. J. Mackerell, "Charmm general force field: A force field for drug-like molecules compatible with the charmm all-atom additive biological force fields," *Journal of Computational Chemistry*, vol. 31, no. 4, pp. 671–690, 2010.

[112] C. Oostenbrink, A. Villa, A. E. Mark, and W. F. Van Gunsteren, "A biomolecular force field based on the free enthalpy of hydration and solvation: The gromos force-field parameter sets 53a5 and 53a6," *Journal of Computational Chemistry*, vol. 25, no. 13, pp. 1656–1676, 2004.

[113] A. R. Almeida, D. X. Andrade, and G. Colherinhas, "Statistical and energetic analysis of hydrogen bonds in short and long peptide nanotapes/nanofibers using molecular dynamics simulations," *Journal of Molecular Liquids*, vol. 359, p. 119308, 2022.

[114] S. Miyamoto and P. A. Kollman, "Settle: An analytical version of the shake and rattle algorithm for rigid water models," *Journal of Computational Chemistry*, vol. 13, no. 9, pp. 952–962, 1992.

[115] U. Essmann, L. Perera, M. L. Berkowitz, T. Darden, H. Lee, and L. G. Pedersen, "A smooth particle mesh ewald method," *The Journal of Chemical Physics*, vol. 103, no. 19, pp. 8577–8593, 1995.

[116] D. R. Roe and T. E. I. Cheatham, "Ptraj and cpptraj: software for processing and analysis of molecular dynamics trajectory data," *Journal of Chemical Theory and Computation*, vol. 9, no. 7, pp. 3084–3095, 2013.

[117] S. S. Tariq, K. Zia, M. Nur-e Alam, D. Nerukh, V. S. Farafonov, and Z. Ul-Haq, "Impact of mutations in sars-cov-2 recombinant sub-variant xbb.1.16 on the binding affinity with human ace2 receptor," *Journal of Molecular Graphics and Modelling*, vol. 131, p. 108813, 2024.

[118] D. M. Aziz, "Molecular docking analysis," in *Molecular Modeling and Docking Techniques for Drug Discovery and Design*. IGI Global Scientific Publishing, 2025, pp. 401–434.

APPENDIX A – Article I

This article corresponds to the first part of the research presented in this Master's Dissertation proposal and was published in the journal *Cuadernos de Educación y Desarrollo*, which holds a Qualis Capes rating of A4 in the Interdisciplinary area.

CUADERNOS DE EDUCACIÓN Y DESARROLLO

SOBRE A REVISTA ▾ POLÍTICAS EDITORIAIS ▾ ATUAL ARQUIVOS ▾ ANÚNCIOS FONTES DE INDEXAÇÃO ▾ CONTATO SUBMISSÕES TEMPLATE

v. 17 n. 7 (2025)

Usando Dinâmica Molecular e Rede Neural na Análise de Fármacos no Combate ao Vírus Marburg

ARTICLES

https://doi.org/10.55905/cuadv17n7-051

Publicado 16-07-2025

Aguinaldo Pantoja de Almeida, Ricardo José Klöppel, Kleber Ferreira de Vilhena, Cássio da Cruz Nogueira, Claudomiro de Souza de Sales Junior

Resumo

Este artigo tem como objetivo analisar os fármacos Ivermectina, Nafamostat e Lopinavir como possíveis combatentes do vírus Marburg, que apresenta uma alta taxa de mortalidade, por meio de técnicas computacionais. Os resultados das docagens moleculares tiveram resultados de energia de afinidade variando de -9.01 até -10.54 kcal/mol para Ivermectina, -7.37 a -10.46 kcal/mol para Lopinavir e para Nafamostat variou de -7.16 até 10.00 kcal/mol. Os resultados da simulação de dinâmica molecular com o software GROMACS 2024.2, mostraram que os ligantes mantiveram interações com as proteínas Glicoproteína Transmembrana, VP24, VP30, VP35 e VP40. O mapa de potencial eletrostático mostrou as regiões de maior facilidade de interação. O estudo do desvio quadrático médio (RMSD) revelou resultados entre 0,25 e 2,0 Å para a Ivermectina e resultados entre 0,25 e 2,6 Å para Nafamostat, constatando alta estabilidade dos complexos estudados. Os resultados evidênciam que os fármacos podem ser possíveis candidatos no combate do MARV, demostram uma abordagem terapêutica possível que, se for validada com pesquisas experimentais, poderá reduzir a mortalidade associada ao vírus.

PDF

Palavras-chave

MARV
docagem molecular
fármacos
dinâmica molecular

Referências

ACCELRYS SOFTWARE INC. AS Discovery Studio Modeling Environment, release 3.5. San Diego (CA): Accelrys Software Inc, 2012.

ALMEIDA, A. R.; ANDRADE, D. X.; COLHERINHAS, G. Statistical and energetic analysis of hydrogen bonds in short and long peptide

APPENDIX B – Article II

This article corresponds to the second part of the research presented in this Master's Dissertation proposal and was published in the journal *Cuadernos de Educación y Desarrollo*, which holds a Qualis Capes rating of A4 in the Interdisciplinary area.

CUADERNOS DE EDUCACIÓN Y DESARROLLO

SOBRE A REVISTA ▾ POLÍTICAS EDITORIAIS ▾ ATUAL ARQUIVOS ▾ ANÚNCIOS FONTES DE INDEXAÇÃO ▾ CONTATO SUBMISSÕES TEMPLATE

v. 17 n. 8 (2025)

Análise de fármacos através ligações de hidrogênio no combate ao vírus Marburg

ARTICLES

https://doi.org/10.55905/cuadv17n8-022

Publicado 06-08-2025

Aguinaldo Pantoja de Almeida, Cássio da Cruz Nogueira, Ricardo José Klöppel, Kleber Ferreira de Vilhena, Jonas Diniz Furtado, Claudomiro de Souza de Sales Junior

Resumo

Ferramentas computacionais como molecular docking e simulações de dinâmica molecular (MD) têm se mostrado essenciais na busca por antivirais contra o vírus de Marburg (MARV). Este estudo analisou as interações entre três compostos antivirais — Nafamostat, Ivermectina e Lopinavir — e proteínas-chave do vírus: VP24, VP30, VP35, VP40 e GP2. Resultados prévios demonstraram boas energias de afinidade, mapas de potencial e RMSD. Agora, a análise de ligações de hidrogênio durante as simulações reforça tais achados. O Nafamostat apresentou interações com todas as proteínas-alvo, especialmente com VP24 e VP30, chegando a até oito ligações de hidrogênio. A Ivermectina destacou-se nas interações com VP40 e VP30, mantendo boa estabilidade. Já o Lopinavir, embora com afinidade inferior, mostrou interações significativas com GP2 e VP24 em momentos específicos. Os dados sugerem que abordagens computacionais são vantajosas na triagem de fármacos, permitindo identificar compostos promissores com bom perfil de ligação antes dos testes laboratoriais. Entre os analisados, o Nafamostat demonstrou o desempenho mais consistente, seguido pela Ivermectina. Embora o Lopinavir tenha mostrado menos eficácia geral, suas interações pontuais indicam potenciais a ser explorado. Tais resultados reforçam a importância das simulações no avanço de terapias antivirais.

PDF

Referências

Palavras-chave

MARV
docagem molecular
fármacos
dinâmica molecular